Università degli studi di Udine

Corso di dottorato di ricerca in:
Informatica e Scienze Matematiche e Fisiche
Ciclo XXXIII

TITOLO DELLA TESI

Monte Carlo simulation and data analysis of sky observation mode with the Cherenkov Telescope Array

Dottoranda:
Alice Donini

Supervisore:
Prof. ssa Barbara De Lotto

Co-supervisore:
Prof. Francesco Longo

Anno 2019-2020

Declaration of Authorship

I, Alice Donini, declare that this thesis titled, "Monte Carlo simulation and data analysis of sky observation mode with the Cherenkov Telescope Array" and the work presented in it are my own. I confirm that:

- This work was done wholly or mainly while in candidature for a research degree at this University.

- Where any part of this thesis has previously been submitted for a degree or any other qualification at this University or any other institution, this has been clearly stated.

- Where I have consulted the published work of others, this is always clearly attributed.

- Where I have quoted from the work of others, the source is always given. With the exception of such quotations, this thesis is entirely my own work.

- I have acknowledged all main sources of help.

- Where the thesis is based on work done by myself jointly with others, I have made clear exactly what was done by others and what I have contributed myself.

Signed:

_____

Date:

_____

"I am not young enough to know everything."

Oscar Wilde

Contents

List of Figures

List of Tables

Abstract

The success of the current generation of Imaging Atmospheric Cherenkov Telescopes (IACTs) has affirmed the importance of gamma-ray astronomy for modern astrophysics. This field focuses on the upper end of the electromagnetic spectrum, with energies in the range of $\sim 50\,\mathrm{GeV}$ to hundreds of TeV. Gamma rays, due to their neutral charge, are not disturbed by deflection from magnetic fields in their journey across the Universe, and can be traced back through their incoming direction. Thus, they can address to identify the acceleration processes of high-energy particles close to their acceleration sites, and also answer to some of the most fundamental physics issues, like the Lorentz invariance or the mystery of Dark Matter. Currently in the construction stage, the Cherenkov Telescope Array (CTA) is the next generation ground-based observatory for gamma-ray astronomy at very-high energies and it will exceed its predecessors in every aspect, e.g. energy range, sensitivity, field of view or angular resolution.

The galactic and extragalactic surveys are two of the main proposed legacy projects of CTA, providing an unbiased view of the Universe at energies above tens of GeV. Surveys provide an immense service to the researchers community in the context of an open observatory, since they constitute versatile datasets that enable the detection of unexpected sources and provide testing ground for new theoretical ideas. Considering Cherenkov telescopes' limited field of view (FoV), the time needed for those science projects is large. The limited duty cycle of about 1000 hours per year of imaging Cherenkov facilities is a strong motivation to try to reduce the observation time needed for the surveys. The huge number of telescopes of CTA with respect to existing instruments, will allow taking full advantage of new pointing modes in which telescopes point slightly offset from one another, like the divergent mode.

This pointing mode leads to an increase in the field of view of the sub-array of telescopes with competitive performance compared to normal pointing of the same sub-array. This type of observation should also improve CTA capacity to detect transient events, such as Gamma-Ray Bursts (GRBs), thanks to the Large Size Telescope (LST) fast repointing capability and low energy threshold, and the ability to cover more complex patterns of the sky, like mapping a Gravitational Wave (GW) probability sky map or GRB large error boxes. A divergent pointing mode was included in the CTA science requirements document but, apart from a few publications, up to now it has never been the center of an in-depth study. This thesis is devoted to the improvement of the analysis in divergent mode and to study the performance of this modality for different array configurations and number of telescopes, in order to investigate if the performance are competitive compared to normal pointing. To completion of the work and my interest in transient events, I will also present the data analysis of several GRBs I performed within the transient group for the Major Atmospheric Gamma-ray Imaging Cherenkov (MAGIC)

collaboration. The thesis is arranged as follows:

- **Chapter 1**: An introduction to the high-energy astrophysics field. The different gamma ray production mechanisms, together with known and potential sources expected to emit in this energy range, are described.

- **Chapter 2**: A summary of the detection techniques employed to measure highly energetic photons. The IACT technique and the showers development are described.

- **Chapter 3**: A description of the CTA project with a focus on the different telescopes and its scientific goals related to this work are given.

- **Chapter 4**: This chapter describes the processes needed to derive the array performance. The programs for the Monte Carlo simulations and also the pipelines used to process the raw data till the performance are explained.

- **Chapter 5**: The chapter is devoted to the work done inside the MAGIC Collaboration. A brief introduction of the telescopes and how they operate is given. A summary of the GRB phenomenon and the results of the analysis performed on 4 of this events are presented.

- **Chapter 6**: In this last chapter the results obtained for sensitivity studies in divergent mode are illustrated. The changes brought to the pipeline needed to perform a divergent analysis are also described, together with the tool developed for the definition of the pointings.

High-Energy Astrophysics

Nowadays astronomy covers all the electromagnetic spectrum allowing to study sources at different wavelengths, from radio waves up to the gamma-ray range, which represents the final window to explore.

Gamma-ray astronomy is relatively new; it was born in the last decades of the XX century when, after the Second World War, the deployment of the first gamma-ray detectors where put into orbit. The extremely energetic processes these detectors observed in the universe could not be explained with conventional thermal emission. The field of high energy astronomy deals with the study of such non-thermal processes.

High-energy astrophysics is strictly connected to the particle physics and it is often referred as *astroparticle physics*. It offers an exceptional area of research for fundamental physics and opens questions like the origin of cosmic rays, the properties of neutrinos, the nature of Dark Matter as well as the nature of gravity, which may find an answer thanks to the synergy between these two fields. Its rapid development has led to the design of new types of experiments, which employ new detection techniques to observe a wide range of cosmic particles including neutrinos, γ-rays and charged particles up to the highest energies.

This Chapter is an introduction to gamma-ray astrophysics, describing the mechanisms and sources of production of γ-rays in the Universe. A brief summary of other non-electromagnetic messengers will be given too.

1.1 Cosmic rays

In the beginning of the XXth century several experiments were carried out to measure the variation of ionization under water and in altitude [1]. Cosmic rays (CR) were finally established as of extraterrestrial origin by Victor Hess in 1912, when, using balloon flights, he observed a regular increase of the density of ionizing particles with increasing height. Later in 1925 Robert Millikan coined the term cosmic rays for this radiation. Their corpuscular nature though was only discovered a few years later and now this term designates high-energy charged particles

originated in outer space, that eventually interact with the Earth's atmosphere and initiate extensive air showers (EASs) producing secondary particles. CRs are the most energetic particles known, they can reach energies up to 10^{20} eV and their study is a precious opportunity to understand the composition and evolution of the universe: which sites and mechanisms are responsible for their acceleration up to these high energies? However, since CRs are charged particles, they are deflected and diffused by interstellar magnetic fields and thus produce an isotropic source of charged cosmic rays reaching the Earth. Hence charged cosmic particles do not point back to their origin and CRs sources cannot be observed directly through CR measurements, since they generally loose the directional information during the propagation. The sources of CRs are still unclear and several candidates, both galactic and extragalactic, have environments that can accelerate these particles to those energies. Some of the potential sources include supernovae (SN) remnants, active galactic nuclei (AGN), quasars, pulsar wind nebulae (PWNe), binary systems and gamma-ray bursts (GRBs).

1.1.1 Spectrum and chemical composition

Cosmic rays have been deeply studied for more than a century in order to explain their origin, still under debate, and the processes that could accelerate these particles to such high energies, far exceeding those reached by the current generation of particle accelerators. Their energy spectrum, shown in Figure 1.1, extends from about 10^9 eV to 10^{20} eV and over more than 24 orders of magnitude in flux. Below ~ 1 GeV CRs have mostly a solar origin, since the solar magnetic field blocks most of the particles coming from outside the solar system. Above ~ 10 GeV the spectrum follows a broken power law distribution:

$$\frac{dN}{dE} \sim E^{-\alpha} \tag{1.1}$$

where α represents the spectral index which assumes different values in different areas of the spectrum.

The spectrum shows two features, the first, generally called *knee*, at $\sim 4 \cdot 10^{15}$ eV, the second, named *ankle*, is at $\sim 3 \cdot 10^{18}$ eV. Nowadays, it is widely believed that cosmic rays with energies below the knee have galactic origin and above extragalactic. The knee indicates the energy range where the galactic magnetic field cannot longer contain the energetic cosmic rays diffusing out of the galaxy, the transition area between galactic and extragalactic CR particles takes place up to the ankle. After the knee, the spectral index of the power-law changes from 2.7 to ~ 3 and above the ankle the spectrum hardens to a $\alpha \sim 2.6$. In the highest energy end of the spectrum at $\sim 5 \cdot 10^{19}$ eV, the interaction of protons with the Cosmic Microwave Background (CMB) radiation causes the GZK cutoff: it sets the theoretical upper limit on cosmic ray energy, and was theoretically predicted simultaneously by Greisen (1966) [3] and Zatsepin and Kuz'min (1966) [4]. Cosmic rays can be classified in primary and
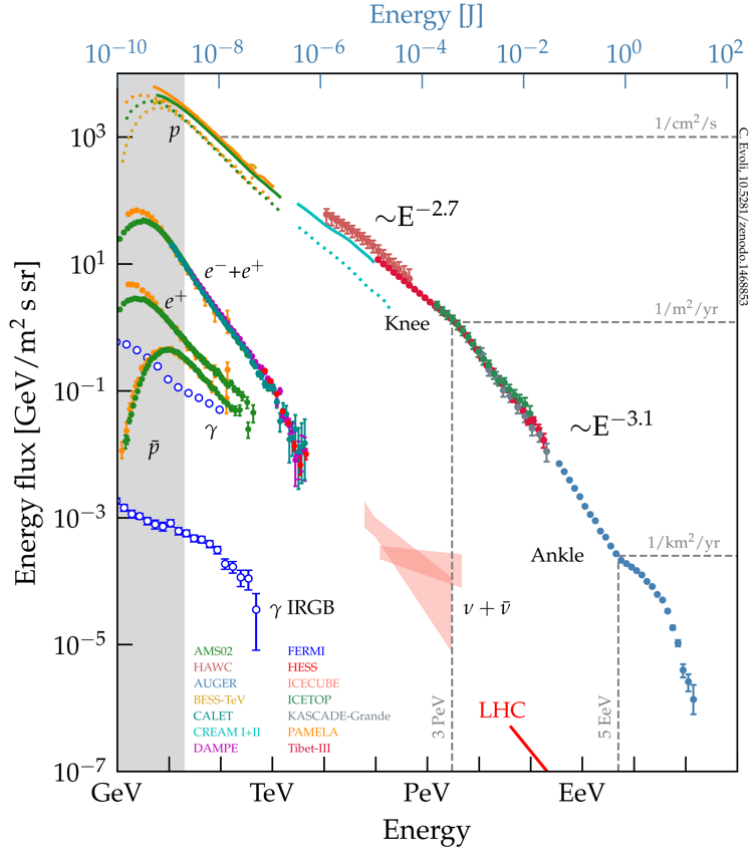
Figure 1.1: Energy spectrum of cosmic rays observed at Earth.
From [2]

secondary. The former are originally produced in various astrophysical processes and are composed mainly of protons and heavier nuclei (98%), with the remaining 2% of electrons [5]. Secondary cosmic rays, originated by the interaction of primary CRs with the Earth's atmosphere, include neutrons, pions, positrons and muons.

1.2 Gamma-ray astrophysics

In general, the term *gamma rays* denotes the electromagnetic radiation above some 100 keV; since they cover a wide energy range to beyond PeV, γ-rays are divided into several energy domains, shown in Table 1.1. This classification also reflects different techniques for the detection of gamma rays at different energies (see Section 1.2.2). Being neutral, gamma rays can travel long distances without being deflected by galactic and extragalactic magnetic fields, providing a useful tool to trace back CRs sources and investigate their acceleration mechanisms. They are of particular interest because they are produced in non-thermal processes.

This work is focused on Cherenkov telescopes and will thus primarily be concerned with VHE gamma rays.

Name	Energy
Low Energy (LE)	< 30 MeV
High Energy (HE)	30 MeV - 100 GeV
Very High Energy (VHE)	100 GeV - 100 TeV
Ultra High Energy (UHE) gamma rays	100 TeV - 100 PeV
Extreme High Energy (EHE)	> 100 PeV

TABLE 1.1: Energy domains of γ-ray astrophysics

1.2.1 Gamma-ray production

Gamma rays can be produced by radiative and collisional processes, in particular those involving the interaction of high-energy charged particles with nuclear targets or radiation fields. In this section I will briefly recall the main radiation processes, that allow the production of γ-rays of such high energies. For more detailed information, refer to [5].

Synchrotron radiation

Synchrotron radiation is emitted when relativistic electrons are deflected by magnetic fields and it can be observed over a wide range of energies, from radio to X-rays. In astrophysics, this is the most common interaction for producing non-thermal radiation, particularly X-rays. The accelerated relativistic electrons trace spirals following the magnetic field lines and synchrotron photons are emitted through an angle $\theta \simeq \frac{m_e c^2}{E}$ directed towards the electron circular motion.

In the context of VHE gamma rays, synchrotron radiation is the usual process for the generation of seed photons through synchroton self-Compton interactions (SSC).

Inverse Compton

The Compton effect consists in a transfer of energy and is often expressed as a change in frequency or wavelength. When a high-energy photon interacts with an electron, or any other charged particle, the photon transfers some of its energy to the electron and the result is a scattered photon with lower energy and longer wavelength.

In the case of a relativistic electron colliding with a low energy photon, the photon is up-scattered to higher energies at the expense of the kinetic energy of the electron. This is called Inverse Compton scattering. Most of the VHE γ-ray photons detected are produced by this mechanism.

Usually two different regimes can be distinguished, the Thomson limit, where the energy of the photon in the electron rest frame is lower than the electron rest mass energy, and the Klein-Nishina limit, where the energy of the photon exceed the rest mass energy of the electron in the electron rest frame:

$$\gamma E << m_e c^2 \qquad Thomson\ regime \tag{1.2}$$

$$\gamma E >> m_e c^2 \qquad Klein - Nishina\ regime$$

where E is the photon energy before the scattering process and γ is the Lorentz factor of the relativistic electron. In the Thompson limit the average energy of the scattered photons is $\langle E_\gamma \rangle = \frac{4}{3} E \gamma^2$, with a maximum energy of $E_\gamma^{max} \approx 4\gamma^2 E$.

This type of process becomes important in regions where there is a large density of photons and it is of great interest for astrophysics studies as it can produce very energetic photons and thus can explain the emission at high energies of some of the sources. In the case the photons emitted by synchroton radiation are scattered by the same electron population that produced them, the process is called synchroton self-Compton (SSC).

Electron Bremsstrahlung

This process occurs when charged particles are decelerated in an electric field of an atomic nucleus with a consequent emission of electromagnetic radiation. In astrophysics Bremsstrahlung emission might occur when a relativistic electron passes through a gas or plasma and is suddenly decelerated, resulting in an energy loss. Since the energy loss is proportional to the inverse of the particle mass, electrons are most efficient in producing Bremsstrahlung radiation. It is the dominant process for galactic diffuse γ-ray production up to $\sim 100\,\text{MeV}$.

Bremsstrahlung occurs when the energy of the charged CR, $E = \gamma m c^2$, is above a critical energy E_0 which depends on the crossed material. Below this value, the most efficient energy loss mechanism is ionization.

In addition to being an interaction process responsible for electron accelerated gamma-ray sources, Bremsstrahlung radiation plays an important role in the formation of the atmospheric showers, as will be described in Chapter 2, and it is then very important for ground-based gamma-ray astronomy.

Pion decay

Gamma rays can be produced from hadronic interactions as well, and the main mechanism is the collision of high-energy protons with matter, like the Interstellar Medium (ISM) gas, which produces almost the same amount of charged (π^+, π^-) and neutral pions (π^0).

While the charged pions decay weakly in muons and neutrinos, the neutral ones decay in two photons in most of the cases:

$$\pi^0 \rightarrow \gamma\gamma \tag{1.3}$$

If the kinetic energy of the original hadron is high enough, the photons emitted are of γ-ray energies.

Gamma rays can originate also from the interaction between protons and a sea of photons, coming for example from synchrotron radiation or from bremsstrahlung of accelerated electrons. This kind of interaction is called photo-production. It has a small cross section (fraction of mb) and it is therefore important in environments where the target photon density is much higher than the matter density.

1.2.2 Detection techniques

Two kinds of gamma-ray instruments exist: space-based and ground-based detectors. These two typologies are complementary. The experimental spectrum of gamma rays spans indeed 7 decades in energy and about 14 in flux, rapidly decreasing towards high energies. The larger is the energy, the larger should be the effective area, defined as the product of the geometrical area and the detector efficiency. Because of the cost of space technology, the geometrical area cannot however exceed $\sim 1\,\mathrm{m}^2$. This aspect makes space-based detectors more appropriate for measuring gamma rays in the MeV – mid-GeV energy range. Going to higher energies, large detection areas are needed and can be deployed only at ground, exploiting the fact that, for energies above $\sim 30\,\mathrm{GeV}$, the so-called electromagnetic air showers start to become detectable.

1.2.3 Gamma-ray absorption

While traveling from the source to the observer gamma rays can suffer absorption losses by interaction with cosmic matter and with the low-energy photon fields [6]. If the absorption by the interstellar and intergalactic matter is negligible due to the low matter densities, the same does not apply to absorption due to the low-energy photons of the Extragalactic Background Light (EBL), that can be relevant. In fact the Universe is almost uniformly filled with photons of the EBL that collide with VHE γ-rays, producing an absorption in the observed spectrum, increasing with the distance (redshift).

As the name suggests, EBL is, like CMB, a background. While the CMB conserves the structure of the Universe at the moment of decoupling of matter and radiation following the Big Bang, EBL is a measure of the entire radiant energy released by processes of structure formation that have occurred since the decoupling.

Until now, several different models of EBL have been proposed. The energy density spectrum of the EBL is characterized by two pronounced peaks. The first peak, known as the *stellar component*, is associated with light emitted by stars and it is redshifted through the history of the Universe. The second one comes from the re-processing of the starlight by dust and for this reason is called the *dust component*.

The process which VHE γ-rays undergo with EBL is the photon-photon pair production:

$$\gamma_{VHE}\gamma_{EBL} \longrightarrow e^+ e^- \tag{1.4}$$

It is an extremely relevant process for the observation of VHE γ-rays of distant sources. In fact beyond 100 GeV the Universe is not completely transparent to VHE γ-rays and this means that far distant sources cannot be observed.

The effect of the EBL absorption is energy dependent, therefore the original spectra get distorted and the measured spectrum must be deconvoluted. This attenuation can be described by an optical depth τ, as a function of the energy of the photon E_γ and the redshift z:

$$F_{obs}(E,z) = F_{int}(E)e^{-\tau(E_\gamma, z)} \tag{1.5}$$

where F_{obs} is the measured flux and F_{int} is the intrinsic spectrum of the source.

The EBL is difficult to measure directly due to strong foregrounds from our solar system and the Galaxy. Therefore, the observation of distant sources of VHE γ-rays using IACTs provides a unique indirect measurement of the EBL.

1.2.4 Sources of VHE gamma rays

Gamma rays are produced from many different sources, both galactic and extragalactic, through non-thermal processes. I will briefly give a description of the sources capable of accelerating γ-rays to these energies.

Galactic emitters

Due to their vicinity, galactic sources are often observed as extended objects in a vast range of wavelengths, and thus provide a unique opportunity to carry out studies on the morphology of the emission region.

Moreover, the γ-ray emission does not suffer absorption of cosmological background light. This eases the study of galactic sources, since they generally have luminosities of many orders of magnitude fainter than extragalactic ones.

Supernova remnants: A Supernova Remnant is the structure resulting from a supernova, an explosion of a massive star at the end of its life. When the initial mass of a star is big enough (mass > 1.5 $M_\odot$), it can collapse in an explosion which blows out a huge amount of material [7]. In the core a pulsar or a black hole is formed, depending on the mass of the remaining object, while the ejected material expands into the surroundings forming a shock wave that will interact with the interstellar medium (ISM). This forms a forward shock front compressing and heating the interstellar medium.

Furthermore the interaction of the shockwave creates a reverse shock moving back into the supernova ejecta. This supernova ejecta is known as the supernova remnant. SNRs are believed to be the main sites for CR acceleration

below 5 PeV, due to the Fermi acceleration processes that occur in the expanding shocks and create gamma radiation [8].

The best known and studied example of such systems is the Crab Nebula. The brightness and stability of its emission in the VHE γ-ray regime makes this source one of the most important sources used as standard calibration candle for ground-based and satellite experiments.

Pulsars: They are fast rotating neutron stars, emitting electromagnetic radiation periodically. Pulsars were first discovered through their emission at radio wavelengths, but they also emit X-rays and gamma rays.

A neutron star is a stellar remnant that is formed due to a gravitational collapse and could be the remaining core after the supernova event. They are extreme compact objects, that are only supported by the neutron degeneracy pressure. Their high spin rate, between a few milliseconds and some seconds, is due to the conservation of the angular momentum. Electromagnetic radiation is emitted along the magnetic axis but, for pulsars, the magnetic axis is not aligned with the rotational axis. This misalignment causes the periodic flux variations: the observer only sees an emission from a pulsar when the beam crosses its line of sight. Several models attempt to describe pulsars γ-ray emission. Gamma-ray emission is predicted to originate either from particle acceleration and subsequent synchrotron emission near the Polar Cap of the pulsar, or in the Outer Gap regions of the magnetosphere by inverse Compton scattering.

Galactic Centre: It is impossible to study the Galactic Centre (GC) in visible light due to the absorption by the interstellar dust, however, it becomes transparent for certain wavelengths such as radio and gamma rays.

The center of the Milky Way is crowded with many astrophysical sources in the γ-ray band. The most important GC γ-ray emitter candidates [9] are the super-massive black hole SgrA*, the SNR SgrA East [10] and the Pulsar Wind Nebula G359.95-0.04.

Binary systems A normal star with an accompanying neutron star, pulsar or black hole orbiting around a common mass center is a subgroup of binary systems. The heavy and compact companion can accrete gas and matter from the other star by its gravitational field. This flow is either turned directly into radiation (mostly X-rays) or collected in an accretion disc. The accretion releases gravitational potential energy, which heats up the gas to a hot plasma. The plasma generates very strong magnetic fields making a binary system an excellent particle accelerator and hence a source for HE and VHE gamma rays.
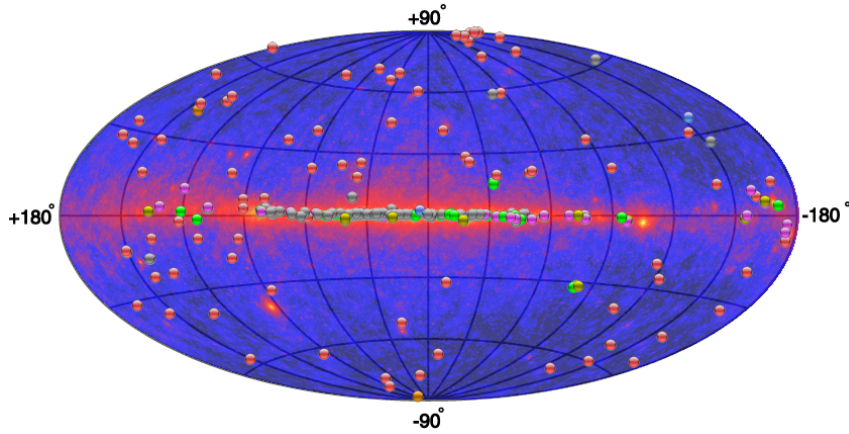
Figure 1.2: Extragalactic VHE γ-ray sources skymap overlapped with the Fermi skymap. Figure from `http://tevcat.uchicago.edu`.

Extragalactic emitters

Extragalactic sources are the brightest ones in the Universe and their study is essential to discover the distant past of the Cosmos. As already explained in Section 1.2.3, the Universe is not completely transparent to γ-rays, and due to their interaction with the photons of the EBL, γ-rays disappear via pair production. This is especially true in the case of distant sources, for which the flux of VHE photons reaching the Earth is strongly reduced, lowering the chances of detection. The current map of extragalactic emitters in the VHE domain above $100\,\mathrm{GeV}$ is shown in Figure 1.2 and most of them are Active Galactic Nuclei.

Active galactic nuclei: Active Galactic Nuclei (AGNs) are galaxies with a super massive black hole (SMBH) in their center. This super massive black hole accumulates great amounts of matter due to its huge gravitational attraction, forming an accretion disk surrounding the SMBH.

AGNs are usually classified into 2 broad types: Radio-quiet and Radio-loud. Radio-loud emission, originated from the BH, is beamed perpendicular to the accretion disk plane forming two jet structures accelerating particles to ultra-relativistic energies and producing electromagnetic radiation in the whole range of the electromagnetic spectrum. AGNs with their jets pointed towards our direction are called Blazars and this is the most common class of observed AGNs in the VHE domain.

Gamma-ray bursts: Gamma-ray bursts (GRBs) are very bright flashes of gamma rays, that last from fractions of seconds (*short GRBs*) to minutes (*long GRBs*) and occur with a frequency of about 1-2 per day [11]. They arrive from cosmological distances from random directions in the sky and are among the most violent and most luminous phenomena in the Universe. The energy released from a GRB is comparable to the energy our Sun releases in its entire life.

GRBs are characterized from an initial emission, called *prompt phase*, and are generally followed by an *afterglow*, a lower energy, long lasting emission in the X- ray, optical and radio. This delayed emission can last from days to years, according to the type of emission.

The two types of GRBs (short and long) have been associated to different progenitors: short GRBs are assumed to be caused by the merging of very compact objects, such as neutron stars or black holes, while long GRBs, the most common ones, are likely caused by massive stars explosions. In fact the first are located in regions with no star formation, instead long GRBs can be found in regions of rich star formation.

There are several models describing the GRB phenomenon, the Fireball model is nowadays the most widely accepted. According to this model GRBs are produced when the kinetic energy of an ultra-relativistic flow is dissipated. The GRB itself is produced by internal dissipation within the flow while the afterglow is produced via external shocks with the interstellar medium. Since the topic is strongly related to the work described in my thesis, GRBs are described in detail in Chapter 5.

1.3 Gravitational wave astrophysics

The search for Gravitational Waves (GWs) direct emission has been going on for several decades, but due to the weakness of the gravitational interactions their detection is very challenging. GWs were predicted by the General Theory of Relativity proposed by Einstein in 1915, and they can be described as perturbations in the curvature of space-time propagating at the speed of light. These ripples are created by masses in accelerated motion, and high-energy astrophysical systems have to be involved in their emission: sources must be compact and highly relativistic systems. Currently, GW direct detection is mainly based on laser interferometry [12], with the Laser Interferometer Gravitational-Wave Observatory (LIGO) and Virgo Collaboration, as the principal operating experiments. LIGO is composed by two almost identical detectors located in two sites, one in Livingston (LA, USA) and the other in Hanford (WA, USA). A third interferometer is planned to be installed in India (LIGO-India). Virgo is placed in Cascina (Italy). The interferometry technique consists in the detection of interferometric patterns generated by gravitational waves onto free masses. The separation L between two test masses is changed by $\triangle L$ due to a gravitational wave, resulting in an amplitude related to the GW. So if the two masses (mirrors) are placed in two perpendicular arms at the same distance L from a light source, a gravitational wave will change the length of the arms (depending on the orientation of the GW with respect to the detector) and also the measured light output will change accordingly. The signal of a GW from a binary black hole (BBH) coalescence was first detected by the two LIGO interferometers in 2015, and many others have followed in the three observation runs done so far

([13], [14]). A major milestone was achieved in 2017, when the LIGO-Virgo Collaboration detected the first gravitational wave signal from a binary neutron star (BNS) coalescence, GW170817 [15], in coincidence with an electromagnetic emission seen independently, among others, from both the Fermi Gamma-ray Burst Monitor and INTEGRAL satellites [16]. This observation has confirmed the model according to which short GRBs can be originated by compact binary mergers of this kind [17]. A more exhaustive description of this topic and details on its connection to this thesis are described in Chapter 3.

Imaging Atmospheric Cherenkov Telescopes

The Earth's atmosphere is opaque to electromagnetic radiation with energies above $\sim 3\,\text{eV}$ ($\lambda < 400\,\text{nm}$), and so it can be detected directly from the ground only in the optical and radio bands. As a consequence, direct detection in all other energy ranges requires detectors to be placed outside the Earth's atmosphere, usually on satellites or balloons. Conducting experiments above the atmosphere imposes restrictions and is costly: in space-based gamma-ray detectors the greater restriction comes from the size of the detectors and thus on the collection area.

So the detection of VHE γ-rays is carried out by ground-based experiments, although indirectly: only the products generated by the absorption of the gamma ray in the atmosphere are observed.

A primary particle, either a cosmic ray or a gamma ray, interacting with nuclei of the upper layers of the atmosphere, initiates a shower of secondary particles called Extensive Air Shower (EAS). These secondary particles are mainly energetic electrons, positrons and muons which produce flashes of Cherenkov light. In ground-based detectors the atmosphere is used as a calorimeter and becomes the medium within which the energetic particle interacts and attenuates.

Imaging Atmospheric Cherenkov Telescopes (IACTs) are ground-based detectors whose aim is to measure the physical properties of primary VHE gamma rays exploiting the Cherenkov light produced in the atmospheric showers induced by these gamma rays.

This chapter briefly summarizes the main properties of atmospheric showers and the subsequent production of the Cherenkov light, the technique used by IACTs and the main sources of background for this kind of detectors.

2.1   Extensive Air Showers

The first experimental evidences of atmospheric showers are associated to the name of Pierre Victor Auger. When a cosmic ray enters the atmosphere, it interacts

with atmospheric nuclei generating a shower of secondary particles. The shower's particles are strongly collimated along the direction of the incoming primary particle because of their relativistic energies. The physical processes involved in the showers development strongly depend on the nature and energy of the primary CR.

It is possible to distinguish between:

- *electromagnetic showers*, initiated by γ-rays or high-energy electrons;

- *hadronic showers*, induced by hadrons.

A shower can be characterized by the following main parameters:

- **shower axis**: flight direction of the primary particle;

- **longitudinal dimension**: distribution of the secondary particles along the shower axis;

- **lateral dimension**: distribution of the secondary particles perpendicular to the shower axis;

- **impact parameter**: distance of the shower center to the detector at the detector level.

The differences in these parameters, in the morphology and temporal feature of the shower development can be used to discriminate between the nature of the primaries. Therefore, these parameters are crucial for background suppression in the IACT technique, as CR induced EASs are more frequent than the γ-ray induced ones, constituting the main background in ground-based γ-ray astronomy. A view of the different development between an electromagnetic and an hadronic shower is shown in Figure 2.1, obtained from Monte Carlo simulations.

2.1.1 Electromagnetic showers

When highly energetic γ-rays or electrons interact with the atmosphere, electromagnetic showers are generated. The main physical mechanisms responsible for secondary particle production are the following:

- *pair production*, when the γ interacting with an atmosphere's nucleus converts into an electron-positron pair;

- *bremsstrahlung*, when an electron or positron deflected by an atmospheric nucleus radiates electromagnetic radiation.

These processes dominate the longitudinal evolution of the shower, while the multiple scattering of particles in the atmosphere determines its lateral distribution. An incoming gamma ray initiate an air shower by pair production and each
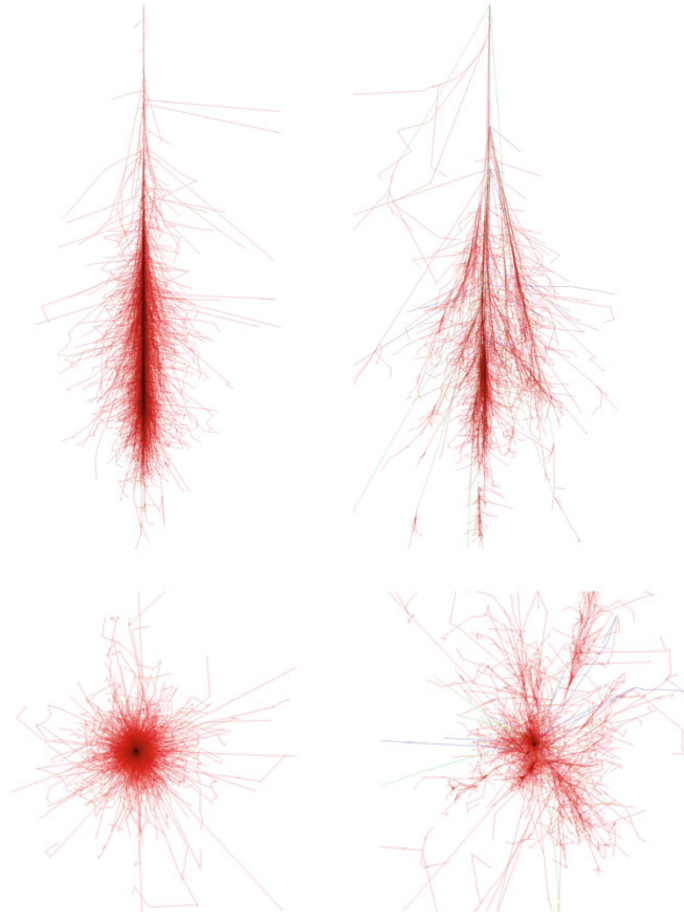
Figure 2.1: γ induced (upper left) and proton induced (upper right) shower for a $100\,\text{GeV}$ primary event simulated with CORSIKA [18]. The same showers seen on the transversal plane are respectively shown in the lower panel.

produced electron-positron pair radiates new photons via Bremsstrahlung decreasing their energy. These new gamma rays generate other pairs of e^-e^+, and so Bremsstrahlung and pair production alternate, giving rise to an EM shower as shown in Figure 2.2.

When the average energy per $e^\pm$ particle goes below a critical value E_c (in air $\sim 83\,\text{MeV}$), ionization losses start to dominate as energy decreases and the shower rapidly dies out. The height above sea level at which this happens is known as *height* of the shower maximum (h_{max}), and it is the height at which the number of particles produced by the EM shower is maximum. This height is inversely proportional to the logarithm of the energy of the primary gamma ray. The height can be also estimated considering the depth of the shower maximum (X_{max}) at which the maximum particles emission is reached, as shown later in Equation 2.4. It is measured in units of *radiation length* [1] and this occurs when the particles have

---

[1]The radiation length is the mean distance after which the charged particle's energy is reduced by a factor e due to bremsstrahlung radiation.
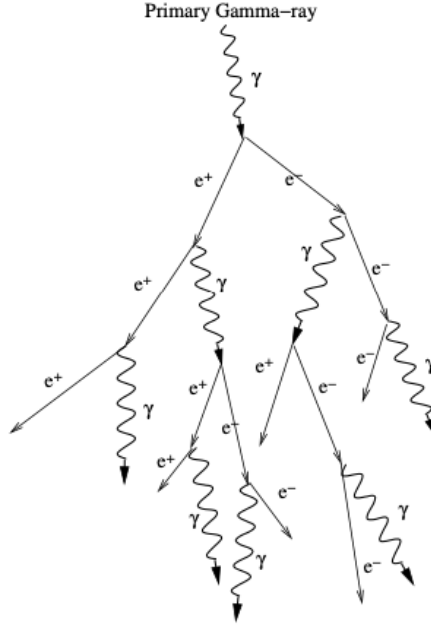
Figure 2.2: Scheme of a gamma-ray induced electromagnetic air shower illustrating the energy loss process by pair production and Bremsstrahlung. Image taken from [19]

an energy equal to the critical energy.

During the shower growth, the number of particles in the cascade increases but at the same time the energy per particle decreases, both approximately in an exponential way:

$$E = E_0 \exp^{-\frac{X}{X_0}} \tag{2.1}$$

where E is the average energy per particle, E_0 is the initial energy of the primary cosmic ray, X is the atmospheric depth and X_0 is the characteristic radiation length. Because of the very similar *radiation lengths* and *mean free paths* [2], the critical energies for pair creation and Bremsstrahlung radiation occur nearly simultaneously, although for $e^{\pm}$, the maximum number of particles is reached at slightly higher altitudes.

Heitler introduced in 1944 a simple model, which can describe in good approximation the characteristics of the longitudinal development of an electromagnetic shower (Figure 2.3).

The model makes two assumptions: the energy is equally distributed between the produced particles and the radiation length and the interaction length are equal. In this way the initial energy E_0 of the primary γ-ray is halved at every step among the produced particles, so the amount of particles N in the cascade after n radiation lengths X_0 is given by

---

[2]The mean free path of photons is defined as the distance covered by a population of photons after which their total number is reduced by a factor e due to electron-positron pair production.
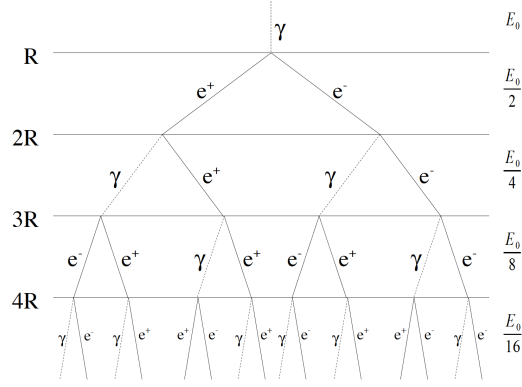
Figure 2.3: Heitler toy model for the development of electromagnetic showers extracted from [20]. Each level corresponds to one radiation length.

$$N = 2^n \tag{2.2}$$

while the mean energy per particle is

$$E_n = E_0 \cdot 2^{-n} \tag{2.3}$$

The maximum number of particles in a shower is $\simeq E_0/E_c$, so an approximation of the number of radiation length at which the shower maximum is reached can be obtained:

$$X_{max} = X_0 \ln \left(\frac{E_0}{E_c} \right) \tag{2.4}$$

A more accurate approximation of the longitudinal development of an electron/photon initiated shower, was given again by Greisen in 1960 [3]. Nowadays most calculations are performed by Monte Carlo methods.

2.1.2 Hadronic showers

The development of hadronic showers is quite different from the electromagnetic one, because the first interaction with an atmospheric nucleus is governed by the strong force and produces pions, kaons and other nucleons, depending on the initial energy of the incoming hadron (Figure 2.4).

As for electromagnetic showers, a simplified model can be constructed also for hadronic showers in order to understand qualitatively their development (see [21]). The hadronic radiation length λ is usually bigger than that for electrons, $\lambda > X_0$, therefore the hadronic showers are more penetrating and wider than the EM ones. In particular secondary particles have large transverse momenta, which makes the shower asymmetric if seen from the plane perpendicular to the shower axis.
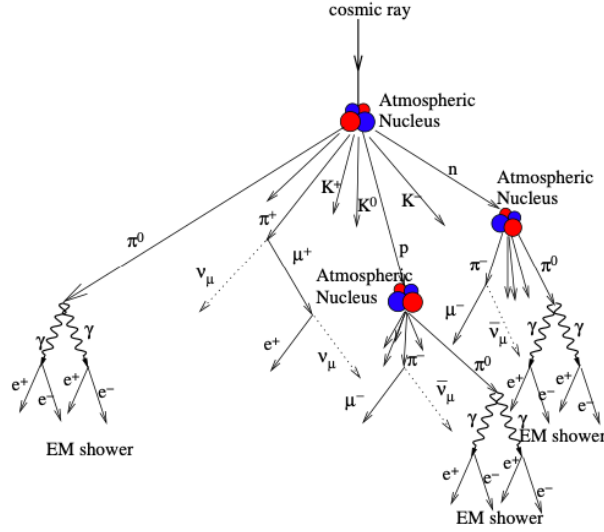
Figure 2.4: Hadronic particle cascade. Image taken from [19]

During the initial development of the shower, until the energy per nucleon is above the threshold for multiple pion production ($\sim 1\,\text{GeV}$), the strong interactions are the dominant processes and hadronic particles are created, whereas at the end ionization and decays become the dominant ones and the shower starts to die out. The shower can be divided in three parts depending on different interaction with matter:

1. The interaction of the primary hadron particle with the atmospheric nucleus gives rise to a multitude of particles such as charged pions and kaons, which decay into muons, neutrinos and other pions:

$$\pi^{\pm} \longrightarrow \mu^{\pm} + \nu_{\mu}(\bar{\nu}_{\mu}) \tag{2.5}$$

$$K^{\pm} \longrightarrow \pi^{\pm} + \pi^{0} \tag{2.6}$$

$$K^{\pm} \longrightarrow \mu^{\pm} + \nu_{\mu}(\bar{\nu}_{\mu}) \tag{2.7}$$

This goes on until the pion production energy threshold is reached.

2. The muons produced by the meson decay, generally lose energy through ionization and reach the ground with a large fraction of the initial energy due to the long muon free path. However they can also decay into electrons:

$$\mu^{\pm} \longrightarrow e^{\pm} + \nu_{e}(\bar{\nu}_{e}) \tag{2.8}$$

3. About one third of the produced pions are neutral, and they almost immediately ($\tau \sim 10^{-16}\,\text{s}$) decay in two photons

$$\pi^{0} \longrightarrow \gamma\gamma$$

adding an electromagnetic component to the hadronic shower.

These photons can produce EM sub-showers, which are practically indistinguishable from the EM showers initiated by primary photons discussed previously. However, the most striking background suppression comes by the fact that γ-ray showers point back to the source of their primary gamma ray, while the arrival direction of charged CR initiated air showers is isotropic.

A hadronic shower is therefore characterized by a core, which proceeds along the direction of the incident primary CR and by a number of sub-showers, both hadronic and electromagnetic, with high transverse momenta that make the lateral distribution of the hadronic showers much wider and irregular than the EM ones, as show in Figure 2.1. This is one of the main features which is used to discriminate between electromagnetic showers initiated by a gamma ray and hadronic showers initiated by a CR.

Cosmic e+ and e- initiate EM cascades similar to the primary gamma-ray ones, thus representing a small fraction of background.

2.1.3 Cherenkov light emission from EAS

The Cherenkov radiation was first discovered by Pavel Alekseevic Cherenkov in 1934 and a complete theory of this effect was later developed in 1937 by I. M. Frank and I. E. Tamm. Due to their work on this radiation phenomenon, in 1958 the Nobel Prize in Physics was given to Cherenkov, Frank and Tamm.

Cherenkov light is produced whenever a charged particle travels through a medium with a velocity v greater than the speed of light ($\frac{c}{n}$, with n refractive index) in that medium. A coherent wave front is produced by the induced medium polarization (Figure 2.5).

The total energy loss due to this process is negligible; however, Cherenkov radiation is important due to the possibility to use it in detectors. The emission angle of the radiation θ_{Ch} defines the Cherenkov light cone and can be derived from geometrical considerations as illustrated in Figure 2.6.

$$\cos \theta_{Ch} = \frac{\Delta t \cdot \frac{c}{n}}{\Delta t \cdot \beta c} = \frac{1}{\beta n} \tag{2.9}$$

The threshold condition for the minimum particle speed required to produce Cherenkov light in a given medium is $\beta_{min} = \frac{1}{n}$.

θ_{Ch} reaches the maximum in case of ultra-relativistic particles, when the particle velocity tends to the speed of light:

$$\beta = 1 \implies \cos \theta_{Ch}^{max} = \frac{1}{n} \tag{2.10}$$

A relation for the minimum kinetic energy of particles needed to produce Cherenkov radiation is then:

(a)

(b)
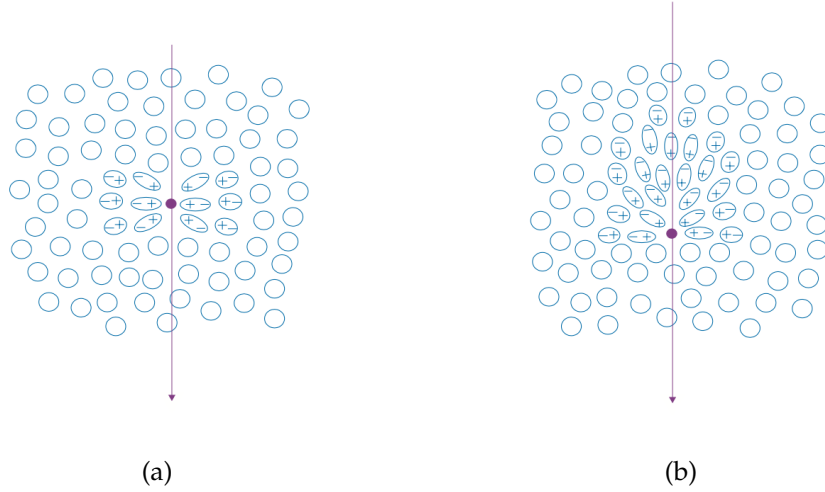
Figure 2.5: Representation of the Cherenkov effect: **(a)** Symmetric polarization induced by a particle moving with velocity $v < cn$. The orientation of the medium charges around the charged particle is symmetric, so no emission of light takes place. **(b)** The net polarization due to a charge moving at $v > cn$ creates a wave of radiation [22].

$$E_{threshold} > \gamma mc^2 = \frac{mc^2}{\sqrt{1 - \beta_{min}^2}} = \frac{mc^2}{\sqrt{1 - \frac{1}{n^2}}} \tag{2.11}$$

Equation 2.11 highlights the essential role of the medium in Cherenkov emission. In air the refractive index n is close to 1, but its value varies with the altitude: slightly lower at high altitudes and higher near sea level. At sea level $n \sim 1.00029$ and thus we expect the maximum emission angle to be $\theta_{max}^{Ch} \simeq 1.4°$, slowly decreasing with increasing height. For example, the Cherenkov angle decreases from $1°$ at 5 km to $0.66°$ at 10 km.

On the contrary, expressing the refraction index as a function of height in Equation 2.11, it can be shown that the energy threshold to emit Cherenkov light increases with height, and at sea level the energy threshold for electrons, muons and protons are 21 MeV, 4.4 GeV and 39 GeV respectively.

In case of a vertical air shower, the produced Cherenkov light illuminates typically a circular *light pool*, with a radius of ~ 125 m if measured at about 10 km above the sea level [23]. The light pool becomes more elliptic and distorted the more the impact angle deviates from the vertical incident direction. The view of the Cherenkov light pool on the ground, Figure 2.7, clearly shows a symmetrical circle on the ground for a high energy photon induced air shower, whereas the hadronic shower light pool is not so well defined and the effect of the electromagnetic subcascades are clearly visible. This provides a method of distinguishing hadronic
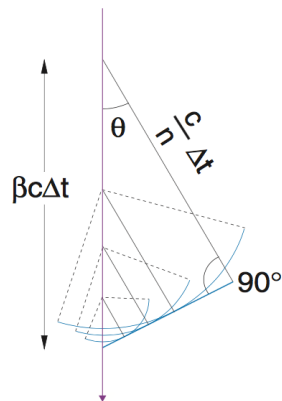
Figure 2.6: Geometric representation of the Cherenkov wave-front. Figure from [22]

from gamma ray initiated showers based on the distribution of light within the focal plane of the telescope. The area hit by Cherenkov photons is very large but, on the other hand, the photon density is very low (few photons per m^2 for a $100\,\text{GeV}$ γ-ray induced shower): this is the reason why ground-based telescopes need large light collection surfaces. Conversely, the lateral distribution of the Cherenkov light density for hadron induced air showers shows a completely different behaviour due to the differences in the shower development with respect to the electromagnetic shower case: it is peaked at small distances to the shower axis and decreases constantly.
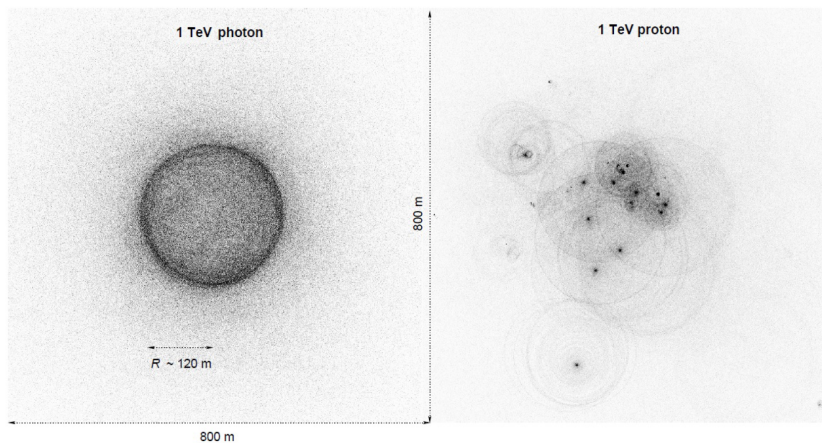
Figure 2.7: Simulated Cherenkov light pool of a shower from a primary gamma ray (left) and proton (right). Image from K. Bernlöhr.

2.2 Imaging Atmospheric Cherenkov Technique

One of the most challenging tasks for ground-based experiments in γ-ray astronomy is the discrimination between electromagnetic and hadronic showers: most of the recorded events are induced by primary hadrons, about three order of magnitude more than VHE γ-rays ones. Different techniques were developed, but the most successful approach so far is the Imaging Atmospheric Cherenkov (IAC) technique, that is employed to detect gamma rays by collecting the Cherenkov light of the electromagnetic cascade. Its principle is illustrated In Figure 2.8.

The time-scale of Cherenkov light is very short, just a few ns, so to overcome this first limitation, cameras equipped with high-speed photon multipliers (PMTs) are used. In addition to achieve a high sensitivity, a large collection area is required since the Cherenkov emission is very faint. Large reflecting surfaces are therefore placed inside the light pool to focus the light on the focal plane of the camera, which records the intensity and the temporal development of the Cherenkov flash.

The photons, coming from different parts of the shower, will reach the pixels located in different regions of the camera depending on the angle between the telescope axis and the incoming photon direction.
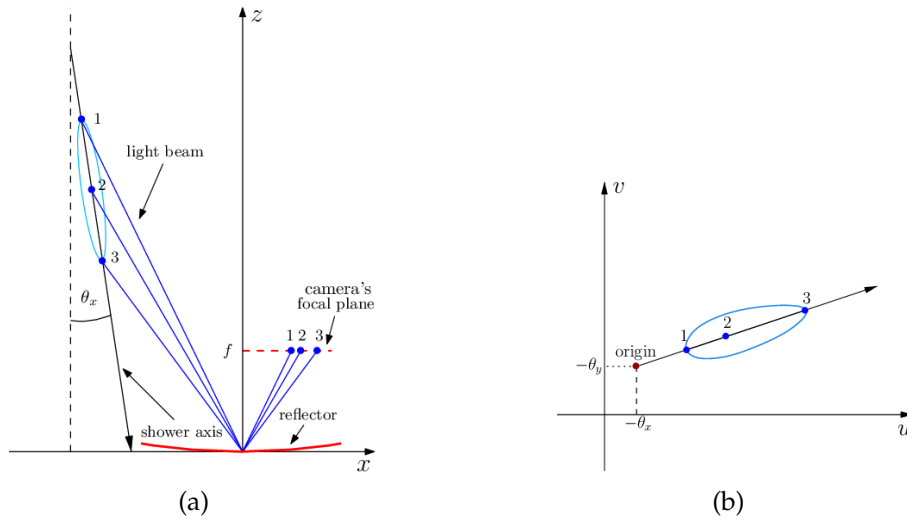
Figure 2.8: Basic observation principle of an IACT. The Cherenkov photons propagate to the ground at increasing angle with increasing shower development. The Cherenkov light is collected by the reflector and it is focused onto the focal plane. Its distance from the center of the camera reflects the shower impact parameter, i.e. the distance from the telescope axis (a). The camera is pixelized and the image can be reconstructed in the camera plane (b). Image adapted from [24]

A linear relation between illuminated pixels in the camera and incoming Cherenkov photons with an angle θ can be assumed under parallaxes approximation [3].

---

[3]Since IACT cameras acceptance is limited, the small angle approximation is well justified.

The longitudinal and lateral development of the shower will thus determine the image shape in the camera. For gamma-ray events the shape resembles approximately an ellipse, whose edges along the major axis represent the head and the tail of the shower, while the inner pixels correspond to its core (see Figure 2.8). In case of a hadron induced shower, the image is broader and more irregular because of the different shower evolution with more sub showers; it becomes a ring for muons. The shape, the orientation and light content of the image can be used to obtain information about the particle producing the air shower, such as the energy, the incident direction and the particle nature, allowing the selection of the γ-ray induced images.

2.2.1 Image parametrization

The electromagnetic shower image recorded by the PMTs of the camera can be parametrized by a set of parameters, called *image parameters*, originally introduced by A. M. Hillas [25]. These parameters are related to the distribution of the photons in the pixels, which constitute the image. Figure 2.9 illustrates how the Hillas parameters are obtained from the camera images of the Cherenkov air showers.
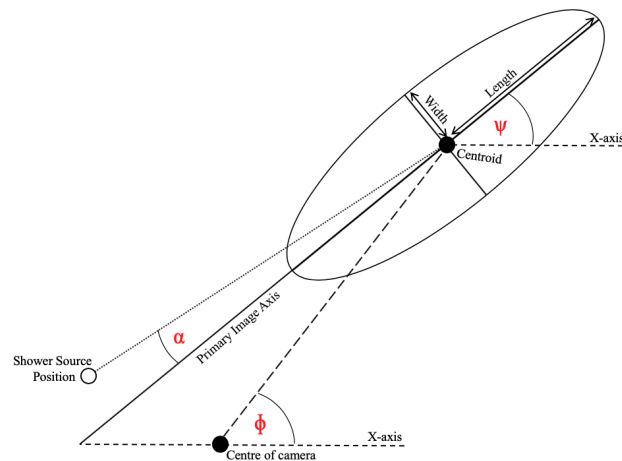
Figure 2.9: Graphical representation of some of the Hillas parameter described in the text. Credit to J.Watson

The assumption is that a shower image can be parametrized as an ellipse and each of these image parameters has a specific role in the discrimination against background events.

In the following the main parameters used in the reconstruction are briefly described, see also Chapter 4

Size Total charge, in photoelectrons (phe), contained in the cleaned image. It is very important in the energy estimation of the primary particle, since in first approximation, the parameter is proportional to the energy of the primary γ-ray if the shower impact point is close to the telescope (≤ 120 m).

CoG Center of gravity of the image. It consists of the coordinates of the position in the camera of the weighted mean signal along the X (*meanX*) and Y axis (*meanY*).

Lenght Lenght of the semi-major axis of the shower ellipse. This parameter is correlated to the longitudinal development of the shower.

Width Lenght of the semi-minor axis of the ellipse. It is a measurement of the lateral development of the shower. Since hadron showers have a wider transversal development with respect to gamma ones, this parameter is important in the discrimination of the nature of the primary. It is usually smaller for primary photons than for primary hadrons.

Conc(n) Fraction of phe contained in the n brightest pixels with respect to the total phe of the image (*size*). It is used to estimate the compactness of the shower and higher values are expected for γ-induced ones.

Number of island Number of isolated active pixels groups in the shower image that survive the cleaning. It gives an indication of the shower fragmentation. Hadronic cascades generally show a larger number of islands in comparison to γ-ray induced showers.

Leakage Fraction of signal contained in the external pixels of the camera. This parameter gives an estimation of the fraction of lost signal in case of a large impact parameter: high *leakage* value means that most of the event light is outside the camera. It allows to reject the event, if the image cannot be reconstructed correctly.

M3long Gives a measure of the asymmetry in the signal distribution along the major axis of the ellipse. It is useful to determine where the positions of the head and the tail of the event shower are.

Alpha Angle between the major axis of the ellipse and the imaginary line connecting the CoG with the real source position in the camera. It is possible to know α only if the source position is known.

Dist Angular distance between the CoG of the image and the source position in the camera. It provides an estimator of the impact parameter of the shower.

The last two parameters in the list above, *Dist* and *Alpha*, even if still connected to the physical properties of the shower, are strongly dependent on the expected position of the source. Instead the *Leakge* and *Number of island* are parameters used to evaluate the quality of the image. If the image is too noisy or not well contained in the camera is discarded.

Information about the time development of the shower is also taken into account in the analysis of the image. The arrival time in the image pixels of the Cherenkov

photons produced at different heights is not the same, because the Cherenkov light is slower than the particle propagating in the cascade. A discrimination between the *head* and the *tail* of the shower is essential to judge the location of the source. The *head* of the image points towards the incident particle direction. It is usually expected that the *head* of the image has a higher charge concentration than the *tail*, so the distinction between the two can be done using the asymmetry (parameter *M3long*) of the image along its major axis.

Once the images are parametrized, they can be tagged as hadron-like or γ-like through the γ/hadron separation (see Section 4.3.2) based on the values of their image parameters. Such an image reconstruction is only possible after the camera image has been cleaned from noisy and night sky background (NSB) light pixels, which do not belong to the shower.

2.2.2 Stereoscopic imaging

Individual telescopes provide independent images of the EASs (Figure 2.10). Ambiguity in the reconstruction could arise especially in key features like the primary particle direction or the core position. The reconstruction of the event and consequently the discrimination between gamma-hadron EAS can be improved by using an array of telescopes. Applying the IACT technique to more telescopes provides a view of the same shower from a number of different perspectives (*stereoscopic reconstruction*), and so enhances the geometrical shower reconstruction. Therefore IACT systems usually work in stereoscopic mode, that will also increase the sensitivity and the collection of photons due to the larger mirror area.

Each individual image from the telescopes carries information of a different projection of the same shower and their union considerably improves three main aspects of the analysis: gamma-hadron separation, direction and energy reconstruction. More telescopes increase the chances of discriminating electromagnetic cascades from hadronic ones, especially at lower energies where the distinction is more difficult, and they allow the detection of more Cherenkov photons. This, along with the improved impact parameter calculation due to the better reconstruction of the shower direction, causes the enhancement of the energy reconstruction too.

Furthermore, a stereo trigger system can be implemented if using multiple telescopes. The system stores only those events detected by several telescopes and allow the rejection of other sources of background, like muons and the local night sky background. A multi-telescope trigger will reject most muon events, because a muon creates a ring image close to only one telescope. It improves the rejection of hadronic induced events, since their Cherenkov light pool is non-uniform and the arrival time spread of the photons is larger than for gamma-ray induced events. A stereo trigger leads to a decrease of the trigger threshold of individual telescopes, raising the collection of photons at lower energy. The energy threshold, like the collection area, depends on the zenith angle of the observation (see Section 2.3.1).
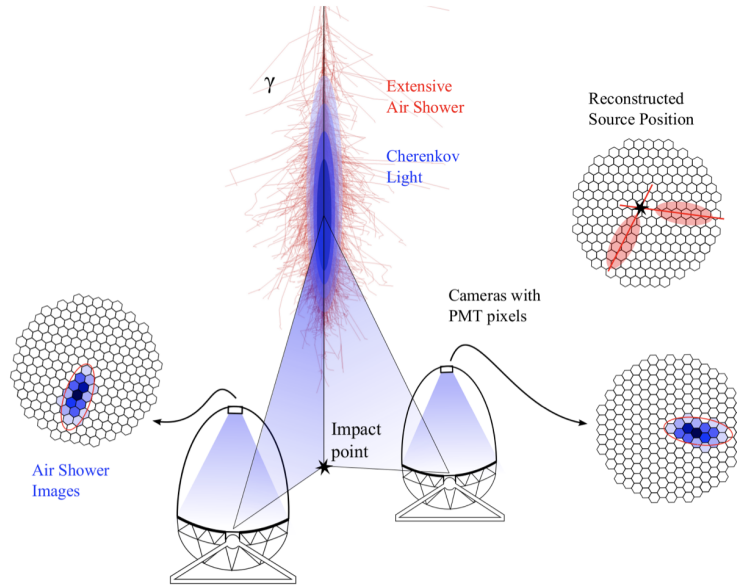
Figure 2.10: Illustration of the IACT technique in stereo mode. A gamma ray triggers an electromagnetic cascade in the Earth's atmosphere, which generates Cherenkov radiation in a pool on the ground. Telescopes within this light pool are used to form an image of the shower, which allows reconstruction of the arrival direction of the incident primary photon. Image from [26].

Other merits of a stereoscopic system are a reduction of dead time and an enhanced angular resolution thanks to the better reconstruction of the arrival direction.

2.3 Background sources for IACTs

Strong backgrounds reduce the sensitivity of the measurements of the Cherenkov light produced in the EAS induced by γ-rays coming from a given source. The most important sources of background for IACTs are:

Night Sky Background The Night Sky Background (NSB) is basically the visible light coming from the diffuse scattered light from stars, clouds, moon light or artificial sources. These photons can mimic low energy events, creating accidental triggers easily suppressed in the analysis, but affecting the data acquisition performance.

Hadrons Hadronic showers constitute the most prominent background of IACTs' measurements. Hadrons arrive almost isotropically in the atmosphere, therefore the background contribution will come from everywhere. It can be highly suppressed by an image analysis based on the image parameters because of

the difference mentioned before between hadron and gamma induced showers. The so-called γ/hadron separation efficiency can be larger than 99%, however, the hadronic background cannot be completely removed.

Muons They are produced within the shower and they emit Cherenkov photons along their path through the atmosphere. However, muons are easily recognized because they usually form ring-like images on the camera plane. Still, Cherenkov light from single high altitude muons with high impact parameter (>50 m) can simulate γ-ray images of low energies and is often difficult to reject. Stereoscopic observation and image analysis can strongly suppress the muons contamination.

Cosmic e$^{\pm}$ Cosmic electrons and positrons with isotropic arrival direction are almost indistinguishable from gamma-ray primaries, as they also initiate EM cascades, identical to those produce by γ-rays.

Diffuse γ-rays This is another source of irreducible background composed by both galactic and extragalactic diffuse γ-rays coming from unresolved sources. It is very weak compared to the other sources of background, especially at VHE.

Electronic Noise Devices have an intrinsic electronic noise that cannot be eliminated and has to be taken into account when analyzing the data. It is referred as *dark noise* and it is present even when the camera is not illuminated. High electronic noise levels in pixels may be able to trigger the telescope. To suppress this noise, electronic needs to be characterized through dedicated data runs.

2.3.1 Large zenith angle observations
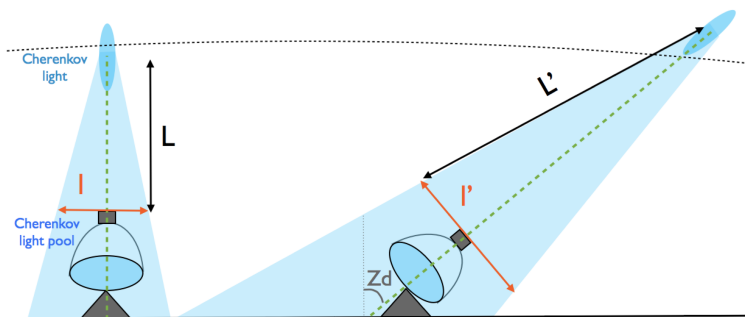
Figure 2.11: Sketch showing the working principle of large zenith angle observations: pointing to lower elevations the Cherenkov light pool increases and so the accessible collection area. Image from [27]

For observations at large zenith angles ($\theta \geq 45°$) the EAS development changes, as it increasingly takes place in the upper layers of the atmosphere, Figure 2.11. The shower has to cover a larger path to cross the atmosphere and this means a

larger attenuation, so the light pool on the ground will be larger, but the Cherenkov photon density at the observation level will be lower. This has a direct impact on the energy threshold and on the collection area, which then depend on the zenith angle of the observation. The reduction of Cherenkov light causes an increase in the energy threshold, with only higher energy showers triggering the telescopes due to the worst analysis of the images and the loss of discrimination power between hadronic and EM showers.

A positive effect that compensates the negative ones is the enlarged collection area of the telescope, which brings a better sensitivity.

Specific studies on observations at very large zenith angles were performed by the MAGIC Collaboration, see [28] and [29].

2.4 IACTs experiments

The first IACT to see significant signal (from the Crab nebula in '89) was Whipple in Arizona. The second generation of Cherenkov telescopes (HEGRA [30], CANGAROO and CAT) and the use of the stereoscopic technique improved the instruments performance. The last decades brought the third generation of telescopes, still operational, VERITAS [31] [32], HESS [33] and MAGIC [34] [35] (see Chapter 5), with better energy and angular resolution, larger cameras and dish diameters. A summary of the main parameters of the above experiments is shown in Table 2.1. The Cherenkov Telescope Array will represent the next-generation of VHE Cherenkov telescopes and will overcome a series of limitations affecting the current experiments. Both CTA and MAGIC experiments will be described further in the next Chapters of this work.

	N tel.	Alt. [m]	E_{th} [TeV]	FoV [°]	Ang. res. [°]	Sensitivity 50h [% Crab]	Dish $\varnothing$ [m]	Mirror area [m^2]
Whipple	1	2300	0.3	2.6	0.1	15	10	75
HEGRA	5	2200	0.5	4.3	0.1	5	3.9	8.5
H.E.S.S.	4	1800	0.1	5.0	0.1	0.7	12	107
H.E.S.S. II	1	1800	0.02	3.2	0.3	0.7	28	614
MAGIC	2	2231	0.05	3.5	0.08	0.7	17	236
VERITAS	4	1268	0.08	3.5	0.1	0.7	12	110

TABLE 2.1: Details of current IACTs experiments. Specifications of the first and second generation of Cherenkov telescopes are also reported to highlight the performance's progress.

Cherenkov Telescope Array

As mentioned in the previous chapter, the Cherenkov Telescope Array is the next-generation ground-based gamma-ray observatory. It will study the very high-energy gamma-ray sky in the GeV–TeV regime making significant progress over the existing Cherenkov observatories. [36] [37].

The aim of CTA is to improve the gamma-ray flux sensitivity by a factor of ten, with respect to the existing IACTs, in the currently accessible energy domain and to enlarge the detectable energy range to well below 100 GeV and to more than 300 TeV [38].

For energies above 1 TeV, CTA will be able to reconstruct the shower direction to an angular resolution of better than 2 arcminutes and the field of view (FoV) will be up to 10 deg, i.e. respectively a factor of 5 and over a factor of 2 better compared to the current instruments.

At lower energies there will be overlap with the energy range of the satellite instruments, and simultaneous observations with the Fermi Large Area Telescope are possible. The Fermi all-sky catalogue provides many sources for CTA to target and while Fermi observations complement CTA down to ~ 100 MeV energies, CTA will have a sensitivity for short-timescale phenomena that is orders of magnitude better than that of Fermi, as can be seen in Figure 3.1 where a comparison with the current gamma-ray telescopes is shown.

To provide full-sky coverage, CTA will deploy more than 100 telescopes between two sites, one in the northern and one in the southern hemisphere. To achieve the requirements in energy range and sensitivity, three different telescope types will operate together, each kind primarily covering a specific energy range: the Large Size Telescope (LST), the Medium Size Telescope (MST) and the Small Size Telescope (SST). A more detailed description of each telescope will follow in the next paragraphs.

The large number of telescopes will allow to operate with separate sub-arrays simultaneously with a sensitivity of current instruments or better. These can either be pointed at one specific known source or perform a survey with a series of pointings of a larger area of the sky. Furthermore, different pointing directions for
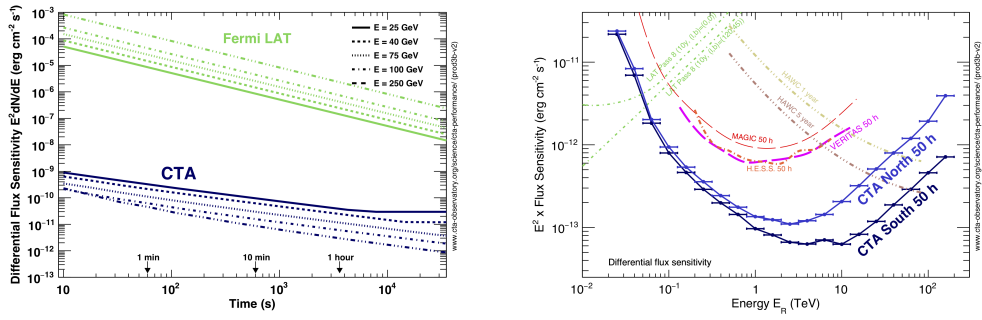
(a) Sensitivity vs Observation Time.   (b) Sensitivity comparison.

Figure 3.1: a) Differential flux sensitivity of CTA at selected energies as a function of observing time in comparison with the Fermi LAT instrument. b) Differential sensitivities for CTA-South and CTA-North as a function of energy compared with the current instruments one.. It is defined as the minimum flux needed to have five standard deviation detection of a point-like source in five independent logarithmic bins per decade in energy. The curves shown give only an indicative comparison of the sensitivity of the various instruments, as the method of calculation and the criteria applied are different. Images from https://www.cta-observatory.org.

different sub-arrays or individual telescopes will be possible: this work in particular will study the divergent pointing mode (see Chapter 6). These observing modes will provide a high degree of operational flexibility.

CTA's southern site will be located near the existing Paranal Observatory in the Atacama Desert in Chile, and will span the entire energy range of CTA, covering gamma-ray energies from 20 GeV to 300 TeV. This site, focused mostly on galactic physics, will host a larger array composed of 4 LSTs to ensure the low-energy reach of CTA, 15 MSTs to cover CTA's core energy range and 70 SSTs for the highest energies.

The northern hemisphere site will be located on the island of La Palma, in the Canary Islands, at the MAGIC site. The northern array will be more limited in size and will focus on CTA's low and mid-energy ranges from ~ 20 GeV to 20 TeV. The site will mainly concentrate on extragalactic physics and transient events and thus will not host any SST, only 4 LSTs and 15 MSTs.

The proposed telescope array layout of the two sites, shown in Figure 3.2 with the indication of the telescope positions on the ground, were defined through large scale simulations in the past years [39]. Since the beginning of the project five Monte Carlo productions have been generated and analyzed to define and optimize the telescope layouts, maximizing the performance while complying with CTA requirements.

The first two large-scale productions (called *prod1* and *prod2*) had the purpose to help in selecting the best site location and to explore a wide range of different
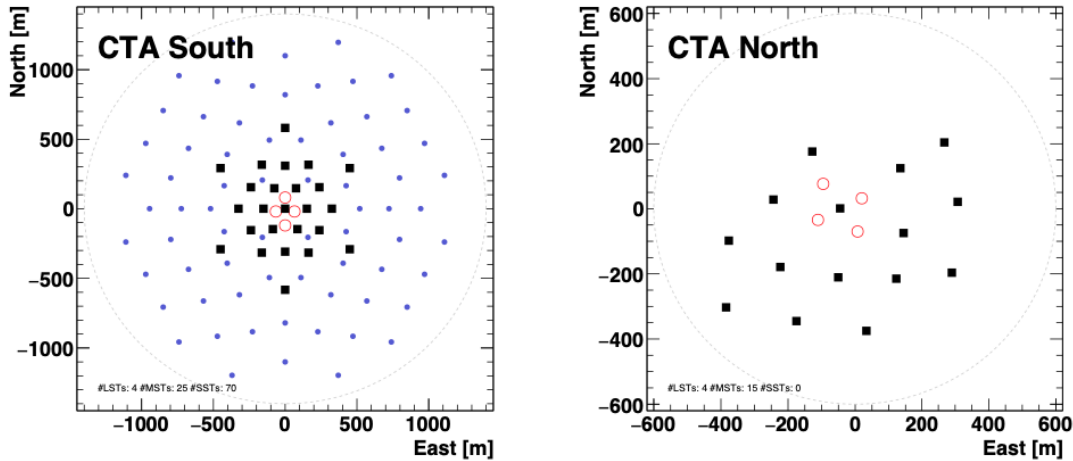
Figure 3.2: Schematics of the proposed baseline layouts of the northern and southern hemisphere arrays from the the so-called 'Production 3b'. LSTs are indicated by open circles, MSTs by filled squares and STSs by filled circles. Image from [40]

layouts, from compact ones, focused on low energies, to very extended ones, focused on multi-TeV energies [41] [42]. The study performed on these productions, together with other practical constraints, allowed to decide on the sites mentioned above, showing that sites at a moderate altitude (~ 2000 m a.s.l.) would give the best overall performances.

The third large-scale production (*prod3*) was generated in order to find the best telescope positions for the final layouts. The telescope design and camera type available were also updated to a more realistic and detailed model thanks to the input coming from the teams building the prototype telescopes in the meanwhile. This third production was updated in 2017 (*prod3b*) with small changes mainly in the telescope positions, especially for the La Palma site because of the restrictions imposed by the local topography. All the simulations and analysis done in this work are based on the *prod3b* layout configuration.

prod3b was followed by *prod4*, specifically done as support for the unification process of the SST design (see Section 3.1.3), hence the simulation was performed only for the Paranal site and didn't contain the other two telescope types. A new large MC production, namely *prod5*, with significantly improved MC model with respect to *prod3b*, is now under processing. Its goal is to optimize the final layout for both sites taking different constraints into account, and to deliver a more realistic estimation of the CTA performance.

3.1 CTA telescopes

The optical system of a Cherenkov telescope is mostly characterized by its reflector with its light collection capability and by the detecting camera, located in the focal plane, followed by the front-end electronics. To reach the large area needed to

gather as many Cherenkov photons as possible, the reflecting surface is composed by many mirrors of the same focal length. The use of tessellated mirrors permits to reduce the costs. The shape of the reflector is usually parabolic, preferred to a spherical one because it preserves the arrival time of Cherenkov photons emitted at a certain altitude, thanks to its isochronous properties. This reduces the time differences between photons reflected at different spots of the reflector, which also means an integration of less NSB noise. The downside of a parabolic shape is the higher construction cost of the single mirrors and the suffering of coma aberration, which makes the image look extended if looking off-axis. The mirrors are aligned by independent actuators to correct possible distortions of the telescope structure and mirror panels. The telescope mirror support frame is altazimuthal and allows to track a source in the sky moving in the azimuth and zenith directions. The camera is a crucial element and is composed by a large number of photo-detectors, which should be most sensitive in the same wavelength range where Cherenkov light is produced. They convert the Cherenkov light into an electrical pulse, amplify it and transmit it to the readout system. The electronics for signal transmission and triggering should provide a bandwidth compatible with the time duration of Cherenkov pulses of a few nanoseconds.

As already mentioned, CTA will host different telescope designs and their technical implementation details are briefly reviewed in the following paragraphs.

3.1.1 Large Size Telescope

The Cherenkov light produced by gamma rays of several tens of GeV is extremely faint and a large mirror is required to collect enough photons.

LST, inspired on the existing MAGIC and H.E.S.S. II IACTs, is the largest telescope in the CTA array with a 23 m diameter split parabolic mirror. It was designed specifically to cover the low-energy range of CTA from a few tens of GeV up to about a hundred GeV. It will also have a very good sensitivity up to several TeV, which is, however, covered by the Medium Size Telescopes more efficiently. Given the energy range, the major aims are transients, both galactic and extragalactic, pulsars and studies of the Extragalactic Background Light. In fact in the design of the telescope the study of GRBs was one of the driving goals: despite a mass of ~ 100 tons, LST can repoint by $180°$ in less than 20 seconds, so as to detect GRB's prompt emission.

The proposed baseline option is an array of 4 LSTs for both CTA sites, placed in a compact configuration with inter-telescope distances of about 150 m. The first LST prototype (LST1), shown in Figure 3.3, was inaugurated in October 2018 and it is currently under commissioning operations [43].

The telescope has an altitude-azimuth mount, supported by a tubular structure made of reinforced carbon fiber and steel tubes, with a parabolic profile and a focal length $f = 28$ m, which leads to a FoV of about $4.5°$. In order to capture fainter Cherenkov light, LST has a reflective surface of about $400 \, \mathrm{m^2}$ that focuses

Figure 3.3: Picture of the first LST prototype in La Palma.

Optical Parameters

Reflector type	1-mirror, parabolic
Focal length	28 m
Dish diameter	23 m
f/D	1.2
Effective mirror area	370 m^2
Pointing accuracy	14 arcsec

Camera Parameters

Camera dimensions (LxHxW)	2.8 m x 2.9 m x 1.15 m
Weight	< 2000 kg
Number of pixels	1855
Pixel size	0.1°
Field of view	4.5°
Readout rate	7.5 kHz (required) 15 kHz (goal)

Table 3.1: Summary of the main LST parameters [43].

the light into a high-sensitivity camera composed by 265 Photo-Multiplier Tube (PMT) modules, intended to work at very high event rates in order to trigger as many events as possible. The LST's main parameters are summarized in Table 3.1.

3.1.2 Middle Size Telescope

MSTs will improve the sensitivity in CTA's core energy range 0.1–10 TeV down to a few mCrab. 15 MSTs are foreseen in La Palma and 25 in Chile: they will populate the central part of the layouts to improve the background rejection power by increasing the event multiplicity. The improved cameras and the increased number of MSTs with respect to the current arrays using similar telescopes, will indeed permit to collect more photons and to improve the angular and energy resolution for a better background rejection.

As the energy of the primary particle increases, the amount of Cherenkov light emitted by EASs raises and large telescope reflecting areas are not needed anymore, so MST optics is based on a modified Davies-Cotton (DC-MST) layout with

Figure 3.4: DC-MST prototype equipped with FlashCam in Berlin-Adlershof (left) and SC-MST prototype at the Whipple Observatory in Arizona (right). Figures from https://www.cta-observatory.org

a reflector diameter of 12 m, mirror focal length of 16 m and a PMT camera.

A novel dual-mirror Schwarzschild-Couder Telescope (SCT), that fully corrects spherical and coma aberrations while providing a large FoV [44], was proposed as an alternative design with a compact camera based on Silicon Photo-Multiplier (SiPM) [45]. A prototype of both these designs, shown in Figure 3.4, was built and tested.

These two configurations are very different from one another, not only regarding the structure and optics design with the SCT having two mirrors, a primary of 9.7 m and a secondary of 5.4 m, but also for what concerns the camera [46]. For the DC-MST two camera concepts have been developed and tested on the prototype in Berlin, namely FlashCam [47] and NectarCam [48], equipped with 1764 and 1855 PMT-based pixels respectively. The SCT, instead, has a finer pixelization with 11328 SiPM, capable of recording the shower development with an excellent image resolution and necessary to obtain the improved angular resolution achievable with the dual-mirror design. The DC-MST is, as for now, the preferred design with still an uncertainty on the camera type; a summary of its characteristics is visible in Table 3.2.

Both the proposed telescopes will be able to rotate to any point in the sky above $30°$ in elevation in $< 90\,s$. This makes them less suitable than LSTs to detect transients prompt emission, but because of their larger FoV, they are better suited to perform a sky survey. Due to their multiplicity, MSTs are also the best candidates to perform sky survey in the so-called "divergent mode". The analysis done in

divergent mode is the center of this work and will be covered in Chapter 6.

	FlashCam	NectarCam
Optical design	Modified Davies-Cotton	
Dish diameter	11.5 m	
Effective mirror area	88 m^2	
Focal lenght	16 m	
Total weight	82 t	
Field of view	7.5°	7.7°
Number of pixels	1764	1855
Pixel size	0.17°	0.17°

TABLE 3.2: Summary of the main DC-MST parameters.

3.1.3 Small Size Telescope

The flux of γ-ray photons at energies > 10 TeV is very small: most of the non-thermal emission processes producing photons with such high energies are expected to produce fluxes falling rapidly with the energy, so the rate of VHE photons will be extremely small. To significantly detect them one has to increase the collection area, since VHE gamma-ray showers produce a large amount of Cherenkov light over a large area . Therefore the SSTs will be located in the outer parts of the array, in order to extend its effective area and to collect the maximum number of VHE photons.

SSTs will be placed only in the southern observatory, focused on galactic physics and interested in the highest γ-ray energies. At these energies the hadronic background is less predominant because of the steepness of the hadronic spectrum, a power-law with a 2.7 photon spectral index. The plan is to have 70 SSTs spread over 4 km^2, with an inter-telescope distance ranging from 300 m for the inner ones to more than 500 m for the outer ones in the array. With a field of view > 8° and an angular resolution of a few arcminutes, the SSTs will provide the highest resolution survey ever of the sky in this energy domain. This is crucial to understand the extreme particle accelerators in the Universe, establish the nature of the sources of galactic cosmic rays up to the knee and look for potential signals of new physics at the highest energies.

Three different SST implementations, shown in Figure 3.5, have been prototyped and tested: two dual-mirror designs, SST-2M ASTRI [49], with a prototype in Sicily, Italy, and SST-2M GCT [50], with a prototype in Meudon, France, and a single-mirror design, SST-1M [51], with a prototype built in Krakow, Poland.

All SST cameras are based on detectors utilizing Silicon photomultipliers technology, which, unlike photomultipliers, can operate during high levels of moonlight.

Currently, CTA is undergoing a harmonization process with the goal to converge on a single SST design for the production phase. Having only one SST type

| | (a) SST-2M ASTRI | (b) SST-2M GCT | (c) SST-1M |

Figure 3.5: Prototypes for the three SST proposed designs [36].

	SST-1M	**SST-2M GCT**	**SST-2M ASTRI**
Optical design	Davies-Cotton	Schwarzschild-Couder	Schwarzschild-Couder
Primary reflector diameter	$4\,\text{m}$	$4\,\text{m}$	$4.3\,\text{m}$
Secondary reflector diameter	-	$2\,\text{m}$	$1.8\,\text{m}$
Effective mirror area	$6.47\,\text{m}^2$	$7\,\text{m}^2$	$6.5\,\text{m}^2$
Focal length	$5.6\,\text{m}$	$2.3\,\text{m}$	$2.2\,\text{m}$
Total weight	$8.6\,\text{t}$	$8.1\,\text{t}$	$25\,\text{t}$
Field of view	$8.9°$	$9.6°$	$9.6°$
Number of camera pixels	1296	2048	2368
Pixel angular size	$0.24°$	$0.2°$	$0.19°$
Photodetector type	SiPM	SiPM	SiPM

TABLE 3.3: Summary of the main parameters of SSTs prototypes.

is important due to the large number of units to be built, operated and maintained during the lifetime of the array. To converge on the choice of the best SST proposal, a dedicated MC production (*prod4*) was performed: all the three designs were simulated, together with mixed configurations between ASTRI and GCT structures and cameras. In late 2019, the CTA Observtory (CTAO) decided that the CTA-SST design should be based on the ASTRI-CHEC design [1]. The Compact High Energy Camera (CHEC) is the camera initially designed for the SST-2M GCT model.

A comparison of the different characteristics between the prototypes can be seen in Table 3.3, where their main parameters are summarized.

3.2 Scientific goals of CTA

CTAO will be the first open observatory in VHE gamma-ray astronomy: a significant fraction of the available observation time will be dedicated to external scientists proposals and the data will be released as public after a proprietary period of one year [52]. The core program for CTAO proposed by the Consortium will be mostly dedicated to several Key Science Projects (KSP): Galactic Centre, Extragalactic Survey, Star Forming Systems, Galactic Plane Survey, Transients, Active Galactic Nuclei, Large Magellanic Cloud Survey, Cosmic Ray PeVatrons, Clusters of Galaxies. Together with the Dark Matter Program, they will enhance our knowledge of

[1]https://www.cta-observatory.org/small-sized-telescope-harmonization-process-and-status/

the high-energy Universe and provide some insight into the open questions of astrophysics, theoretical physics and particle physics. To address these themes CTA will exploit synergies with currently and forthcoming instruments seeking GW and astrophysical neutrino detection as well as with other photon observatories. Details on each KSP can be found in the document "Science with the Cherenkov Telescope Array" [53]. The science goals of CTA can be grouped in three themes:

Understanding the Origin and Role of Relativistic Cosmic Particles

As addressed in Chapter 1, in astrophysical systems like supernova explosions, galaxy clusters or active galactic nuclei, highly energetic particles play a major role. However, how cosmic rays can be accelerated to the highest energies and their impact in stars and galaxy evolution has still not been explained. CRs are believed to be an important regulator in the star formation process, through the ionization of the ISM material which affects the molecular cloud structure and star formation. With CTA's high improvement in spatial, temporal and spectral resolution, it will be possible to better understand CRs acceleration sites and the mechanisms involved (see [54] for a first quantitatively evaluation of CTA's capabilities in observing the accelerator RX J1713.7-3946, a young SNR). There is direct evidence that protons are accelerated in SNRs [55]: with CTA's Galactic and Extragalactic surveys other particle acceleration sites could be identified. Known TeV-emitting sources, such as Pulsar Wind Nebulae, gamma-ray binaries, massive stellar clusters, starburst and active galaxies will be observed in detail and CTA data will have a big impact in understanding these systems. CTA should also have the capability to search for the so far unidentified sources emitting particles at the PeV energies (PeVatrons) [56].

Probing Extreme Environments

Extreme environments like neutron stars and black holes are usually associated with the emission of VHE particles. Supermassive black holes in the center of active galaxies and stellar mass black holes produce collimated jets of relativistic particles when accreting surrounding material. The physical processes involved in the production of these jets are still an open question, so as the region of the black holes responsible for particle acceleration. The jets are believed to be sources of Ultra-High-Energy Cosmic Rays and CTA, together with observations in other wavelengths, will play a key role providing access to the inner regions of the jets and to their composition at VHE [57]. A source of high interest is the AGN Sgr A* at the center of our Galaxy. It is extremely difficult to distinguish its emission, probably coincident with a TeV source, from the diffuse emission around the Galactic Center, because of the insufficient angular resolution of the current instruments. This will be possible thanks to CTA's improved angular resolution. CTA will map the central region in high detail and with unprecedented sensitivity.

Exploring Frontiers in Physics

CTA will also try to address open questions in fundamental physics, such as the nature of dark matter. There are several observational evidences requiring that the Universe is dominated by the so-called cold non-baryonic dark matter. Among the favorite candidates are Weakly Interacting Massive Particles (WIMPs), which comprise non-baryonic particles with masses mostly in the range $\sim 10\,\text{GeV}$ - $10\,\text{TeV}$. According to the theoretical prediction, the annihilation of such particles should release secondary particles included gamma rays. The extended energy range and high sensitivity of CTA compared to existing IACTs, will increase the chances of detecting WIMPs annihilation.

CTA will search for axion-like particles (ALPs) too, and study a possible Lorentz Invariance Violation induced by quantum gravity effects on spacetime. Axions are a candidate for cold dark matter and are expected to convert into gamma rays. This coupling would result in an unexpected increase of the photons flux at TeV energies from sources at high redshift, that would be detectable by CTA.

In the next paragraphs I will address the topics relevant for this work and that I have been working on during my thesis: Extragalactic surveys and Gravitational Waves follow-up, as part of the Transient KSP. GRBs are one of the main targets of the Transient KSP and are related to this thesis, they will be discussed in Chapter 5.

3.2.1 KSP: Extragalactic survey

Surveys are a systematic and unbiased approach to observe the Universe. Observing the sky in an unbiased way, allows the discovery of unknown sources and provides legacy data-sets, particularly important for the relative new domain of VHE gamma-ray astrophysics. For these reasons surveys are pursued by all major facilities and also for CTA one of the main operations will be the completion of both a Galactic Plane Survey and an Extragalactic Survey. The latter consists of a blind survey of a quarter of the total sky, with three main objectives [58]:

1. Create an unbiased VHE extragalactic source catalogue with an integral sensitivity limit of 6 mCrab above 125 GeV.

2. Provide a high-resolution map of the extragalactic sky at gamma-ray energies between 50 GeV and 10 TeV.

3. Search for unknown and serendipitous VHE phenomena over a large portion of the sky. The area covered by the Extragalactic Survey will also connect to the Galactic Plane Survey so that all Galactic latitudes are covered.

The northern CTA site, which is more centered on the middle-low energy range, will be well suited to perform an Extragalactic Sky Survey: it will detect distant

VHE sources, which are significantly affected by gamma-ray absorption due to the EBL especially at the highest energies.

However, both sites are required to access the whole extragalactic sky. Due to the larger number of MSTs and the presence of the SSTs, the southern array sensitivity above 100 GeV will be better than the northern array (from MC estimations, see Figure 3.1). In order to compensate for this difference in sensitivity the northern site needs an exposure time approximately two times longer and thus the idea is to use both CTA sites for the Extragalactic Survey. It will allow to complete the survey to the required sensitivity (6 mCrab) within three years.

Such a survey has never been done by Cherenkov telescopes, because of the low observation duty cycle (night time and moonlight constraints) and limited field of view. However, thanks to an increased sensitivity to point-like sources and larger FoV compared to the current generation of IACTs, a VHE CTA survey would improve over the existing ones performed by other experiments like the Milagro and Tibet air shower arrays [59], or the High Altitude Water Cherenkov (HAWC) [60] below 10 TeV. At energies above this value, EAS array like HAWC or LHAASO (Large High Altitude Air Shower Observatory) will have a higher sensitivity for point-like sources [61] [62].

To cover the survey's area, the array has to perform a huge number of pointings and their duration is a crucial point in the achievement of the wanted survey depth (minimum source flux detectable) in the total sky. The biggest restrain comes from IACTs limited duty cycle and many studies have been carried out to determine the time needed for different science cases. To reach the target of 6 mCrab for point-like sources over the 25% of the sky, it is estimated that CTA will need to allocate 1000 hours [53].

These surveys can be performed in various observation modes, in particular, the large number of high-performance IACTs allows for using non-parallel modes (each telescope, or a sub-array pointing to a different part of the sky) with an enlarged FoV.

The proper adaptation of such a mode for a specific telescope array is challenging. The optimization of the pointing strategy, taking into account numerous characteristics of an array, e.g. distance between telescopes, field of view, energy threshold etc., can significantly reduce the observation time needed to achieve a given sensitivity. A proposed observation mode is the divergent pointing [63], which could bring benefits to both the Galactic and Extragalactic surveys due to the immediate increase of the total FoV. The larger field of view would increase the possibility of a serendipitous detection of a transient source within the observing area while the array is performing the survey (the possible detection of a GRB is 2-4 times higher in comparison to the parallel pointing [58]). It is however expected a worsening in sensitivity with the divergent modality [64]. Yet, if the source is bright enough even a worse sensitivity would be enough to detect it, allowing then a possible repointing of the array for a deeper observation. The study of the

performances of the northern array in divergent mode are discussed in Chapter 6.

3.2.2   Gravitational Waves follow-up

As anticipated in Section 1.3, Gravitational Waves are detected by interferometers. When an event is observed, a low-latency alert is sent to the other observatories via the Gamma-ray Coordinates Network (GCN), so that follow-up observations can be pursued. The GCN is the main system used to distribute information on transient alerts to the transient community. The information can be divided in GCN Notices, which contain the sky positions of the source detected usable by the observatories interested in performing a follow-up, and GCN Circulars, reporting about the results of the follow-up observations.

The sky localization of the GW event is done via triangulation. In the case of two detectors the result is an annulus in the sky if only the timing information is used. To restrict the localization to only some part of the annulus other informations, like the consistency of the signal amplitude, can be used. With more than three detectors, the timing information is sufficient to have a good estimation of the event localization, even if there is a significant difference in sensitivity between them, which leads to different accuracies in calculating the position. The sky localization of GW events detected during O1 and O2 runs of LIGO-VIRGO is shown in Figure 3.6
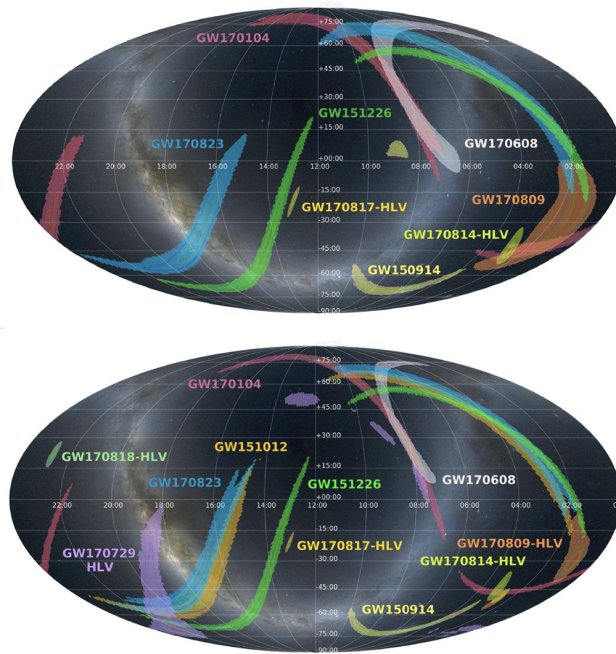

Figure 3.6: Sky probability map of all the GW events detected in O1 and O2. Top: location shared via GCN. Bottom: refined sky location after offline analysis, which identified three more events [65].

40

CTA will receive, as the currently EM observatories, the localization as a sky probability density map and will perform electromagnetic follow-up at VHE of the GW events, which means searching for EM emission inside the sky area provided by these maps. EM emission is expected from the systems generating the gravitational wave, so follow-ups are important because they could give complementary information about the source generating the signal.

The problem of follow-up for IACTs, given their limited FoV, is the enormous localization area provided by the GW probability skymaps, which can be as large as thousands of square degrees (deg^2): the worst sky localization between the eleven GW events shown in Figure 3.6 is the one of GW170823 with 1666 square degrees (TABLE III in [66]). CTA North, with the MSTs having the biggest FoV, can reach at most $50\,deg^2$, thus a strategy on the pointing pattern and the time spent per each pointing which would maximize the probability of detection is needed. More information about the GW follow-up with CTA can be found in [67].

With respect to other instruments, CTA will be favored in case of follow-up of GW alerts, due to its telescope multiplicity and larger field of view. Another advantage could come by performing the follow-up observations in divergent mode. The gain in field of view would allow to cover a bigger area of the localization map, reducing the number of pointings needed. Even if the sensitivity is expected to drop, after a detection alert of the on-site analysis the array could be repointed and the observation would be performed in parallel mode with better performance. The work pursued in this thesis will not examine the estimation of the benefit of the divergent pointing with respect to the standard pointing in the specific case of GW follow-up, which needs further analyses. It will however serve as starting point for the necessary analysis that have to be done based on the currently available tools.

Derivation of CTA Performance

The estimation of CTA performances is a long process, requiring massive MC production for the simulation of the shower, a software capable of simulating the telescope data taking and an analysis pipeline, whose output is the set of the so called Instrument Response Functions (IRFs). The IRFs describe the response of the array and strongly depend on the observing conditions and user-defined analysis parameters, which might be optimized for different science cases. They describe the reconstructed photon arrival direction ($\vec{p'}$), energy (E') and time (t') with respect to the true quantities, $\vec{p}$, E and t respectively [68]. Given a gamma-ray intensity of $I(\vec{p}, E', t)$, the expected event rate as a function of the reconstructed parameters is:

$$e(\vec{p'}, E', t') = \int R(\vec{p'}, E', t'|\vec{p}, E, t)\, d\vec{p}\, dE\, dt \times I(\vec{p}, E, t) \qquad (4.1)$$

where $R(\vec{p'}, E', t'|\vec{p}, E, t)$ describes the response of the instrument to a specific observation by associating the reconstructed quantities to their true value. It is generally factorized in effective collection area, point-spread function and energy dispersion:

$$R(\vec{p'}, E', t'|\vec{p}, E, t) = A_{eff}(\vec{p}, E, t) \times PSF(\vec{p'}|\vec{p}, E, t) \times E_{disp}(E'|\vec{p}, E, t) \qquad (4.2)$$

where

$$\int PSF(\vec{p'}|\vec{p}, E, t)\, d\vec{p'} = 1 \ , \ \int E_{disp}(E'|\vec{p}E, t) = 1 \qquad (4.3)$$

The background rates as a function of energy and position within the field of view is included in addition to the IRFs. The estimate of these quantities together with the sensitivity are the ultimate goal of the study of divergent simulations, in order to establish its performance with respect to the standard pointing mode.

In order to pursue the key science projects described in Chapter 3, certain standard, namely CTA requirements, must be fulfilled by all components of the observatory and they have to be considered in the calculation of the IRFs.

CTA's IRFs within different context are publicly available [1], for the latest results see Section 4.4.

4.1 CTA data level

It is relevant to this work to introduce a description of how data are handled in CTA, more specifically the *data processing level* definitions and the flow in between. The *data processing levels* indicate the progression of the data along the processing chain; their definition is important to ensure that each telescope adopts the same processing chain, so that compatibility between them and the pipeline framework software is guaranteed [69].

R0 (raw low-level) Raw waveform data. The content and format of the data is internal to each device.

R1 (raw common) Waveform data with calibration applied. The calibration is unique to each camera (camera-wise) and is needed to achieve a common data format between all telescopes. This and the previous level will exist only at electronic level and will not be saved.

DL0 (raw archived) Data received from the data acquisition software and intended to be stored in the CTA data center. Here data volume reduction may be performed on-site to meet storage requirements. These data are the first input for the analysis pipeline.

DL1 (calibrated) Processed DL0 data, calculated telescope-wise. The calibrated image charge and its characterization through the Hillas parametrization fall in this data level. This level is handled by the offline data processing pipeline, of which `ctapipe` [70] is a prototype. Details about this process are described in Section 4.3.1.

DL2 (reconstructed) At this stage the information is shower-wise and the one from individual telescope is not relevant anymore. DL1 products are used to reconstruct shower parameters including energy, direction, and source particle. This process is performed by the offline pipelines too, and for this work the prototype pipeline `protopipe` [71], based on the `ctapipe` library, was used. Further information about `protopipe` can be found in Section 4.3.2.

DL3 (reduced) List of selected events (eg. gamma rays, electrons or protons) with their set of reconstruction and discrimination parameters. Also associated IRF and any technical data needed to interpret them are given. Some quality cuts may be applied, according to the science goal which is being investigated.

---

[1] IRFs: https://www.cta-observatory.org/science/cta-performance/

DL4 (science) Higher-level science data products like spectra, sky-maps and lightcurves, enabling the analysis of astrophysical sources. They are derived from the CTA tools designed to support science data analysis. Two prototype have been developed: `Gammapy` [72] and `ctools` [73].

DL5 (high-level) From DL4 data legacy datasets, such as the CTA survey sky maps or the CTA source catalogue, are generated.

The quantity of data that the telescopes on the arrays will produce is expected to be of many hundred petabytes per years. Thus a package of software products to support this big flow of data is needed and each of them would be responsible for some data level [74]:

- **ACADA**: The Array Control and Data Acquisition System is the software supervising and controlling the telescopes of the array. The system will manage the data acquisition and compression of the raw data, as well as the generation of automatic science alerts. The ACADA also provides the user interface for the site operators.

- **DPPS**: The Data Processing and Preservation System will process the observed raw data into low-level science data products.

- **SUSS**: The Science User Support System will give access to the high-level data products and to the Science Analysis Tools needed to analyze them.

4.2 CTA simulation tools

Monte Carlo simulations are an essential tool for the design and optimization of Cherenkov telescopes. They are also required to interpret any VHE data beyond a detection, so simulations are very important for operation and scientific exploitation too. Unlike other experiments where the direct observation of γ-rays allows a straightforward calibration in test beams, the IACT analysis needs to rely on MC simulations to emulate the development of EASs in the atmosphere and the IACTs response. Starting with the energy, direction and nature of the primary particle, the cascade is simulated taking into account interactions and decays of the generated secondary particles, along with their corresponding Cherenkov emitted photons. Then they are traced in the telescope optics and the response of the camera pixels is also simulated, reproducing the camera electronics and readout systems. The simulated data are then used for gamma-hadron separation analysis, direction and energy reconstruction and performance studies. The final results of this process are the IRFs introduced at the beginning of the Chapter.

4.2.1 CORSIKA

The air-shower simulation is based on the COsmic Ray SImulations for KAscade (`CORSIKA`) code, widely used in the astroparticle physics community and publicly

available [75]. It is a Monte Carlo program to study the evolution and properties of EAS in the atmosphere initiated by photons, protons or any light nuclei up to iron. It was fundamental to learn how to use it in order to produce the simulations for the divergent pointing mode. Different interaction models can be implemented, in particular for this work the `CORSIKA` version used is the 6.990 (same one used for production *prod3b*); it uses the EGS4 code for electromagnetic shower generation and QGSJET-II and URQMD for respectively high (>80 GeV) and low-energy hadronic shower generation. In the later CTA's production `CORSIKA` was updated to version 7.6400, including the hadronic models QGSJET-II-04, SIBYLL, and EPOS.

The treatment of hadronic interactions is very complex and diverse models exist that may be activated optionally with varying precision of the simulation and consumption of CPU time. For an exhaustive description of the models and the possible customization of the physical parameters, please refer to `CORSIKA` documentation [2].

A mandatory extension for IACT simulations is the `IACT` option, needed to treat the Cherenkov radiation and to add more functionalities related to Cherenkov telescopes. The `IACT` package also allows to configure many physical parameters affecting the showers development and observed Cherenkov photons, like the observation altitude or tabulated atmospheric profiles, that include the density, the atmospheric thickness, and the effective refraction index as a function of altitude. To simulate a given array, the telescope positions on the ground should be provided as (x_i, y_i, z_i) coordinates with respect to observation level, and, in order to considerably decrease the `CORSIKA` output size, only photons hitting a sphere surrounding a telescope position are stored. A huge number of showers needs to be generated to properly estimate the CTA performance, and their computation requires a large amount of CPU time. To reduce the computing resources required, each shower is re-used at different random impact points on the ground with respect to the nominal shower core over a ground area with a radius defined by the option `CSCAT`. Generally for a performance study gamma, protons and electron are simulated. For point-like simulations the point of origin is fixed in the center of the field of view, however the protons and electrons are simulated in a diffuse manner. This way their point of origin is uniformly distributed across the field of view. This can be done by specifying a cone around the source position within which the diffuse particles can come (parameter `VIEWCONE`).

The large volume of simulations, dominated by those of proton-induced showers needed for background estimations, has motivated the use of the CTA computing GRID for the massive production of showers and detector simulations. In Table 4.1 an overview of the parameters and number of events used for production *prod3b* are reported.

---

[2]The latest `CORSIKA` User's Guide can be found at https://www.iap.kit.edu/corsika/70.php

	gamma (on-axis)	**proton**	**electron**
ERANGE [TeV]	$0.003 \div 330$	$0.004 \div 600$	$0.003 \div 330$
NSHOW	$2 \cdot 10^7$	$2 \cdot 10^8$	$1 \cdot 10^7$
VIEWCONE [deg]	0	10	10
OBSLEV [m]	2147	2147	2147
CSCAT [cm]	10 1400E2	20 1900E2	20 1900E2
CWAVLG [nm]	$240 \div 700$	$240 \div 700$	$240 \div 700$

TABLE 4.1: Typical parameters describing the MC air shower simulations for the La Palma site at 20 deg Zenith angle. In particular here are reported: the energy range ERANGE, the number of showers NSHOW, the cone around the primary direction from which the particles come VIEWCONE (useful for simulation of extended or diffuse emission), the observation level OBSLEV, the number of times a shower is re-used together with the maximum scattering of the core location along the X and Y direction in cm CSCAT, the lower and upper limit of the wavelength band for Cherenkov production CWAVLG.

4.2.2 Sim_telarray

In the second step of the CTA MC production, the atmospheric impact on the Cherenkov light transport as well as the details of the detector response is simulated with the sim_telarray software, mainly developed by K. Bernlohr for the High Energy Gamma Ray Astronomy (HEGRA) experiment and later on adapted and used by the H.E.S.S. experiment [76]. The software is highly flexible, each telescope is configurable independently and consequently, reflector and camera layout, readout and triggering schemes can be specified just by setting different configuration files.

Starting from the CORSIKA output, containing the arriving Cherenkov photons, sim_telarray simulates the transport through the atmosphere and the tracing of the Cherenkov light in the telescope up to its detection in the camera as well as the response of the camera electronics. The output of sim_telarray is the digitized pulse shape of the PMTs along with their calibration parameters such as pedestals or photoelectron conversion factors. It is as similar as possible to the real raw data format of an IACT, so that it can be directly analyzed from the latter format or converted into the specific formats of other Cherenkov telescope data analysis packages.

Regarding the divergent pointing work done in this thesis, the principal issue was understanding how to change the input cards of sim_telarray, since the pointing direction of each telescope had to be modified according to the pointing pattern, while the default pointing is unique and applied to all telescopes (see Section 6.2).

4.3 CTA analysis pipeline

The final CTA analysis pipeline, that will be used to derive the IRFs, will process both simulated data and real data recorded by the arrays to produce high-level data. At the moment it is still under development, therefore other non-CTA software,

`ROOT` and `C++` based adapted for CTA analysis, are used to study the performance: the MAGIC Analysis and Reconstruction Software (`MARS`) [77], main software analysis used by the MAGIC Collaboration, and `EventDisplay` used by the VERITAS Collaboration [78]. Their analysis is also used as cross-check to validate the results obtained with the pipeline in development.

As for now, the only real data available are the one from the LST prototype, the only telescope constructed in CTA north site. Therefore, the shown CTA performances are derived from MC simulations done at different Zenith and Azimuth angles. For each simulation different IRFs are produced at varying observation time, typically 50 hours, 5 hours, or 30 minutes.

The goal is to abandon these software packages for the next big MC production and for the analysis of the real data, and to replace them by a unique pipeline. The proposed concept is to use the pipeline called `protopipe`, which will exploit the library of other frameworks: `ctapipe` for the reconstruction of the events and `pyirf` [79] for the calculation of the performance.

So far IACT data are usually stored in `ROOT` files, readable only by proprietary software. CTA will be an open observatory, so the data and software have to be accessible to the astronomy community. For this reason the use of a common data format (FITS) for CTA data was chosen, that will allow joint analysis with other astronomical data sets. Moreover the analysis tools are mainly python-based, a programming language now very popular in data science, due to its extensive library of statistical and numerical open-source packages.

Currently, the merger of the work-flow in one pipeline is not completed and the three pipelines are still under development and tested independently, especially regarding `protopipe`, used for the data analysis in this work. As for now `protopipe` supplies a complete chain from DL0 to DL3 data.

In the following I will go through the description of the `ctapipe` framework, highlighting its major components and methods to perform an event reconstruction. I will then explain the whole `protopipe` chain and its spin-off `pyirf`.

4.3.1 `ctapipe`

To process and combine in a standardized approach the waveform data coming from each CTA telescope, the pipeline `ctapipe` is being developed by the members of the CTA Consortium [70]. It is intended to be a core library to be used later on in a full pipeline. The `ctapipe` framework is mainly written in Python, taking advantage of widely used open-source packages, such as `NumPy` [80], `SciPy` [81], `Astropy` [82], `Pandas` [83] and `Matplotlib` [84] to cite the most important and so avoiding the re-implementation of already existing methods.

Its development is being done via *GitHub*, an open-source system used mainly in software development for collaborative projects. This system allows an easy and simple interaction between the code contributors for the discussion of bugs and

improvement of the code. It also provides a documentation page where tutorials and examples are placed and can be freely used by other users.

ctapipe is still in evolution and the methods and classes defined in it can rapidly change or evolve. What I present in the following is referred to version 0.7.0 [85] on which protopipe v. 0.3.0 [71] is based.

Data Containers

In ctapipe, containers are used to store the data coming from the telescopes, independently of the camera type. The data are stored in a hierarchical structure (see Figure 4.1) that recalls the data processing level defined before in Section 4.1. This allows an easy reading and filling of the correct data level during the data processing.

```
ctapipe.containers.ArrayEventContainer:
              index.*: event indexing information
                 r0.*: Raw Data
                 r1.*: R1 Calibrated Data
                dl0.*: DL0 Data Volume Reduced Data
                dl1.*: DL1 Calibrated image
                dl2.*: Reconstructed Shower Information
          simulation.*: Simulated Event Information
             trigger.*: central trigger information
                count: number of events processed
            pointing.*: Array and telescope pointing positions
         calibration.*: Container for calibration coefficients for the
                        current event
                mon.*: container for event-wise monitoring data (MON)
```

Figure 4.1: Print result of an event, showing the content of the top-level container `ArrayEventContainer` and his hierarchical structure.

In case of MC data, classes for the simulated event exist, like `SimulatedShower Container` where the main information relative to the shower are stored.

EventSource

The class `EventSource` from the module `ctapipe.io` is used to read the telescope simulation files and it generates `ArrayEvents` when iterated over. Since the data format for camera prototyping was not unique, ctapipe had to be capable of reading them all. Thus a new `EventSource` can be created for each type of event file read. The data reading has been simplified thanks to the helper function `ctapipe.io.event_source`, see code snippet 4.1. Given an input URL, it automatically detects the type of file and, if it is compatible with the ones that ctapipe can read, returns the corresponding class. In case of `sim_telarray` files, class `SimTelEventSource` is called.

```
from ctapipe.io import event_source

filename = "example_file.simtel.gz"
allowed_tels = {1,2,3}
max_events = 100

source = event_source(input_url=filename, allowed_tels=allowed_tels, max_events=max_events)
```

LISTING 4.1: Simplified example on how the simtel files are read. The argument `allowed_tels` can be used if only certain telescopes (identified by a number ID) are wanted in the analysis, instead of the whole array (default option). `max_event` can be used to read only a number of events from the specified file. This option is usually used when tests are performed and it is not needed to read the whole file. In `protopipe` these arguments are passed through a configuration file defined by the user.

Raw data processing

The R0 data loaded contain the raw waveforms for each pixel in ADC counts. Each pixel has a low (LG) and a high gain (HG), with the latter the default one. To transform the signal from the R0 level to the R1 one, low-level corrections such as pedestal subtraction, timing and flatfield corrections are applied. This is done per each gain channel and time slice.

Successively when passing to DL0 data, gain selection is performed and calibration coefficients are applied to obtain photoelectrons from ADC counts. Here a data volume reduction is also performed, with the requirement that only $\sim 3\%$ of the pixels are kept, due to the large amount of data that CTA array will acquire. The algorithms that will be used to discard the noisy pixel and keep the ones with signal are still under discussion.

At this point the waveform is integrated over time, obtaining one final image with the number of photoelectrons per pixel along with the peak time after trigger in that pixel. The location of the peak is used as an estimator for the mean arrival time of the Cherenkov photons. The integration to extract the charge is by default done using class `NeighborPeakWindowSum`. In `protopipe`, based on a MARS analysis, the `TwoPassWindowSum` is applied instead. This is the DL1 level image, see Figure (a) of 4.2.

The passage from data level R0 to DL1 (R0 $\rightarrow$ R1 $\rightarrow$ DL0 $\rightarrow$ DL1) can be simply done using the class `CameraCalibrator`, which automatically runs the three calibration and trace-integration phases of the pipeline with the specified configuration and fills the *r1, dl0* and *dl1* containers of the event. If particular configurations are not specified, the default ones are used. If specific analysis have to be performed, the classes `R1Calibrator`, `DL0Reducer` and `DL1Calibrator` can be used separately to obtain the same result.

Treating simulated events, the assumption that all telescopes are well cross-calibrated is done. In case of real observations the calibration of the data is a

crucial passage that has to be done carefully to compensate environmental effects like temperature and humidity.

Image Cleaning

Before the full event reconstruction the DL1 image has to be cleaned, since the pixels still contain noise due to the background light and only those containing signal from the Cherenkov photons are of interest for the analysis. A double threshold algorithm is used: first pixels with photoelectron (phe) content above a certain threshold are selected as core pixels, and than neighboring pixels to the core ones above a second, lower threshold are also selected. This is the so-called *tail-cut* cleaning. The output of the cleaning algorithm is an array of boolean values where the pixels passing the cleaning are marked with `True` and the others are marked with `False`. The pixels surviving the cleaning can then be used to extract the geometrical properties of the air shower.

An example of applied image cleaning to an event seen by an MST equpped with NectarCam can be seen in Figure 4.2.

(a)   (b)

(c)
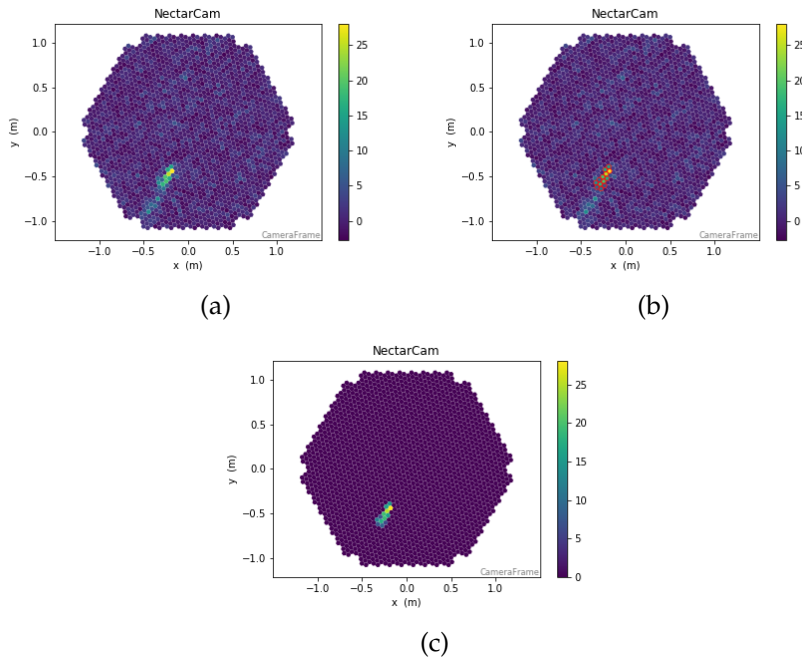
Figure 4.2: Example of a DL1 image before (a) and after (c) the cleaning. The pixels surviving the *tail-cut* cleaning are highlighted in red (b).

Shower Reconstruction

The pixels selected by the cleaning step can now be used to calculate the Hillas parameters which describe the shape of the Cherenkov emission (see Section 2.2.1).

The resulting shower image of a gamma is parametrized as an ellipse and its moments are calculated using the charge of each pixel as a weight (Figure 4.3). This is computed using the function `hillas_parameters` (block code 4.2).

```python
from ctapipe.image.hillas import hillas_parameters

camera = event.inst.subarray.tel[tel_id].camera
image_biggest, mask_reco = self.cleaner_reco.clean_image(pmt_signal, camera)

camera_biggest = camera[mask_reco]
image_biggest = image_biggest[mask_reco]

moments_reco = hillas_parameters(camera_biggest, image_biggest)
```

LISTING 4.2: Code snippet to show the application of the cleaning to the image and its parametrization. `image_biggest` is the cleaned image and `camera_biggest` the associated geometry. They are filtered with the mask used for the cleaning to speed up the computation.

The leakage parameter, amount of signal deposited in the border pixels of the camera, and the number of islands (group of isolated pixels) after the cleaning are also calculated.
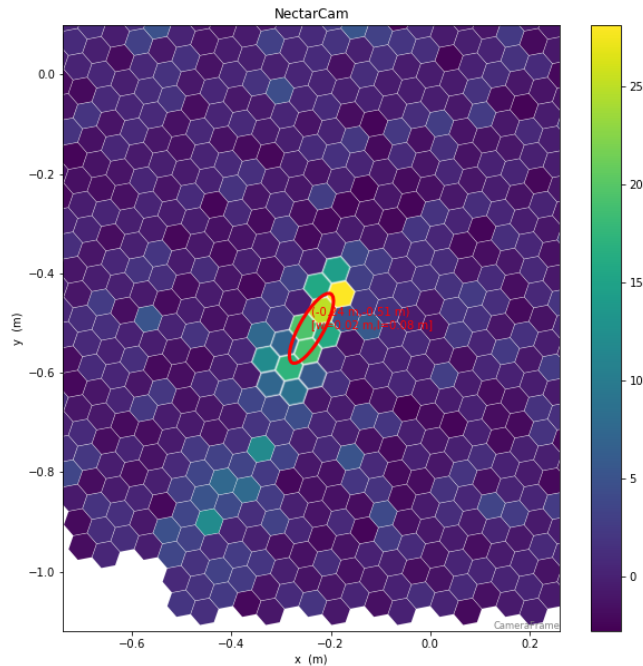
Figure 4.3: Zoom on the pixels that will survive the cleaning and will be parametrized as an ellipse.

At this point the stereo reconstruction can be performed for each event in order to find the primary particle incoming direction, the impact point of the shower on the ground and the height of the shower maximum lateral distribution h_{max}. This is executed by the class `HillasReconstructor` implemented in the module `ctapipe.reco`, which contains all the functions and classes needed to reconstruct the physical shower parameters. In a simple stereoscopic reconstruction the images

of each telescope are projected into a common camera coordinate system, and the intersection between each pair of major ellipse axes is calculated and averaged to define the point of origin on the sky. In `ctapipe` instead two points on the major axis in the camera are selected for every triggered telescope. One is the center of gravity, that by definition has to lie on the ellipse's major axis, the other one is selected at an arbitrary distance from the c.o.g. along this axis. These two points, defined in the camera frame, are transformed to a common coordinate frame relative to the local horizon (sky frame, the pointing direction of the telescopes are known). Thus they will be defined by altitude and azimuth coordinates. Together with the position of the relative telescope on the ground, a plane in the 3D space passing through them can be defined and the intersection between the planes gives the direction of the recorded shower.

In case of N telescopes used in the reconstruction, $N(N-1)$ intersections will be considered and the direction of the recorded shower is estimated by the weighted average intersection.The planes are first intersected pair-wise with the angle between each pair as weight. Successively the final reconstructed direction is obtained from the average of all the found pair-wise directions taking into account the weight of each plane and the angle between them.

From this method the h_{max} is estimated too. As mentioned in Section 2.1.1, h_{max} represents the moment where the amount of produced particles by the EM shower is maximum and it corresponds to the ellipse's c.o.g. From the horizontal frame, c.o.g coordinates are transformed to cartesian ones, and again together with the telescope position a line passing through them can be defined. h_{max} is then calculated as the closest point to a common intersection between all considered lines (Figure 4.4).
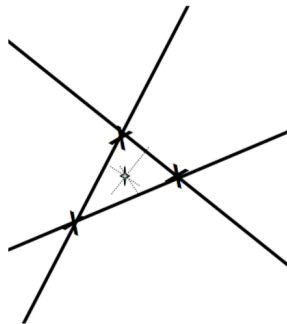

Figure 4.4: Closest mutual point to intersecting line method.

The impact point is estimated in a similar way by intersecting the major ellipse lines of each telescope and finding the closest mutual point. In case of simulations in divergent mode the method had to be adapted, see Section 6.3.

All the transformations and coordinate frames in `ctapipe` rely on `astropy` and the same convention are applied.

At the end of this pipeline the results are saved to disk in HDF5 format [86], which provides hierarchical binary storage with built-in compression capabilities.

Next step is the energy estimation and the classification of the particles. At the time of starting this work the class `EnergyRegressor` and `EventClassifier` (no longer present in the most up to date release v. 0.10.1 of `ctapipe` [87]) were just in testing, thus the choice to start using and developing the quite new pipeline `protopipe`, which had implemented both these estimations.

4.3.2 `Protopipe`

As already mentioned, `protopipe` is a pipeline prototype for CTA based on the `ctapipe` library. It has been first developed in the department of astrophysics at CEA-Saclay/IRFU and in late 2019 was open for development by other members of the CTA consortium. All the CTA public package is hosted on GitHub. The code is not stable and still under development. At the moment of writing the last release is tagged 0.3.0 [71] : a major update will be released soon, bringing important changes and improvement to the building of the models used for the energy reconstruction and classification, which I will describe. The pipeline is optimized for point-source analysis.

The list below gives an overview of the steps performed by the whole pipeline and the work-flow is illustrated in Figure 4.5:

1. **Energy estimator:** a table with gamma-ray image information is produced and used to extrapolate a model for the particle energy.

2. **Gamma/hadron classifier:** tables for both gamma rays and hadrons with image information are produced and used to build a gamma/hadron classifier.

3. **DL2 production:** production of tables for gamma rays, hadrons and electrons with event information after the implementation of the models obtained in the previous steps.

4. **Performance estimation:** optimization of the cuts and computation of the IRFs with consequential estimation of the energy.
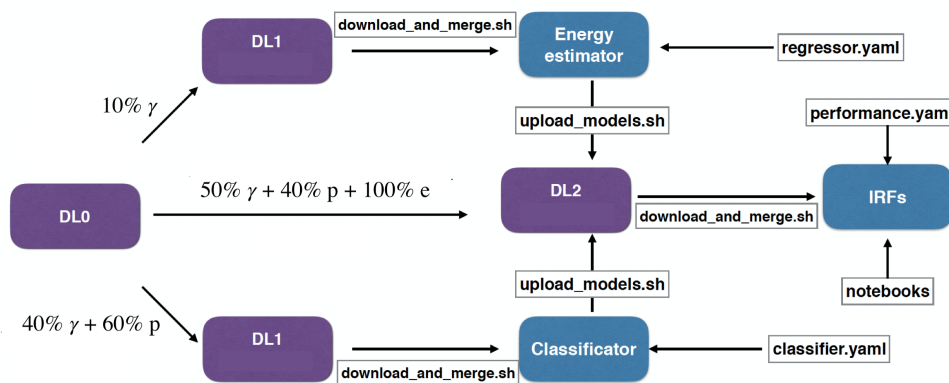
Figure 4.5: Scheme of `protopipe` work-flow.

DL1 data

The event processing to obtain tables with images information (DL1 data), follows what described in the previous section. The two main classes used are the `EventPreparer` class, which loops on the events to provide event and image parameters, and the `ImageCleaner`, which cleans the images according to different options. The algorithms and settings of this part of the pipeline were designed to mimic the CTA-MARS pipeline, with which a comparison is on-going to validate the results. Thus for the calibration process the class `ctapipe.image.extractors.TwoPassWindowSum` is used to extract the charge and pulse times, while the image cleaning is performed using as default the class `ctapipe.image.cleaning.mars_cleaning_1st_pass`, eventually changeable by the user. The MARS cleaning selects pixels that pass a three-threshold tail-cuts procedure, so the pixels that will be retained are:

- pixels that have a signal higher than the core threshold,

- pixels that are neighbors of a core pixel having a signal higher than the boundary threshold,

- pixels that are neighbors to a neighbor core pixel having a signal higher than the boundary threshold.

The default quality cut on the image selection are set as follows (settings are user-dependent):

- at least 50 phe,

- image's center of gravity within 80% of camera radius,

- ellipticity between 0.1 and 0.6,

- at least 3 surviving pixels.

Then the parametrization is done by `ctapipe.image.hillas.hillas_parameters`, while the direction reconstruction uses `ctapipe.reco.HillasReconstructor` with a minimum number of 2 surviving images per event.

Model training

Supervised learning algorithms [88], like Random Forests (RF, [89]) and Boosted Decision Tree (BDT,[90]), have been implemented during the last decade to determine the shower parameters from its image [91] [92]. These methods are used to estimate a target variable, called *label*, of an unlabeled event from a set of properties, *features*. A model can be created through a training process of a set of labeled events, like MC events, together with their features. The performance of the model
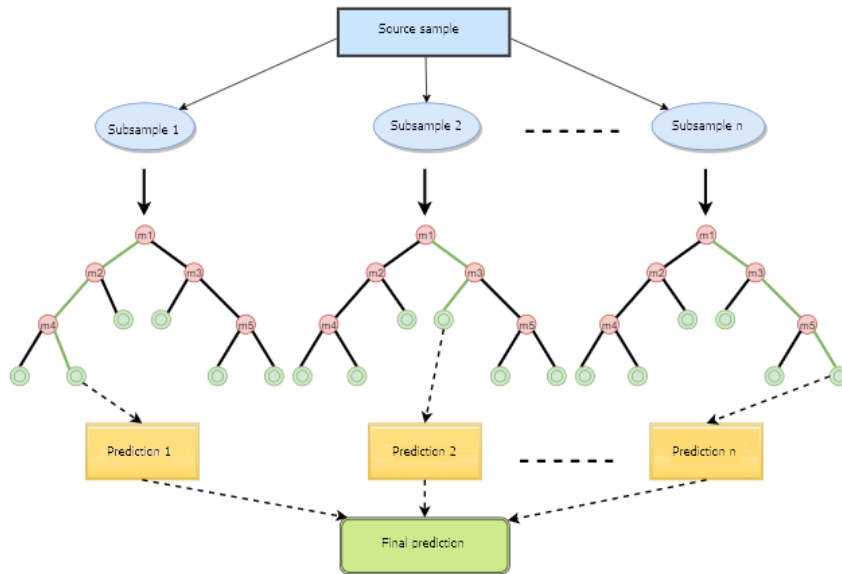
55

Figure 4.6: Scheme of a Random Forest operation: n random subsamples are selected from an original sample; for each subsample, a decision tree is constructed based on a random set of m features; results from all trees are gathered and averaged.

are evaluated with the help of a test set of labeled events, that has to be independent from the training set. The model can then be used to predict unknown labels in a new set of data not known to the algorithm.

In this case the label is the type of particle, gamma or hadron, or the energy of the incoming particle. In the former the algorithm is called *classification*, while in the latter is called *regression*. Normally Hillas parameters and other derived variables are used as features. The model parameters have to be optimized in order to reach the best performance, and even a small variance between training and test data can lead to significant different results.

With `protopipe` it is possible to build estimation models for both particle energy and gamma/hadron classification using a BDT regressor and a RF classifier both implemented in the module `sklearn.ensemble` of the `scikit-learn` package [93]. These methods are based on the creation of decision trees: tree-structured elements consisting of a series of splits using classification parameters (Figure 4.6). Trees start with a root node and then grow with repeating splits and nodes down to the final nodes, called *leaves*. A set of nodes and splits resulting in a leaf is called a *branch*. An event is classified according to the class label of the leaf at the end of the tree branch in which it ends up.

In case of the gamma/hadron classifier, the class `RandomForestClassifier` is used and parameters showing statistical differences in the shower development between gamma-ray and hadron induced showers are exploited as features: the second moments of the images, width and length, as well as the higher order skewness (measure of the asymmetry) and kurtosis (measure of the tailedness) are included,

together with the stereoscopic parameters height of the shower maximum and the reconstructed energy. The energy is important since the distribution of the discriminant parameters varies a lot with the energy of the particles. The inputs needed in the starting sample are a MC dataset of simulated gamma-ray events and a set of only hadronic events.

In the random forest the starting sample for each decision tree is bootstrapped from the original training dataset. Bootstrapping is a type of resampling where n samples are randomly selected with replacement from the original dataset containing n events: it allows to create new sets from a single original sample. The idea is that if you sample over and over again, your data should approximate the true population data. The method is commonly implemented when the statistic of the training dataset is limited and it would be difficult to divide it into as many independent sub-samples. The result of the RF is the average of the individual results of the decision trees and it will represent the probability that the event belongs to the class of gammas or the class of hadrons. The result covers the range from 0 to 1 (Figure 4.7): with a value of 0 the model estimates that the event is very likely an hadron one, while with a value of 1 is a signal event.

Some of the main parameters to adjust when using the RF method are `n_estimators` and `max_features`. The former is the number of trees in the forest. The larger the better, but also the longer to compute. In addition experience shows that the results will not significantly improve beyond a critical number of trees. The latter is the size of the random subsets of features to consider when splitting a node. In `protopipe`, `max_features` is set as the square root of the number of total features, while the number of trees is set at 200. The settings used are based on the ones in CTA-MARS analysis and are not yet optimized especially for non-parallel pointing. In case of parallel simulations a first optimization will follow from the comparison
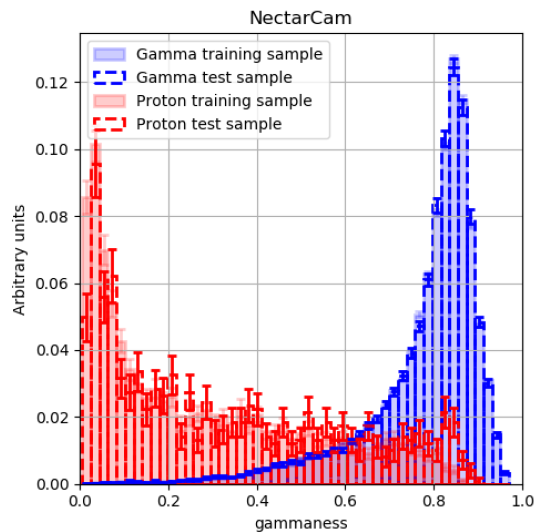
Figure 4.7: Example of the RF outcome for the MSTs, where the created model is applied to the testing set.
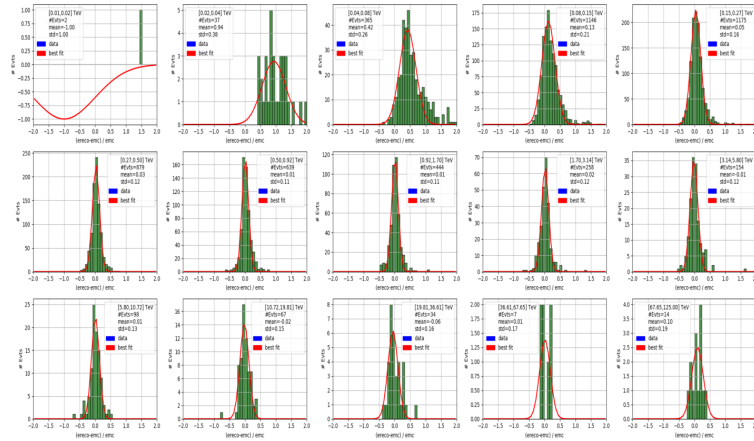
Figure 4.8: Example of the BDT outcome for the MSTs, where
the fit in different energy ranges is shown.

against CTA-MARS.

For the regressor, instead, a decision tree is boosted using the AdaBoost.R2 algorithm [94]. Simple features have been used to feed the regressor to estimate the energy, e.g. the charge, the width and the length of the images, the impact parameter and the height of the shower maximum. The method is similar to the RF, but with the main difference that the decision tree is built using the whole starting dataset and all the features of interest, which are not randomly chosen. Moreover the trees are not built in parallel, but in series: in the following trees the weights of the features are adjusted according to the error of the previous prediction. The core principle of AdaBoost is to fit the sequence of trees and at the end the predictions from all of them are combined through a simple majority decision to produce the final prediction (Figure 4.8).

Another approach for energy reconstruction commonly used by IACT is the use of look-up tables (LUT) [95], as done in MAGIC analysis. The implementation of this method is planned in the future release of the pipeline.

In `protopipe` features and other values to build both the models are passed through configuration files.

DL2 data and performance estimation

At this point the created models can be applied to the data to analyze and DL2 tables labeled with shower information such as the direction, the energy and the score/gammaness are created. The script used to generate them is similar to the one used for the DL1 reconstruction, and the same parameter values for the image selection are kept. In this step electron simulations are analyzed too. They will be added to the background together with protons to introduce some contamination. The tables are then merged into a unique one, that is used as input for the performance estimation.

The module `protopipe.perf` contains the tools needed to handle the determination of the best-cutoffs to separate gammas and background (protons + electrons), produce the IRFs and estimate the sensitivity with the help of `Gammapy` [96]. One contribution I did to the code together with Gaia Verna is the implementation of the functionality of `pyirf` to perform these operations, and accordingly changing `protopipe` variable notation. A new script that produces a DL3 file was introduced and a jupyter notebook is used to read this file and plot the performances. In the script the possibility of using the bootstrap method to evaluate the errors was added. In this case the number of bootstrap is defined in the configuration file `performance.yaml` and the average value together with its standard deviation are used as final value for the IRFs. These additions are not part of the master repository on GitHub cited for the analysis, but will be included in the next stable release of `protopipe`. The old scripts based on `Gammapy` functionality will be discarded. Thus all the final steps of the analysis were performed on a personal git branch.

In this thesis, the total MC data sample is split randomly following the same scheme adopted for the testing of the parallel simulation:

- training energy: 10% gammas

- training classification: 40% gammas, 60% protons

- data for analysis: 50% gammas, 40% protons, 100% electrons

4.3.3 pyirf

As mentioned above, `pyirf` [79] aims to provide functions to calculate IRFs and sensitivity for IACTs. The package is a prototype and a spin-off of the analog subprocess of the pipeline `protopipe`. It is still under development and changes to the source code, hosted on GitHub, are expected. Most functions need DL2 event lists as input and the main information needed in the DL2 tables with the appropriate units are:

- `true_energy` (TeV): True energy of the simulated shower

- `reco_energy` (TeV): Reconstructed energy of the simulated shower

- `reco_alt` (deg): Reconstructed altitude of shower origin

- `reco_az` (deg): Reconstructed Azimuth of shower origin

- `pointing_alt` (deg): Altitude of the FoV center

- `pointing_az` (deg): Azimuth of the FoV center

- `true_alt` (deg): True altitude of the shower origin

- `true_az` (deg): True Azimuth of the shower origin

- `multiplicity`: Number of telescopes used in the reconstruction

- `gh_score`: Gamma/hadron classification output

- `weight`: Event weight

Currently, `pyirf` allows calculation of the usual factorization of the IRFs mentioned at the beginning of this Chapter. Their implementation follows the definition given in the data formats for gamma-ray astronomy documentation [3]:

Effective Area It is a measure of the collection area of the telescope and is computed as a function of the true energy. It describes the efficiency of the instrument to detect γ-rays. The events which are considered are the ones passing the threshold of the best cutoff plus the angular cuts. The effective area increases with the energy and reaches a plateau at the highest energies.

Energy Dispersion It is defined as the ratio between the reconstructed energy E_R and the true energy E_T. It is represented by the width and the average of the distribution of the energy dispersion matrix. The events considered are the ones passing the threshold of the best cutoff plus the angular cuts.

Point Spread Function The PSF describes the probability of measuring a gamma ray of a given true energy and true position at a reconstructed position. So it describes the response of the detector to a point source. It is derived from MC simulation, but it can be also estimated from the observation of point sources, like AGNs.

Background rate The background rate is calculated as the number of background-like events per second, reconstructed energy and solid angle. The current version is computed in radially symmetric bins in the FoV.

The computation of point-source flux sensitivity and functions to calculate event weights, that are needed to translate a set of simulations to a physical flux for calculating sensitivity and expected event counts, are also implemented. Flux sensitivity is defined as the smallest flux an IACT can detect with a certain significance, usually 5σ according to the Li&Ma likelihood ratio test [97], in a specified amount of time.

4.4 *prod3b* results

CTA IRFs and high-level analysis software are public and usable by any user, even outside the CTA collaboration. IRFs were performed for both the North and South site and the full arrays shown in Figure 3.2 are considered. The analysis were evaluated for a point-like gamma-ray source located at the center of the FoV of each

---

[3]https://gamma-astro-data-formats.readthedocs.io/en/v0.2/

camera and with nominal telescope pointing. For each site the IRFs available are for 20°, 40°, 60° Zenith angle, for 0° and 180° Azimuth angle (pointing direction towards North and South respectively). The optimal cuts depend on the duration of the observation, therefore the IRFs are provided for three different observation times: 30 min, 5 hours and 50 hours. The plots presented in Figure 4.9 are the ones available at the CTA official site.
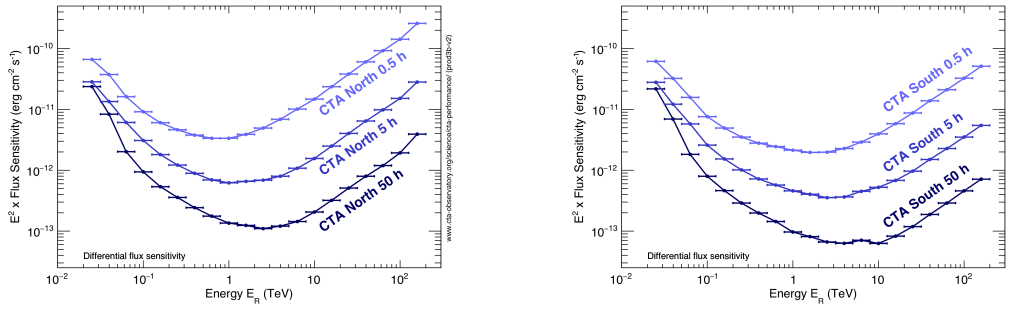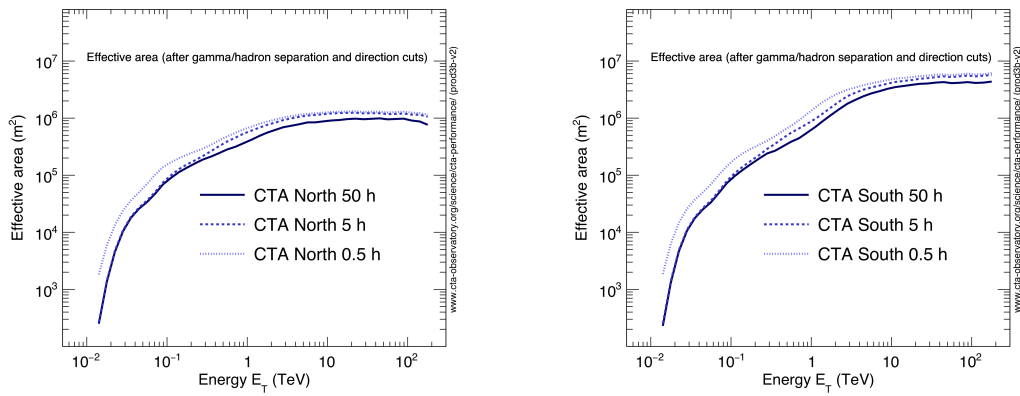

(a) Differential flux sensitivity for different observing times assuming a gamma-ray source located at the center of the field of view.
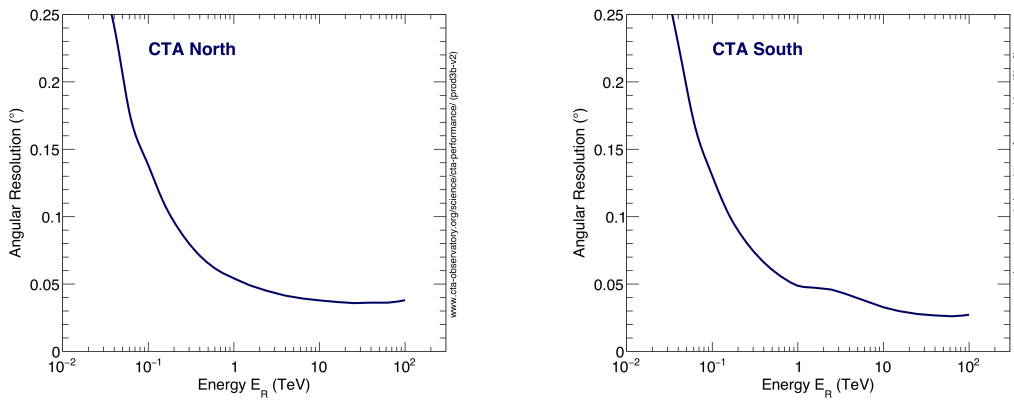
(b) Angular resolution vs reconstructed energy.
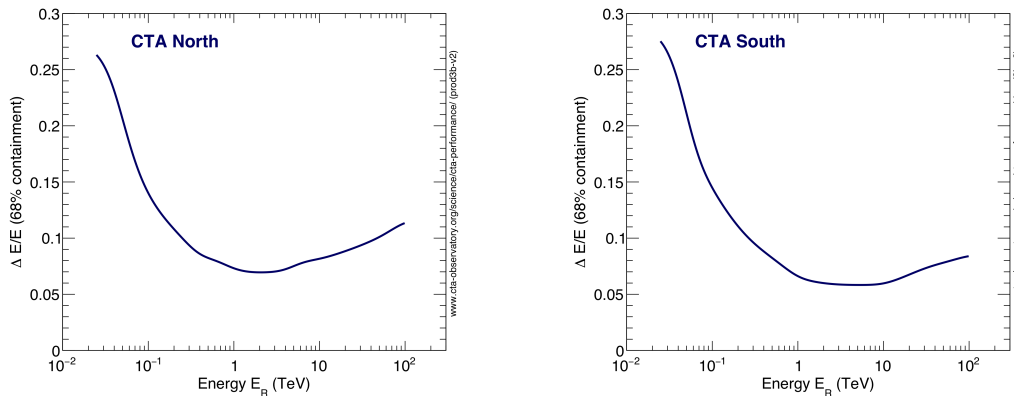
(c) Energy resolution vs reconstructed energy.

(d) Effective collection area for different observing times.
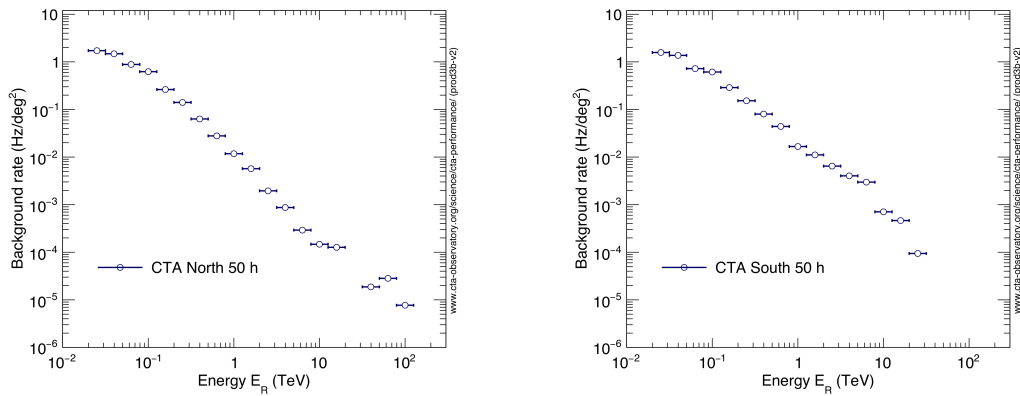
(e) Post-analysis residual cosmic-ray background rate for gamma-hadron separation cuts optimised for 50 hours.

Figure 4.9: Results from the *prod3b* for both the North (left column) and South site (right column) [40].

GRBs analysis with the MAGIC telescopes

While working in the Analysis and Simulation Working Group of CTA to derive the best pointing mode for GRB transients, I joined the transient working group of the MAGIC Collaboration to study these phenomena with current IACTs. Indeed, the group task is the analysis of transients, unpredictable astrophysical events exhibiting short-time scale variability.

This chapter is then structured as follows: in Section 5.1 a brief introduction to the MAGIC telescopes is given. The data analysis chain based on the proprietary software MARS is also described. Section 5.2 introduces the GRB phenomenon. In the last Section 5.3 the results of the analysis I performed of some GRBs observed by MAGIC is shown.

5.1 The MAGIC telescopes

The Major Atmospheric Gamma ray Imaging Cerenkov telescopes are located at the Roque de los Muchachos Observatory on the Canary island of La Palma, the same site where the CTA Northern array is being built (Figure 5.1). The first telescope MAGIC I was built after the HEGRA experiment dismantling and is operative since late 2003. The telescope was designed to have the largest reflector (17m diameter) at that time, in order to achieve a lower energy threshold of below $50\,\mathrm{GeV}$ and to close the gap between space and ground-based gamma-ray observations, a primary goal for the MAGIC collaboration. Another goal was to catch transient events, such as Gamma-Ray Bursts, thus the light weight design for a fast repointing. In 2009 a twin telescope, MAGIC II, started to be operative.

5.1.1 Hardware and systems

The telescopes have an alt-azimuth mount, with a parabolic dish of $17\,\mathrm{m}$ diameter, their total weight is about 60 tons. The parabolic shape, as mentioned before, preserves the arrival time of Cherenkov photons allowing to minimize the time

Figure 5.1: The two MAGIC telescopes. Image taken from https://magic.mpp.mpg.de

spread of the Cherenkov light reflected into the camera and reducing the time window to extract the signal and thus a smaller noise integration. This brings to a better signal to noise ratio.

The mirrors had originally a $\sim 85\%$ reflectivity and, depending on their location in the dish, have a slightly different curvature to match the parabolic profile. An Active Mirror Control (AMC) hardware and software allows mirror adjustments as a function of the zenith angle of the observation, to compensate distortions of the telescope structure. The optical Point Spread Function (PSF) of the instrument can be checked by images of bright stars projected on a dedicated lid in the center of the camera.

The cameras of both MAGIC telescopes have 1.5 m diameter and a FoV of $\sim$ 3.5°. Each camera is equipped with 1039 PMTs grouped into clusters of 7 to form a modular unit [34]. The cameras status can be checked and controlled for each telescope through the Camera Control softwares, *CaCo1* and *CaCo2*, which interact with the central control program of the telescope.

Most of the components and subsystems of the telescopes can be operated via this central control software named *SuperArehucas* (SA). The program, written in LabView, provides a graphical user interface for the operators and automatizes most of the complex tasks during observations, see Figure 5.2.

The weather phenomena can heavily affect the performance and accuracy of the telescopes, thus during data taking the atmospheric conditions are monitored with a Light Detection And Ranging (LIDAR) system. This instrument measures the transmission profile of the atmosphere by recording the back-scattered light of a laser shooting in the direction of the observation [99]. A Pyrometer that measures the intensity of infrared radiation in the FoV of the telescopes is also used. It gives an indication of the cloudiness of the sky. Additional information like temperature, humidity and wind speed are collected by other small instruments. All weather informations are gathered in the weather station monitor that provides feedback during the data taking.

The MAGIC telescopes can operate both in "mono" (only one telescope operates) or in stereo mode. The event recording is regulated by a standard trigger system: a digital coincidence trigger logic, where each pixel in a N next-neighbor group
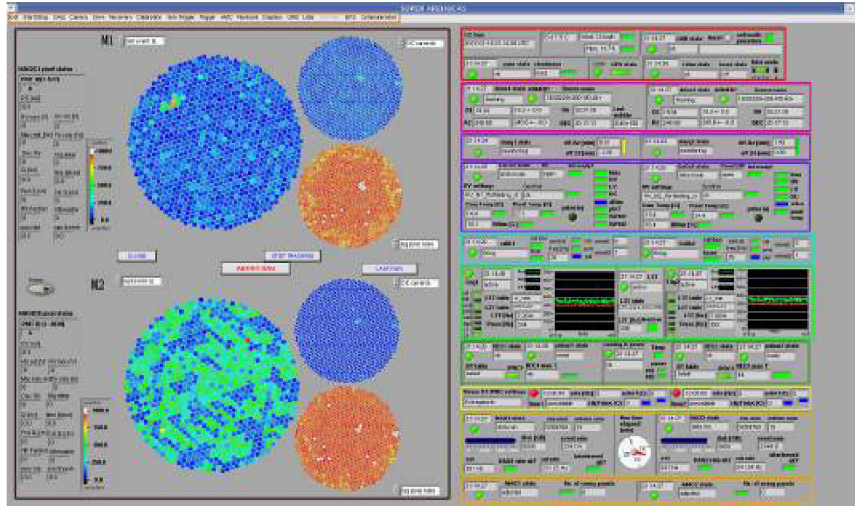
Figure 5.2: *SuperArehucas* graphical user interface. On the left is well visible the information regarding the camera, while on the right side all other subsystem details are reported. Figure from [98]

has to pass a certain signal threshold simultaneously [100] [101]. In stereo mode also the coincidence of both telescopes is required. The trigger system has multiple levels with defined conditions that have to be fulfilled by the event in order to be registered:

1. *L0 trigger*, first level where an individual threshold to each pixel is applied;

2. *L1 trigger*, next-neighbors to the selected pixels are defined. The number of neighbors N can change, generally 2, 3 or 4 are the most common choice;

3. *L3 trigger*, called also stereo trigger, where, in case of stereo observations, a coincidence windows for the time difference between the light flashes hitting both telescopes has to be taken into account.

A second analog trigger is also available, called *Sum Trigger-II* [102], which allows to trigger fainter events.

In case of a triggered event, the readout system sends the sampled signals to the Data Acquisition system (DAQ) [103]. The events are then saved in binary files and stored on disk.

5.1.2 Data taking

As mentioned, the night conditions during observations can influence the data taking and so the final performance of the telescopes. Several safety limits for operations regarding the weather and the hardware are implemented. Outside these limits the telescopes can not operate, in order to avoid damages to the telescopes components. The main ones are:

- Humidity has to be less than 90%;

- wind gusts < 40 km/h and mean wind speed < 50 km/h;

- no rain;

- average PMT current $< 30\mu A$ and individual PMT current $< 47\mu A$;

- mean humidity inside camera < 60%;

- Zenith angle > 1.5°.

MAGIC can also observe in moon conditions, stopping operations only on full moon nights. Particular filters and settings are used in this case to preserve the hardware components. In a year, MAGIC duty cycle is $\sim$ 18%, if no lost time due to bad weather or technical time is considered. Moon observations allow to expand the duty cycle up to 40%, even if with a higher energy threshold due to the increased NSB.

Generally the MAGIC telescopes observe in the so-called *wobble mode* [104]. In this mode the observed source is not pointed directly, but two to four opposite positions with a certain offset from the source are tracked alternately for 20 minutes or less each (Figure 5.3). The advantage is that the "OFF observations", used to evaluate the background, are taken simultaneously with the "ON data". It saves observation time and ensures that OFF data are taken under the same conditions as the ON one. For point-like sources an offset of 0.4° is used, but it can change based on the nature of the source.

A second observation mode is the "*ON mode*". In this case the telescopes point directly to the source, whose position lies right in the camera center. However, additional OFF observations have to be performed under similar Azimuth and Zenith conditions. Usually this modality is used to take OFF data that will be useful for the following data analysis.
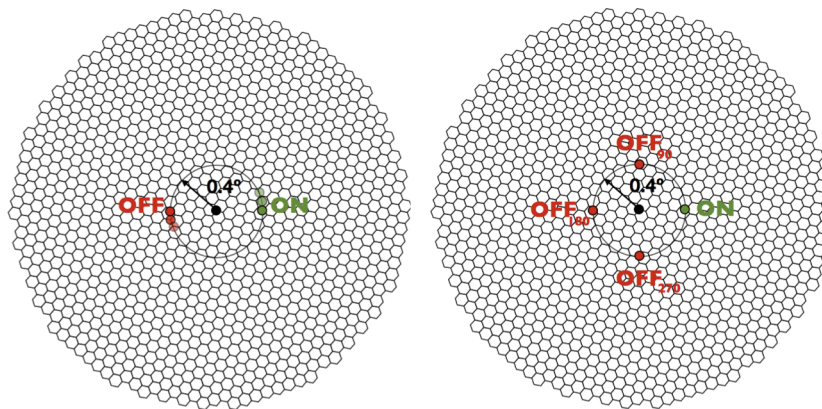
Figure 5.3: Wobble observation pattern in the case of 1 OFF region (left) and 3 OFF regions (right). The black circle represents the center of the camera. Image from [27].

5.1.3 Data analysis chain

Data taken by the MAGIC telescopes are analyzed with the Magic Analysis and Reconstruction Software (MARS) [77], written in `C++` on top of `ROOT`. MARS is a full chain providing all procedures and methods needed to complete a whole analysis, from the reading of raw data to the high level analysis products.

To start an analysis the input data generally needed are: observed data, data collected during the observation in which the gamma-ray signal is thought to be present; OFF data, no signal is present here and they will be used to estimate the background; MC data, for the estimation of the instrument response.

The shower simulations are done with a customized version of the software `CORSIKA`, already described in the previous Chapter, while the telescope response is simulated with two software packages called *reflector* and *camera*. The MC files are updated in case of changes in the hardware configuration or performance of the telescopes, like for example loss of mirror reflectivity due to dust.

The analysis chain, summarized in Figure 5.4, can be divided in several executables:

1. `merp`, converts the data into `ROOT` format,

2. `sorcerer`, performs the calibration,

3. `star`, for the image cleaning and parametrization,

4. `superstar`, for the calculation of the stereo parameters,

5. `coach`, for energy reconstruction and gamma-hadron separation training,

6. `melibea`, for the gamma-hadron separation and the estimation of the event energy and stereo direction,

7. `odie`, `flute`, `caspar`, generate final products like detection plots, energy spectra and skymaps respectively.

All the programs configurations and settings needed for the analysis are passed through input cards, that can be modified according to the science case requirements. I will not enter in the detail of the analysis done by each program, that can be furthered in [77]. However, the concept and many of the techniques used are similar to the ones in the data analysis for CTA described in the previous Chapter.

In standard conditions, the analysis is performed from `superstar` data, that can be retrieved by the MAGIC data center located at the Port d'Informació Científica (PIC) in Barcelona. The previous steps are automatically performed by the OnSite Analysis (OSA) system. However, in the case of analysis in moon or other particular conditions, or if hardware problems happened during the observations, the analyzer can start from a lower level stage. This can happen especially in GRBs analysis.
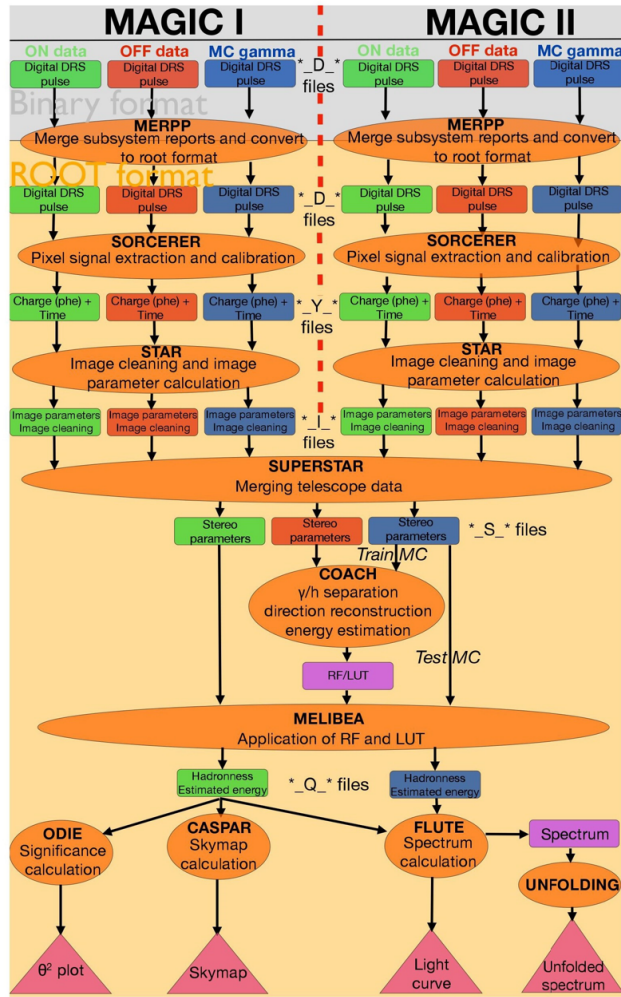
Figure 5.4: Scheme of MAGIC analysis chain. Figure from [27].

In case of a GRB alert, MAGIC has an automatic telescopes repointing procedure during which the DAQ is not stopped. The first subrun of the observation is then classified under the name of the source that was tracked before. This subrun needs to be treated separately, and the analyzers have to start from the calibration data.

5.2 Gamma-Ray Bursts

In the following I will give a general description of the Gamma-Ray Burst (GRB) phenomenon, briefly introduced in Section 1.2.4.

5.2.1 Historical overview

GRBs are the most luminous events in the known universe. They manifest as flashes of hard X and soft γ radiation, lasting from a few milliseconds up to hundreds of seconds. The first GRB was discovered by accident by the Vela satellite mission in 1967 [105], and in the following two decades satellite missions and several theoretical models tried to unfold the nature of GRBs.

A first break through came with the Burst and Transient Source Explorer (BATSE) instrument, launched in 1991 as one of the four main instruments onboard the Compton Gamma-Ray Observatory (CGRO). During its nine years mission, BATSE detected an avarage of one GRB per day, discovering that their distribution is isotropic, i.e., they are evenly distributed in the sky as shown in Figure 5.5 [106]. This provided the first hint for GRBs cosmological origin, disfavoring them as galactic sources.

BATSE Gamma-Ray Bursts
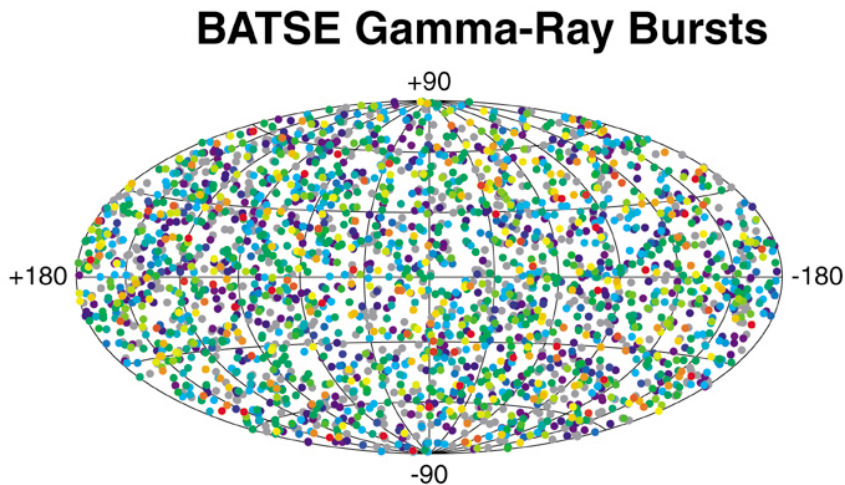
Figure 5.5: The isotropic distribution of the GRBs observed by BATSE during its mission. Image from https://asd.gsfc.nasa.gov/

Until then only the *prompt* phase (gamma-rays emission) of GRBs was known, and no counterparts at any other wavelength could be associated.

Studies on the distribution of the prompt emission duration suggested the separation of the GRBs in two classes (Figure 5.6) [107]: *short* ($T_{90} < 2\,$s) and *long* ($T_{90} > 2\,$s) GRBs, where T_{90} denotes the time interval in which the detector collects from 5% to 95% of the total fluence.

This changed with the second milestone: the discovery by the BeppoSAX satellite, launched in 1996, of the *afterglow* phase, the X-ray counterpart of the GRB. The afterglow of GRB970228 was detected after almost 8 hours by the Narrow Field Instrument BeppoSAX X-ray detectors, improving its positioning accuracy up to $\sim 4\,$arcmin [109]. 21 hours later an optical afterglow of GRB970228 was observed too [110]. Many other afterglow detections followed together with follow-up observations in optical, radio and infrared wavelenghts. These observations led to the localization of the host galaxy and to the measurement of the GRBs redshift, confirming their extragalactic origin. Knowing their distances, the intrinsic power released could be calculated too ($\sim 10^{52} erg\,s^{-1}$).

The interest in GRB's physics grew through the years and several X-ray and gamma-ray instruments were lunched, such as the INTErnational Gamma-Ray Astrophysics Laboratory (INTEGRAL) in 2002, the Neil Gehrels Swift Observatory
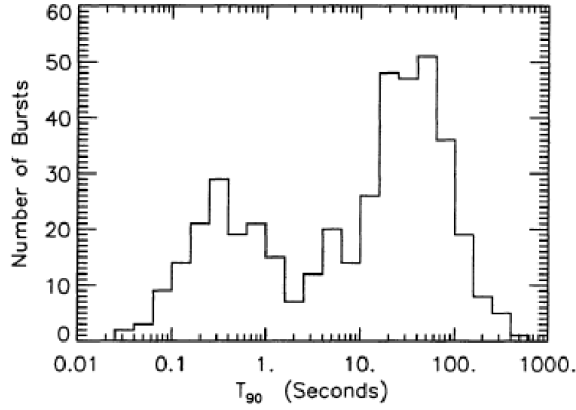
Figure 5.6: T_{90} duration distribution of the GRBs presented in the third catalog of BATSE [108].

(Swift) in 2004, the Astro-Rivelatore Gamma a Immagini Leggero (AGILE) in 2007, and the Fermi Gamma-ray Space Telescope (Fermi) in 2008. For ground-based observatories like MAGIC, H.E.S.S, VERITAS and CTA such instruments are needed to give the trigger for transient events.

5.2.2 Prompt emission

The prompt emission is the first phase of a GRB and its duration is defined by the T_{90} parameter. As said, this parameter separates the GRBs in two populations, short and long, with the short ones showing harder spectra than the long ones. This means that the ratio between high energy and low energy photon counts is larger for short GRBs. GRBs temporal properties are irregular: each light curve is different from one another and no coherent behavior can be found. However the short variability times that can be observed in the light curves suggest that the emission region has to be very compact. This raised the so-called *compactness problem* in 1975, a first argument for the outflows of GRBs to be relativistic [111].

GRBs non-thermal spectrum is usually fitted with the *Band function* [112], two power-law functions smoothly connected at a break energy:

$$N(E) = A \begin{cases} \left(\frac{E}{100keV}\right)^{\alpha} \exp\left(-\frac{E}{E_0}\right) & E < (\alpha - \beta)E_0 \\ \left[\frac{(\alpha - \beta)E_0}{100keV}\right]^{\alpha - \beta} \exp(\beta - \alpha)\left(\frac{E}{100keV}\right)^{\beta} & E \geq (\alpha - \beta)E_0 \end{cases} \tag{5.1}$$

where $N(E)dE$ is the number of photons in the energy bin dE, while the unknown parameters are the low-energy (α) and high-energy (β) spectral slopes, E_0 the break energy and A the normalization factor. The Band function, however, comes from empirical considerations and not all GRBs' spectra can be fitted with it. Several studies during the years have proved that additional components can contribute to the prompt emission spectrum [113]. A smoothly broken power-law

70

function, a cutoff power-law function or a simple power-law function in case of high energy data can be added to better fit the spectra.

The energy power spectrum (νF_ν, where F_ν is the flux density spectrum) is usually represented as $E^2 N(E)$. The typical spectral energy distribution (SED) is a peaked function with $E_{peak} = (2 + \alpha)E_0$.

The Fireball model

Different models tried to describe the main properties of GRBs emission. Nowadays the commonly accepted is the *Fireball model*, first presented by Paczynski and Goodman in 1986 [114]. The model came from the compactness problem: the typical GRB released energy of the order of $\sim 10^{53}$ erg and its short time variability of ~ 10 ms, imply that the emission region has to be very compact. However, a high density of energetic photons in a small region suggests a high opacity to gamma rays; the majority of the photons should be absorbed by pair production processes. Yet, they are detected and the observed spectrum of GRB is non-thermal, which means the source must be optically thin. This can be explained if photons are emitted by a source moving with relativistic velocities towards the observer. With a relativistic expansion the energy of the photons at the source is lower, reducing the number of available photon-pairs that can pair-produce. In this case a lower limit on the required Lorentz factor for an optically thin fireball can be found and is set at $\Gamma > 10^{13/(4+2\alpha)} \gtrsim 100$, where α is the photon's index of the observed gamma rays. For a more detailed explanation and the calculation required, please refer to [115] and [11].

According to the model, a central engine, a compact object like a black hole or a millisecond magnetar, emits a fireball of electrons, positrons and gamma rays, plus possible baryons. The engine might be produced either by the merging of two compact objects or by the collapse of a massive star. The fireball expands and undergoes an acceleration phase. As it moves outwards, it cools with the internal energy of the photons adiabatically transformed into bulk kinetic energy of the outflow [116]. This is the phase were the prompt emission is produced. However a pure radiation fireball cannot generate the observed non-thermal prompt emission spectra. If a small amount of baryons is present, the fireball's energy will be transferred to the kinetic energy of baryons [117]. The interaction of baryons with the surrounding medium results in relativistic shocks generating high-energy particles and magnetic fields, allowing the energy to be radiated through synchrotron and/or inverse Compton processes producing non-thermal spectra. This is based on the assumption that the dissipation process is done by shocks generated by the outflow. Two types of shocks are possible: *internal* and *external* shock.

The internal shocks are within the moving ejecta, while the external ones occur when the ejecta is decelerated interacting with the interstellar medium (ISM). The internal shock model easily accounts for the high temporal variability of the prompt

emission and its non-thermal spectrum. The external shock, instead, explains the multi-wavelenght afterglow radiation.

This scenario allows to explain most of the properties observed in the prompt and afterglow emission. Moreover it is independent from the nature of the central engine originating the fireball.

5.2.3 Afterglow

As mentioned above internal shocks convert part of the kinetic energy of the fireball into radiation producing the prompt gamma-ray emission. After, the fireball starts to decelerate and the generated external shocks propagate into two directions: into the external medium (forward shock) and into the outflow itself (reverse shock) [117]. The reverse shock generates the prompt optical emission, while the forward shocks weeps up and accelerates the ISM producing the afterglow emission. The afterglow is observed up to days/months after the prompt emission as a long fading multi-wavelength emission in the X-ray, optical and radio bands. From the optical information of the afterglow the redshift can be determined and so the burst distance. The radiative mechanism responsible for the afterglow emission is assumed to be the synchrotron emission.

5.2.4 Progenitors

Studying the GRBs observational features and their host galaxies, hypothesis on the nature of GRB progenitors can be done. A hint about the different nature of the progenitors for short and long bursts came from the duration distribution of the GRB prompt emission. The existence of two populations of GRBs was suggested by the bimodal distribution of their T_{90} (Figure 5.6).

The fast variability seen in GRB light curves suggests that the progenitors are compact objects. Moreover the central engine should be able to release a great amount of energy and generates a collimated outflow accelerating it to relativistic velocities. Different models were developed to explain the different types of GRBs, the main two categories being massive stars and binary systems of compact objects.

The connection between long GRBs and the death of massive stars came empirically from observations that linked GRBs to supernova Ic type [118] [119]. Supernovae Ic are believed to be produced by the collapse of Wolf-Rayet stars which lose their hydrogen and helium envelopes prior to the explosion. Moreover resolved host galaxies of long GRBs are typically star forming galaxies.

Most of the short GRBs have instead host galaxies with little star formation, or their position is at edges of the hosts [120]. These observations suggest that the short GRBs progenitor is related to the merger of compact objects, such as a system composed of a neutron star and a black hole (NS-BH) or a neutron star binary (NS-NS). This was confirmed by the detection of the gravitational wave event GW170817,

possibly associated to the merger of two NS, and the independent detection in the same sky region of the short GRB170817A [16] (see Figure 5.7).
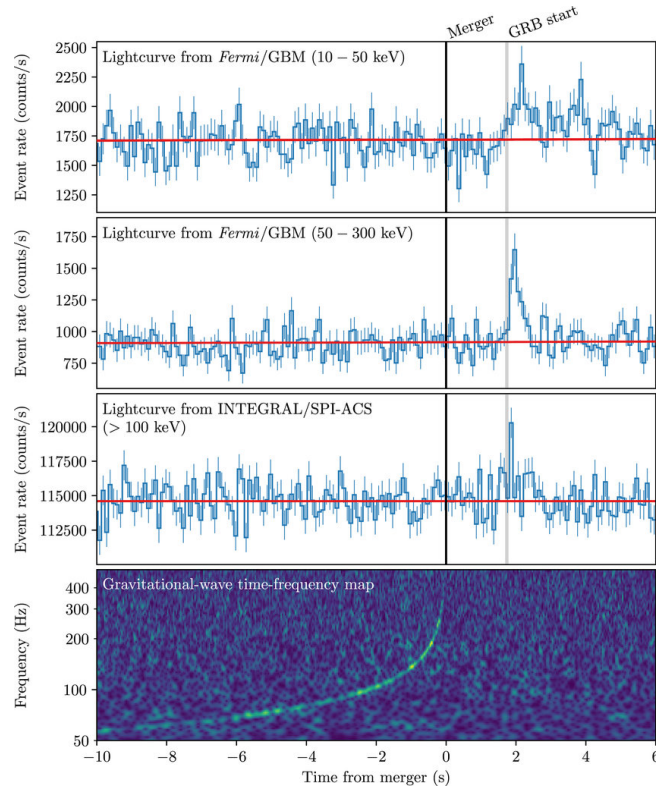
Figure 5.7: Multi-messenger detection of GW170817 and GRB170817A. In the top 3 panels the light curves of the GRB seen from Fermi/GBM and INTEGRAL. In the bottom panel the time-frequency map of GW170817 [16].

5.2.5 HE and VHE emission

High-energy emission from GRB has been firstly detected in a few cases with the EGRET instrument. Before, the highest energy of the detected photons was less than 100 MeV. Indeed usually GRBs emission is detected in the keV-MeV energy band. A significant event was GRB940217, which triggered both BATSE and EGRET. This GRB showed a high energy emission significantly long (~ 5400 s), during which 28 gamma rays were observed, with a 18 GeV photon detected by EGRET ~ 4500 s after the trigger. As can be seen in Figure 5.8, 18 photons were detected when the low-energy emission was already over. This event was an important hint to the long and delayed GeV emission with respect to the low-energy one and set also the ground for the possible presence of additional spectral components to explain the HE emission. A second burst, always detected by BATSE and EGRET, that showed clearly that the high-energy component had different features with respect to the low-energy one, was GRB941017 [121]. The Band model is not sufficient to describe the low and high-energy spectra together anymore. An additional component or a cutoff are needed.
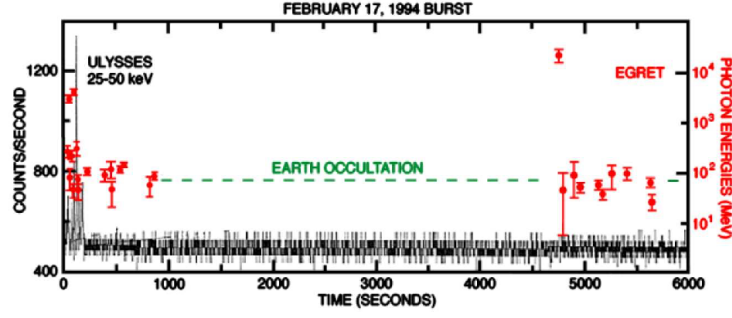
Figure 5.8: Plot showing the photons detected by EGRET in red, together with the count rate of Ulysses X-ray counter in the range 25-150 keV in black. The horizontal green line is the time when EGRET was occulted by the Earth [122].

The launch of more advanced satellites like Fermi with the Large Area Telescope (LAT) and Gamma-ray Burst Monitor (GBM) on board, opened new possibilities in the study of HE GRB emission. Two LAT catalogs [123] [124] were released covering more than 10 years of data taking. The GRBs analysis confirmed that the high-energy emission recorded by LAT above > 100 MeV starts significantly later with respect to the low emission observed with GBM and lasts longer.

These observations led to the suggestion that the external forward shock is responsible for the high-energy emission via synchrotron process during the early afterglow. The forward shock high-energy emission explains the luminosity observed during the late afterglow phase [125] [126].

Until 2019, no detection of GRBs at VHE from a IACT was performed. On January 2019 the MAGIC telescopes, triggered by an alert from Swift-BAT, reported a significance > 20σ for GRB190114C in 20 minutes of observation and at an energy greater that 300 GeV [127]. Always in 2019, the H.E.S.S. collaboration announced other two detections: GRB180720B detected with a significance of 5σ and GRB190829A with a > 5σ confidence level. Both observations started long after the trigger, 10 hours for GRB180720B [128] and 4 hours for GRB190829A [129].

5.3 GRBs analysis

As member of the transient working group of MAGIC, I performed several GRB analyses. In the following the results for GRB140430A, GRB190106B, GRB191004A and GRB200125B are shown. The only one with redshift measurement is GRB140430A. Its redshift could be determined to be 1.6 thanks to the Very Large Telescope (VLT) observations. No VHE signal was detected from any of the these GRBs. For each GRB the following plots are shown:

- θ^2 plot obtained from `odie`. The blue points are the ON data while the OFF ones correspond to the grey filled histogram. A label is also shown in the plot with the information on the observation time, the total ON, OFF and excess

74

events and the value of the significance calculated according to the Li&Ma formula [97].

- test statistic (TS) skymap obtained from `caspar` specifying the coordinates of the GRB.

- TS value distribution plot, showing the data compatible with background emission in a red line (null hypothesis distribution) and the distribution from the taken data in white circles as markers.

- significance plot, divided in 4 subplots showing the evolution in time of the significance, the excess events number, the background events number and the signal to noise ratio.

The plots are obtained applying to the ON data low energy cuts on several parameters, especially on size and hadronness, for signal search. Currently three sets of standard cuts are used in three energy ranges: Low Energy (LE), High Energy (HE) and Full Range (FR). The LE cuts are the looser ones. Applying different cuts results in a slightly different final sensitivity.

For comparison the θ^2 plot and the skymap for an observation of the Crab nebula are also shown where the red points are the ON data (Figure 5.9).

(a)

(b)
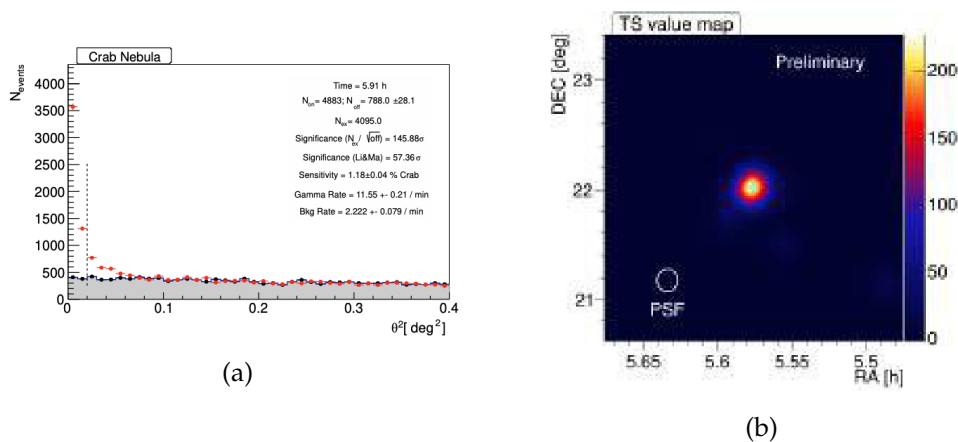
Figure 5.9: a) Example of a θ^2 plot and b) a skymap for Crab nebula data.

(a) θ^2 plot.

(b) Significance evolution in time.

(c) TS skymap and distributions.
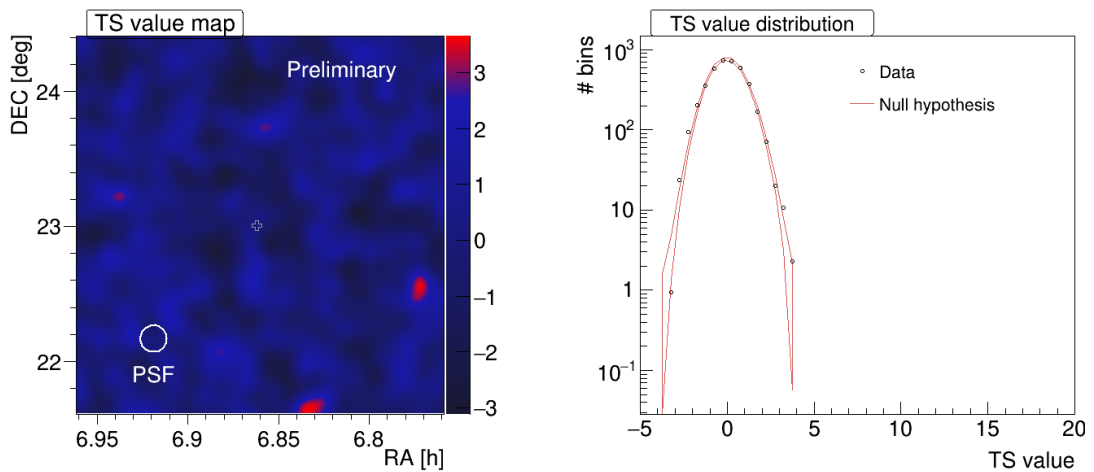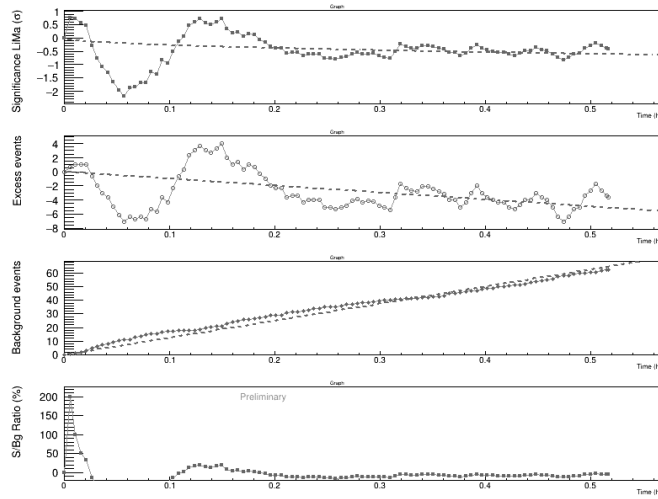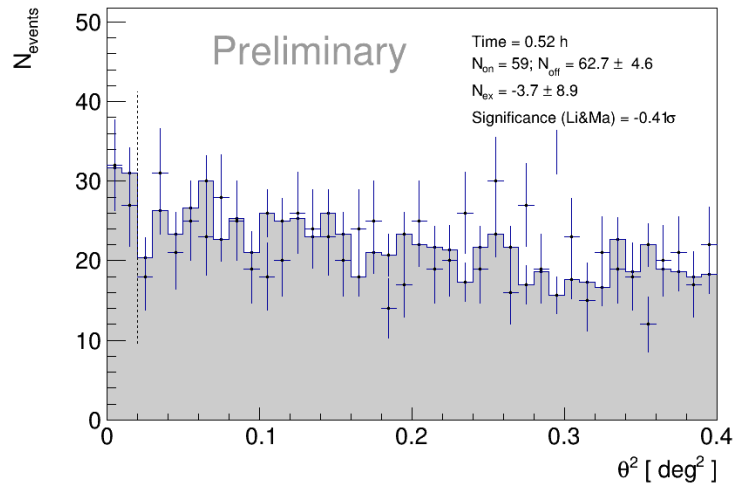
Figure 5.10: θ^2 plot, significance evolution in time and TS skymap and distribution for GRB140430A. GRB140430A was triggered by Swift-BAT at 20:33:36 UT.

(a) θ^2 plot.
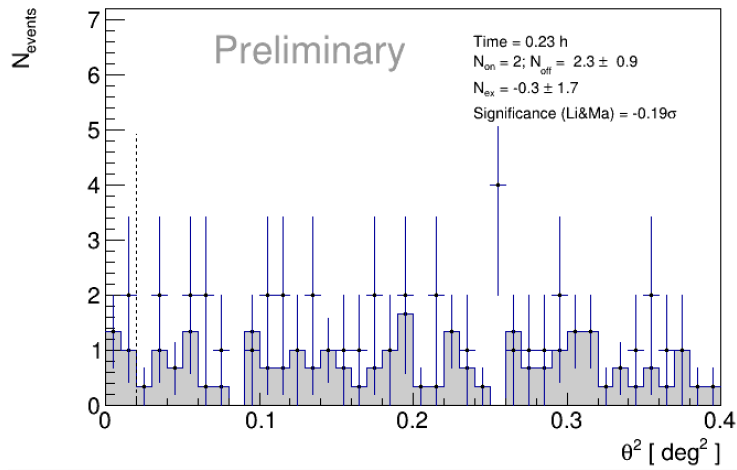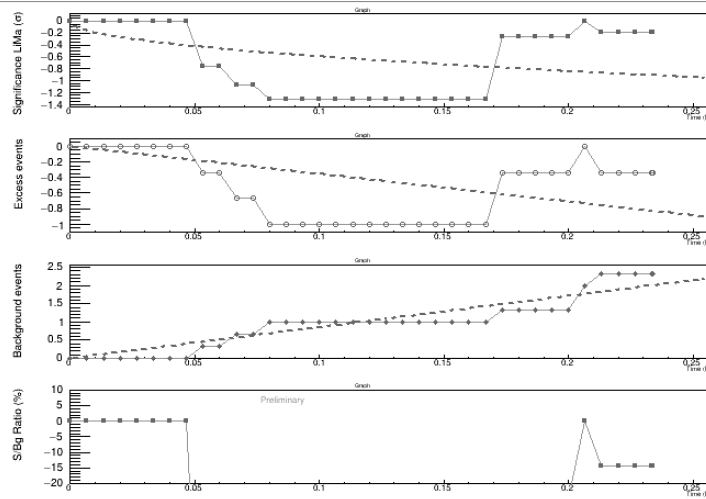
(b) Significance evolution in time.
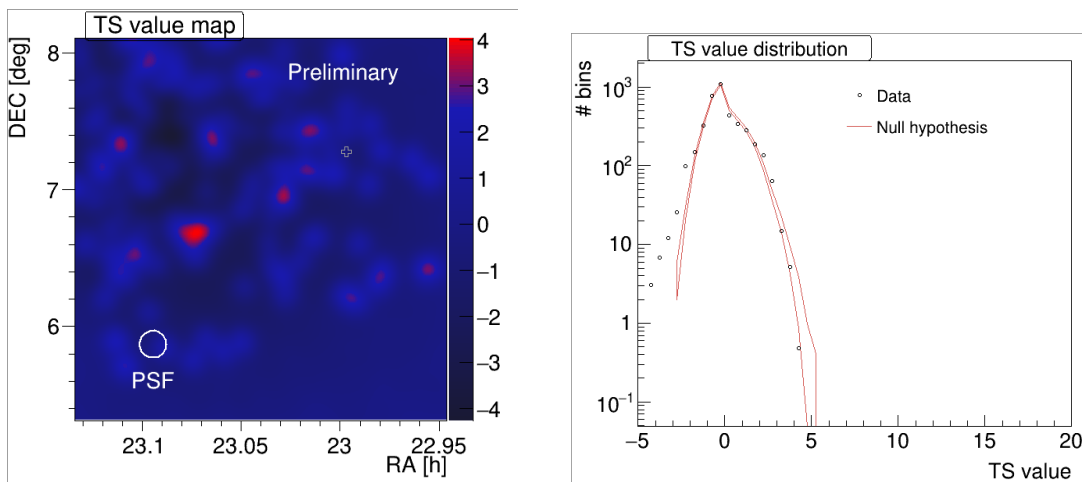
(c) TS skymap and distributions.

Figure 5.11: θ^2 plot, significance evolution in time and TS skymap for GRB190106B. GRB190106B was triggered by Fermi-GBM at 20:47:10.476 UT.

(a) θ^2 plot.
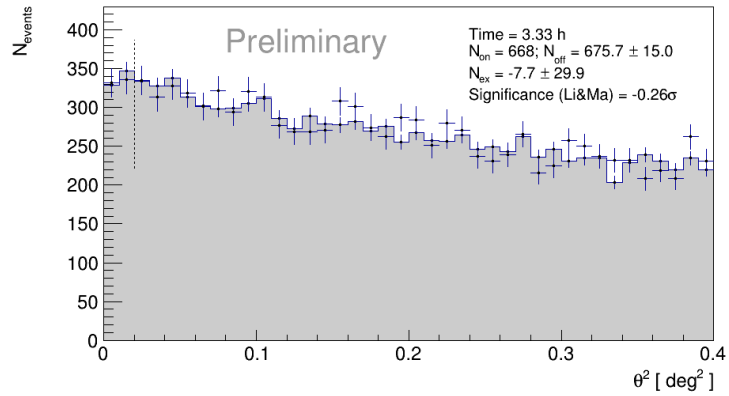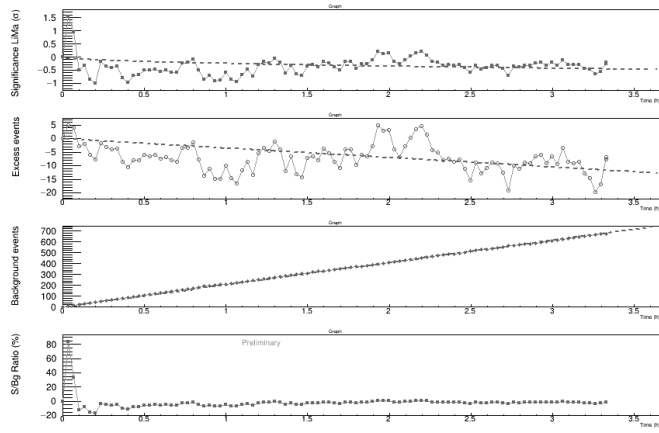
(b) Significance evolution in time.
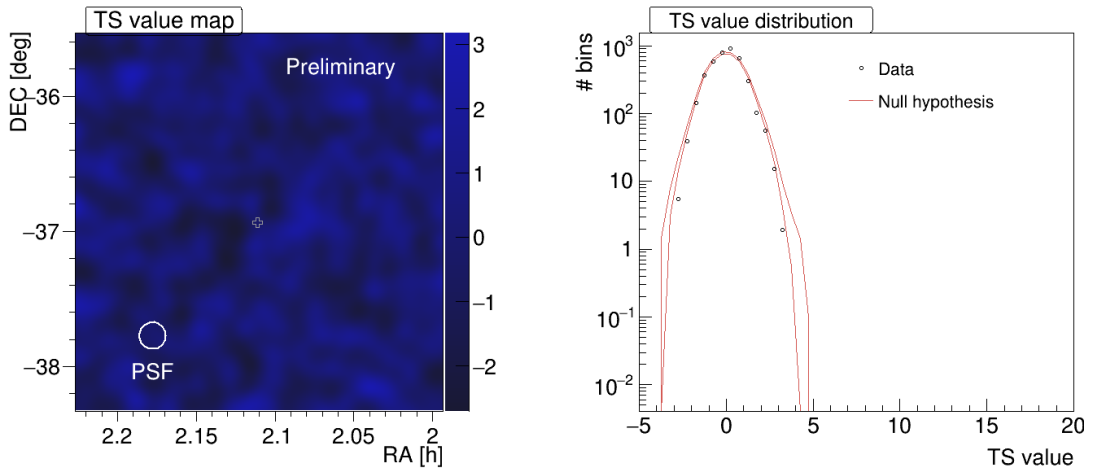
(c) TS skymap and distributions.

Figure 5.12: θ^2 plot, significance evolution in time and TS skymap and distribution for GRB191004A. GRB191004A was triggered by Swift-BAT at 18:07:02 UT.

(a) θ^2 plot.
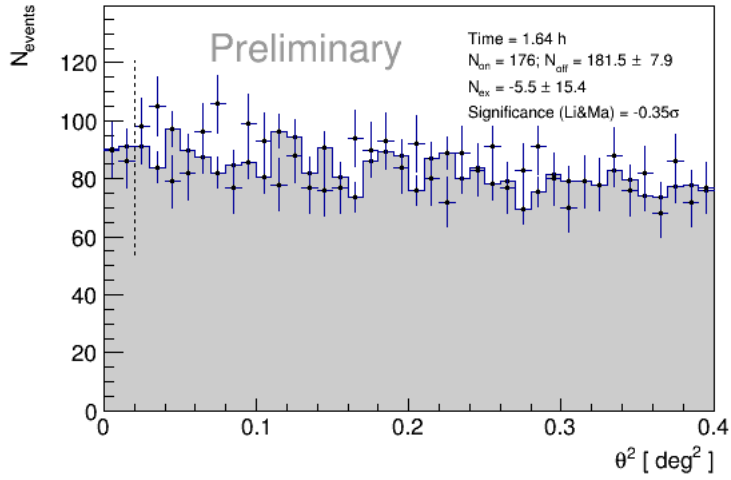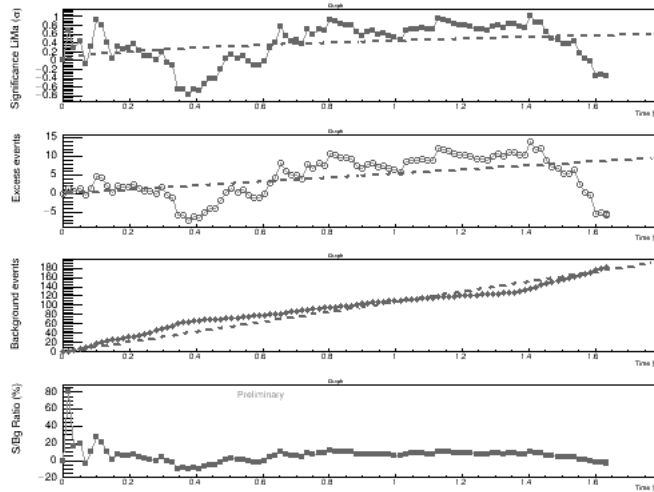
(b) Significance evolution in time.
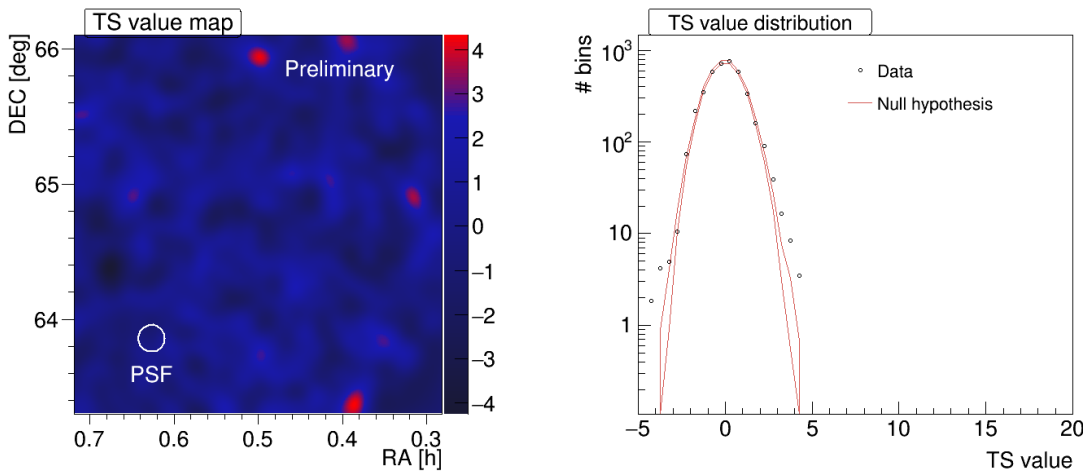
(c) TS skymap and distributions.

Figure 5.13: θ^2 plot, significance evolution in time and TS skymap and distribution for GRB200125B. GRB200125B was triggered by Fermi-GBM at 20:43:31 UT.

Divergent Mode Sensitivity

In order to optimize a new pointing mode, simulations and analysis must be done to prove the benefits. The work to investigate the CTA northern site performance in the case of divergent observing mode is presented in this Chapter. The values and parameters required to perform such Monte Carlo simulations and analysis, together with the programs used, will be illustrated. Part of the work illustrated here was already published in [130].

6.1 Introduction

As introduced in Section 3.2, the divergent pointing has been considered by the CTAO for tasks as survey or GW follow-up as an alternative observation mode to the nominal one, referred to as "parallel mode", where all telescopes point to the same position in the sky. Due to the large number of telescopes with respect to the existing experiments, CTA will be the first IACT array able to use the divergent mode.

The performance of an array of telescopes operating in sky-survey mode depends upon the field of view of the system and the time of observation needed to achieve a given signal significance level, i.e. its sensitivity. In the standard pointing scheme, sky surveys are performed with telescopes pointed into the same direction of the sky. However, in such a case the FoV of the system is highly limited by the FoVs of the individual telescopes.

The overall FoV of a telescope array can be significantly enlarged by slightly deviating the pointing direction of each telescope according to its position in the array. This is the idea on which the divergent mode is based: telescopes are inclined into the outward direction by an angle increasing with the telescope distance from the array center (see Figure 6.1).

The performances of the array can vary a lot according to the pointing pattern. Thus, the pointing directions should be chosen in order to maximize the size of the field of view while maintaining a certain average telescope multiplicity (number of

telescopes looking at the same part of the sky), crucial parameter for the quality of the shower reconstruction.

The chosen telescope pointings will affect the angular resolution, the energy resolution and the sensitivity, that have to be studied in order to decide on the optimal divergent mode configuration. The requirements that have to be fulfilled are driven by the science case.

Other patterns with a mix of parallel and divergent pointing may be considered: groups of telescopes, such as pair or triplets, having the same pointing directions but divergent within one another. They have not been investigated in this thesis, but are possible and should be considered in future works.

Figure 6.1: a) Standard pointing, b) divergent pointing. Adapted from [131].

Two preliminary studies of this pointing mode based on the first CTA Monte Carlo productions using only SSTs and MSTs have been presented in the past (see [64] and [131]).

In [64] an array of 18 MSTs and 56 SSTs was studied and the considered pattern lead to a FoV of $14°$. The work showed that, compared to a normal pointing of the same array, a gain of 1.5 in sensitivity and a factor 2.3 in time, could be achieved in survey mode. In the second work, the authors have shown that the divergent mode could be more convenient with respect to the normal pointing mode for source detection, reaching a better flux sensitivity. The study was carried on with an array of 23 MSTs and it was shown that the time needed to perform a scan on a fixed sky area of $20°$ x $12°$ at a given sensitivity is smaller by a factor of ~ 2 with respect to the parallel mode. Even though the angular and energy resolutions are up to a factor of about two worse when compared to the normal pointing, an increase in flux sensitivity is important for the survey science project, especially for the extragalactic one.

These works were carried out using the *prod1* simulation (see Chapter 3), in which the number of telescopes, their characteristics and the construction site were still undefined. Thus this PhD work intended to continue and update the results of those works, taking advantage of the improved MC models and implementing the non standard analysis into the official reconstruction pipeline. The basis set from this work will allow to perform further and deeper analyses of the simulated data for the divergent pointing.

The analysis were performed with the use of the programs described in Chapter 4.

6.2 Simulations

When undertaking simulations on the scale required for CTA, a very large number of showers needs to be simulated in order to have adequate statistics at the detection and post-analysis stages. At the start of this thesis, the work was more focused in finding the best pointing configuration and adapting the pipeline for the analysis, thus, due to time and processing convenience, the performed simulations were smaller in size if compared to the big production, as *prod3*. For the analysis shown later, I only used data simulated on the full northern array for both the parallel and the different divergent configurations since I am most involved in the LST Collaboration and interested in the extragalactic sky.

Gamma rays were simulated from a point-like test source with the direction defined by Zenith angle = 20° and Azimuth angle = 180° measured with respect to the magnetic North. Protons and electrons were simulated as diffused. All the settings of the `CORSIKA` simulations are the same as the ones reported in Table 4.1 used for the *prod3* production, except for the number of showers `NSHOW`. Table 6.1 summarizes the simulated dataset for each of the pointing configurations (pointing patterns in Appendix A).

All the simulations, after some tests at the INFN computing facility in Trieste, were performed using the GRID.

	gamma	proton	electron
Energy range	3 GeV - 330 TeV	4 GeV - 600 TeV	4 GeV - 600 TeV
# shower	10^4	$2 \cdot 10^4$	$2 \cdot 10^4$
# re-use	10	20	20
# files	1000	1000	500
# tot particles	10^9	$4 \cdot 10^9$	$2 \cdot 10^9$

TABLE 6.1: For each of the different pointing configurations, the number of files per particle that were simulated are reported. Each file has a number # of shower and each of them is re-used # times.

Regarding `sim_telarray` (see Par. 4.2.2), all the configurations and parameters were kept the same as in the parallel simulation. The only change was in the configuration file used as input, where the pointing directions of each telescope were added. This can be done specifying the `telescope_theta` and `telescope_phi` parameters (block code 6.1), which represents the Zenith and Azimuth angle respectively.

```
#ifndef TELESCOPE
# define TELESCOPE 0
#endif
#if TELESCOPE == 0
    telescope_phi = ...     % array azimuth
    telescope_theta = ...   % array zenith angle

#elif TELESCOPE == 1
% Take constant global config values from one of the telescope config files
#    include <CTA-ULTRA6-LST.cfg>
    telescope_phi = ...     % telescope 1 azimuth
    telescope_theta = ...   % telescope 1 zenith angle
```

```
#elif TELESCOPE == 5
#    include <CTA-ULTRA6-MST-NectarCam.cfg>
    telescope_phi = ...      % telescope 5 azimuth
    telescope_theta = ...    % telescope 5 zenith angle

... (each telescope separately) ...
#endif
```

LISTING 6.1: Extrapolation of part of the input card where the pointing of each telescope is specified together with its camera configuration file.

For a divergent simulation those two values have to be individually set through the configuration file.

A key passage was defining the direction of the telescope identified by the ID = 0. This actually denotes the general array pointing (code 6.1). In case of parallel on-axis studies, it matches with the source position that has been simulated, instead for divergent analysis the single telescope pointings diverge from it.

The array pointing is set as a global parameter thanks to these two lines in the `sim_config.c` file:

```
array->azimuth = default_setup.telescope_phi;
array->altitude = 90. - default_setup.telescope_theta;
```

In parallel mode the direction is set for all the telescopes through the command line and thus the array pointing will have the same value, but that is not true anymore for the divergent case. So the definition of the "fake" telescope with ID = 0 is essential, otherwise the array pointing will be defined by the coordinates Az = 0° and Alt = 90° as default. This would arise problems in the later analysis of the data, when the `offset` parameter, that establishes the separation between the reconstructed direction and the simulated one, is calculated: its value would be too big and no data would pass the quality cut imposed.

The rest of the telescope configurations are position-independent, all the directions are self generated to achieve the desired divergent viewing pattern.

6.2.1   Pointing tool

The choice of the pointing pattern is a crucial step. At the beginning of the work, presented in [130], the pointings were chosen with a simple script, where only an "*offset*" parameter was used, in order to have some test configurations to start with and investigate the event reconstruction in divergent mode.

Later, with the help of Thomas Vuillaume of the Laboratoire d'Annecy de Physique des Particules, I started working on a new pointing tool. The idea was that, once defined the value of the "divergence" parameter, from the ground position of the telescopes the script calculates the pointing directions and other informations, such as the telescope multiplicity and the geometrical hyper field of view (HFoV). The HFoV represents the total area covered by all the telescopes FoV.

The tool, written in python, is divided in 3 modules: `telescope.py`, `pointing.py` and `visualization.py`.

`telescope.py` contains the classes `Array` and `Telescope`, where all the telescopes and the array properties are defined. For example, a telescope is defined by its ground position, focal length and camera radius, then other properties such as the field of view and the pointing, if an object is specified, can be established (see snippet code 6.2).

```python
class Telescope:

    _id = 0
    def __init__(self, x, y, z, focal, camera_radius):

        self.x = x.to(u.m)
        self.y = y.to(u.m)
        self.z = z.to(u.m)
        self.focal = focal.to(u.m)
        self.camera_radius = camera_radius.to(u.m)
        self.alt = u.Quantity(0, u.rad)
        self.az = u.Quantity(0, u.rad)
        Telescope._id += 1
        self.id = Telescope._id

    def point_to_altaz(self, alt, az):
        self.alt = alt.to(u.rad)
        self.az = az.to(u.rad)

    @property
    def position(self):
        return np.array([self.x.to(u.m).value, self.y.to(u.m).value, self.z.to(u.m).value]*u.m)

    def point_to_object(self, object):
        """
        object: numpy.array([x, y, z])
        """
        GT = np.sqrt(((self.position - object) ** 2).sum())
        alt_tel = np.arcsin((-self.z.value + object[2]) / GT)
        az_tel = np.arctan2((- self.y.value + object[1]), (- self.x.value + object[0]))
        self.point_to_altaz(alt_tel * u.rad, az_tel * u.rad)
```

LISTING 6.2: Some of the functions defined inside the `Telescope` class.

The same for the class `Array`, where all the positions and pointings of the telescopes are taken into account and the information of the array's *barycenter* is also added (code snippet 6.3). Moreover, here is defined the function `divergent_pointing`, that updates the pointing of the telescopes with a given parameter `div` (divergence), as shown in the block code 6.6. Two simple functions to display the array in 2D and 3D are also implemented. In 2D different projections can be chosen.

```python
class Array:

    def __init__(self, telescope_list):
        self.telescopes = telescope_list
    @property
    def positions_array(self):
        return np.array([tel.position for tel in self.telescopes])
    @property
    def pointing_vectors(self):
        return np.array([tel.pointing_vector for tel in self.telescopes])
    @property
    def barycenter(self):
        return self.positions_array.mean(axis=0)
```

LISTING 6.3: Main functions of the `Array` class.

Inside the module `pointing.py`, instead, the functions to define the telescopes pointings can be found. The same reference frame as `simtel_array` has been adopted in the code:

- X is pointing North

- Y is pointing West

- Z is pointing upward

- Az is taken clock-wise from X (towards Y) and between -180 and 180 degrees

- Alt is taken from ground (towards Z) between -90 and 90 degrees

To implement the "umbrella mode", where the divergence angle increases with the distance from the array center, we defined a parameter called `div`. With the set of only this parameter the pointing pattern of the array can be defined.

(a) `div` $= 0$

(b) `div` $= 0.5$

(c) `div` $= 1$
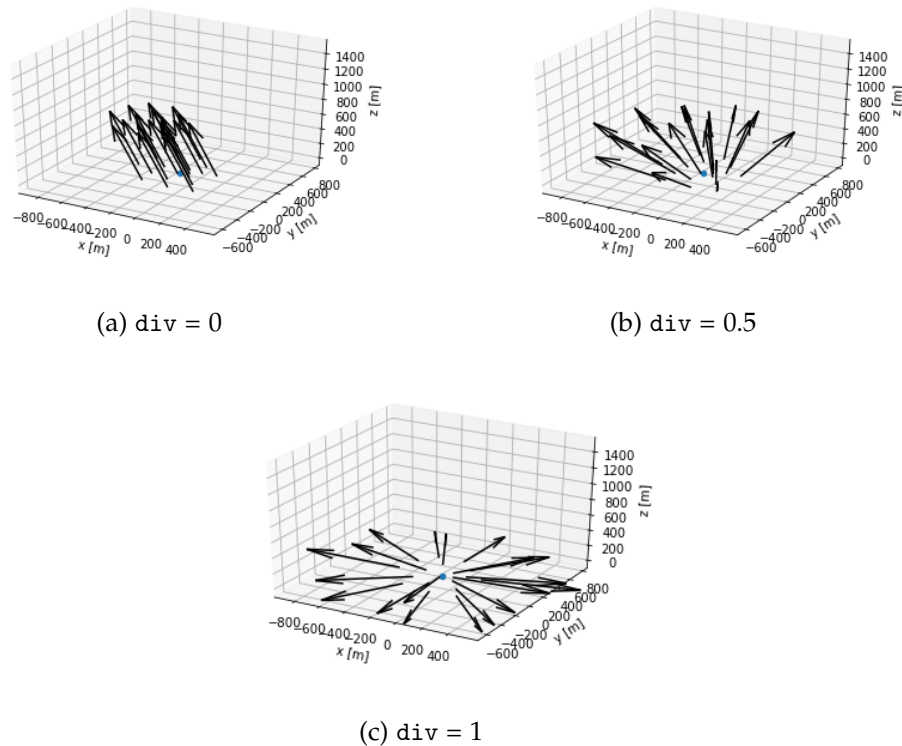
Figure 6.2: Example of the array pointing for three different values of the parameter `div` in case of a source at (Alt,Az) = $(70°,180°)$. The plots are the output of the function `display_3d` defined inside the class `Array`.

The parameter `div` can go from zero to one, where the value zero corresponds to the parallel pointing, while the value one means maximal divergence. Figure 6.2 clarifies the situation.

Consider for simplicity the barycenter B of the array at coordinates (0,0,0) of the defined system and a telescope T at a distance of $1\,\mathrm{m}$ from it (see Figure 6.3). We

define a point G on the z axis such that the line passing through G and T forms an angle α with the parallel direction P.
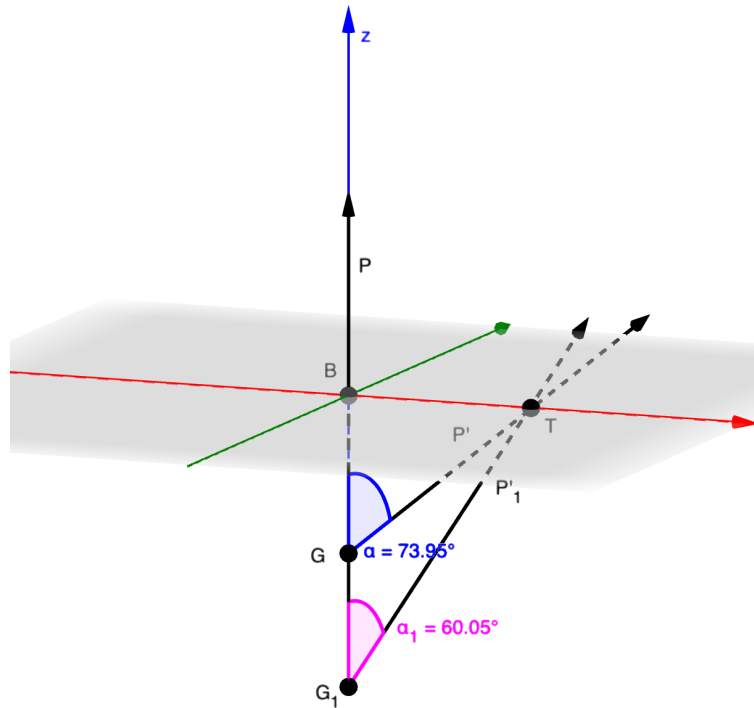
Figure 6.3: Concept used to define the divergent pointing from a parallel one for a telescope.

The divergence of the telescope pointing P' can be controlled through the angle α. This implies that an α value should be defined for each telescope. To avoid this and control the divergence with a single parameter for the whole array, we defined $div = \sin(\alpha)$. Therefore, the distance between G and the barycenter B is given by:

$$|\overrightarrow{GB}| = \frac{1}{\tan(\arcsin(div))} \tag{6.1}$$

In this way the parallel pointing corresponds to $div = 0$ ($\alpha = 90°$), the maximum divergence to $div = 1$ ($\alpha = 0°$).

So once defined the value of the `div` parameter and computed the pointing vector P', the G position can be computed (code snippet 6.4).

```
def pointG_position(barycenter, div, alt_mean, az_mean):
    norm = _norm_div(div)
    Gx = barycenter[0] - norm * np.cos(alt_mean) * np.cos(az_mean)
    Gy = barycenter[1] + norm * np.cos(alt_mean) * np.sin(az_mean)
    Gz = barycenter[2] - norm * np.sin(alt_mean)
    return np.array([Gx, Gy, Gz])
```

LISTING 6.4: Evaluation of the position of G for the pointing as implemented in the code. The function takes as input the coordinates of the barycenter, the `div` value and the mean pointing altitude and azimuth in radians from which to diverge.

A normalization has to be introduced to take into account the different position of the telescopes from the barycenter of the array. To generalize the formula 6.1, it can be written:

$$norm = \frac{f}{\tan(\arcsin(div))} \tag{6.2}$$

where f is the scale factor, defined as the telescope distance from the barycenter at which $div = \dfrac{divergence\ angle}{90°}$.

Now the telescope distance from G can be calculated and thus its divergent pointing directions (code snippet 6.5).

```python
def tel_div_pointing(tel_position, G):
    GT = np.sqrt(((tel_position - G) ** 2).sum())
    alt_tel = np.arcsin((tel_position[2] - G[2]) / GT)
    az_tel = np.arctan2((tel_position[1] - G[1]), (tel_position[0] - G[0]))
    return alt_tel, az_tel
```

LISTING 6.5: Function that computes the divergent pointing to a point G for a telescope updating its previous values. It takes as input the telescope T and also G position.

Finally, all these implementations are brought together by the function `divergent_pointing` defined in the `Array` class: simply passing the `div` parameter and the source position, the pointing of all telescopes of the array is updated with the divergent one.

```python
from . import pointing

def divergent_pointing(self, div, alt_mean, az_mean):
        if div==0:
            for tel in self.telescopes:
                tel.point_to_altaz(alt_mean, az_mean)
        else:
            G = pointing.pointG_position(self.barycenter, div, alt_mean, az_mean)
            for tel in self.telescopes:
                alt_tel, az_tel = pointing.tel_div_pointing(tel.position, G)
                tel.point_to_altaz(alt_tel*u.rad, az_tel*u.rad)
```

LISTING 6.6: Function that computes the divergent pointing of all telescopes of the array given a parameter div.

In the last module `visualization.py` all the functions and methods for the visualization of the computed divergent directions are implemented. At the moment skymaps and FoV multiplicity plots are supported. Moreover informations about the average multiplicity and the area covered by the hyper field of view are printed. These informations were obtained through different methods of the python package `Shapely`, which allows the manipulation and analysis of geometric objects in the Cartesian plane.

I chose to analyze five different configurations, which approximately correspond to x1.5, x2, x3, x4 and x5 times the nominal field of view in parallel pointing. The nominal field of view is defined by the MSTs, having a larger FoV with respect to the LSTs. In Table 6.2 the values for all the five divergent configurations tested are reported. The same values, in the case only the MSTs or the LSTs sub-array

is considered, are also reported. All the plots regarding these configurations are shown in the Appendix A.

	parallel	cfg1.5	cfg2	cfg3	cfg4	cfg5
HFoV (deg^2)	46.5	69.62	93.70	140.3	186.37	233
Overall average multiplicity	16.25	10.85	8.06	5.38	4.05	3.24
MSTs average multiplicity	15	10.02	7.44	4.97	3.74	3
LSTs average multiplicity	4	3.41	2.98	2.41	2.05	1.8
LSTs HFoV (deg^2)	14.5	17	19.47	24.04	28.32	32.38

TABLE 6.2: Comparison of the values for the hyper field of view and telescope's multiplicity between the parallel pointing and the five divergent configurations simulated.

6.3 Analysis

In order to analyze the divergent simulations, the low-level pipeline `ctapipe` had to be adapted. With respect to the parallel simulations, the difference in the analysis of the MC data is mainly at reconstruction level. Once implemented the new features, the later analysis from DL0 to DL3 can be easily performed by the standard chain. The problems encountered during the testing have been solved with minor changes in the code, or with modification in the simulations, like the one regarding the `pointing_array` in `simtel_array` mentioned before.

6.3.1 Divergent reconstruction in `ctapipe`

This part of the work was carried out together with the colleague Thomas Gasparetto [132] of the University of Trieste.

To perform an analysis of divergent events, modifications to the class `HillasReconstructor` in `ctapipe` were required. The changes concern mainly the impact point reconstruction. The reconstruction of the height of the maximum of the shower (h_{max}) and its direction instead, needed only minor corrections. As presented in Section 4.3.1, in the event reconstruction method two points in the camera frame are transformed to two points in the sky frame. Together with the position of the telescope on the ground, the two points define a plane in the 3D space. From the pair-wise intersection between the planes of the considered telescopes the direction can be reconstructed. Since the planes are created for each telescope separately using its pointing direction, it also applies in case of divergent data. The same concept is used for the estimation of the h_{max}.

The reconstruction of the impact point, instead, is done in the *TiltedGroundFrame*, a plane perpendicular to the array pointing direction. Once reconstructed in this frame, the impact point is projected into the *GroundFrame* and the comparison
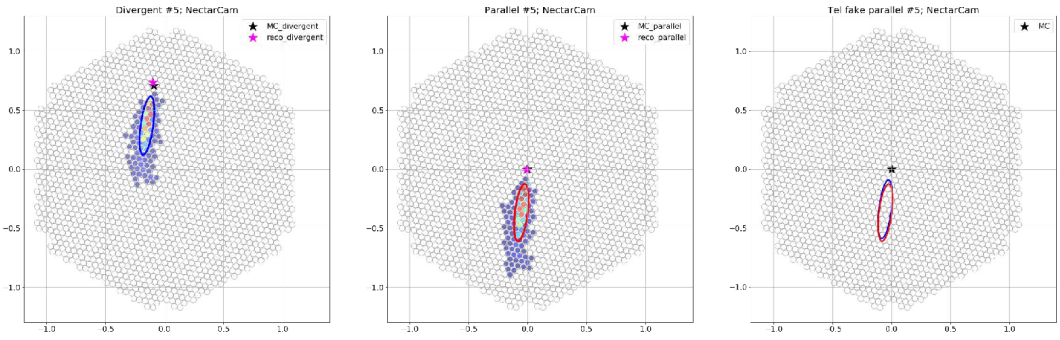
Figure 6.4: Example of the use of the virtual telescope. The first two images show the same event seen in divergent and parallel mode (in the virtual telescope). The last image on the right shows the superimposition of the two ellipses, where the blue one is the one with the corrected `psi` angle and the red one is the ellipse in parallel mode. Images by T. Gasparetto.

with the MC position can be done. To perform the reconstruction the Hillas parameter called *psi* is used: it is the angle between the major-axis of the ellipse and the X axis of the camera (see Figure 2.9) and it gives information about the rotation of the ellipse in the camera frame. This angle is used to define a line passing through the telescope position and the intersection of all the lines coming from each telescope gives the impact point in the *TiltedGroundFrame*. In the divergent mode, the telescope pointings do not coincide with the array pointing, therefore the camera planes of each telescope are not parallel to the *TiltedGroundFrame*.

To resolve the issue, when computing the *psi* angle, the ellipse is projected into a virtual telescope that has the same pointing as the array (Figure 6.4). It corresponds to how the event would have been observed in the camera if the pointing was like the standard parallel mode.

In this way *psi* is corrected accordingly to this virtual camera frame parallel to the *TiltedGroundFrame*, and when computing the impact point through the function `estimate_core_position`, the corrected *psi* is used. The correction is implemented in the function `initialize_hillas_planes` of the class `HillasReconstructor`.

The method has been tested on the first sample of divergent simulations and the improvement in the reconstruction is proved (see Figure 6.5).

6.3.2 Results

As anticipated in Section 4.3, I performed the analysis of the simulations defined in Table 6.1 with the use of `protopipe`. A different script and its associated file, where the user can change the value of the parameters according to the analysis' type, takes care of each part of the analysis.

For the reconstruction of the events the values used in the quality cut for the image selection are: at least 50 phe and 3 surviving pixels, image's center of gravity within 80% of camera radius and ellipticity between 0.1 and 0.6. Moreover at least
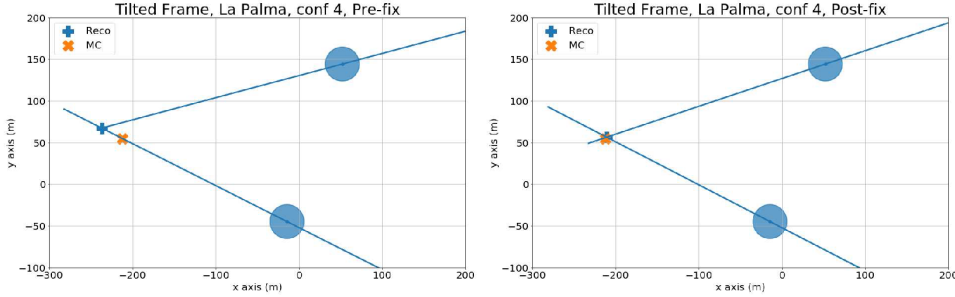
Figure 6.5: Results of the impact point reconstruction for the same event before (left) and after (right) the correction to the `psi` angle. The blue cross represents the reconstructed position, while the orange cross the MC one.

3 telescopes have to be triggered to consider the event for the reconstruction and the picture threshold, the boundary and the minimum number of neighbors in the cleaning were set as 6, 3, 2 for the LSTCam and 8, 4, 2 for the NectarCam respectively (see Section 4.3.2 on cleaning).

For every simulated configuration, the models for the energy reconstruction and the gamma/hadron separation have been generated using a part of the data; the remaining data have been used for the analysis of DL2 data. The percentage of data used in each step is the default one, already mentioned in Section 4.3.2. For the analysis were used 50% of the gammas, 40% of the protons and 100% of the electrons in the original dataset. The remaining percentage was used for the models. This separation is not optimized for the divergent configuration: the one which gave the best results in the analysis of the parallel one was used. It is suggested as default in protopipe's documentation, but it has to be further investigated.

Regarding the models, it can be seen from the plots in Appendix B that, especially at low energy, the statistic is very low and the created models are preliminary. As expected they worsen with increasing divergence, also because of the lower statistics. A deep study on the best parameter to use in the regressor and classifier has to be performed, together with a better comprehension of the needed statistic in the divergent pointing simulations.

The last part of the analysis is the computation of the performances. The script implemented in `protopipe` was missing features like the calculation of the errors, and it didn't contain all the CTA requirements. For this reasons, together with Gaia Verna, PhD student at Aix-Marseille Université, I implemented a new script based on `pyirf` functions to calculate the DL3 data. `pyirf` is actually a spin-off of the `protopipe` performance module: it has been further developed to reach the requirements of the observatory. In the new script we implemented the bootstrap method, already mentioned in Section 4.3.2, for the computation of the errors associated to the different results. The number of bootstrap iterations to be performed can be set by the user in the configuration files, where also the MC information of the number of simulated event is stored.

Another small addition was the implementation of a cut based on the multiplicity. Multiplicity refers to the number of telescope images used to reconstruct an event. By default is set to 4 (changeable from the configuration file). The file obtained from the script can now be used to plot the performances and for this purpose a jupyter notebook was created.

The plots obtained for the five divergent configurations are shown in Appendix B. These simulations have low statistics, especially if compared to the parallel one; therefore, in order to have a better comparison I simulated a bigger production for the configuration 2. The parameters for the simulation were kept the same as the other productions, but a higher number of files was produced: 4170 files for gammas, 8808 for protons and 2044 for electrons in total. For this simulation I also performed an analysis of the threshold layout, namely the minimal array formed by 4 LSTs and 5 MSTs. The results are shown in the following.

Even with small statistics, the analysis shows a performance worsening with increasing divergence, as expected. As it was shown in [130] for the angular resolution, a higher telescope multiplicity improves the performance over the whole energy range, so in further studies a more selective cut could be considered and investigated even if at the expense of a lower number of events.

Before computing the IRFs, direction and gamma/hadron (γ/h) separation cuts are applied to the data. The analysis in `pyirf` is optimized on the EventDisplay analysis, thus the used values could not be the best choice for this particular case and should be optimized in further studies. A series of theta cuts on the gamma direction, defined as the 68% containment of the gammas with respect to the original direction, are calculated and using these the γ/h ones can be computed too. Once the γ/h cuts are defined, the theta cuts are re-calculated a second time but only on the data passing the γ/h cuts. The data with the applied cuts can now be used to compute the IRFs and the sensitivity of the array. Constraining the analysis to include only the best events, enables an accurate and reasonable prediction of the array performance to be calculated.

In all the plots the analysis of a parallel configuration is shown as a reference curve and I also added the CTA performance curve already present by default in `ctaplot` [1], a package that provides reconstruction quality-check plots for IACT such as CTA. This simulation is the one provided for the benchmark of the `protopipe` pipeline in the comparison with the CTA-MARS based analysis. It was analyzed with the same configuration values of the divergent one. The data are plotted versus estimated energy to make it comparable to the reference curve.

Angular resolution

The angular resolution of an array is defined by the reconstruction quality of a point-like source. I only consider on-axis point source simulations; the results would be different when considering off-axis observations of extended sources.

---

[1]https://github.com/cta-observatory/ctaplot

When implemented, the angular resolution is typically defined as the angular distance within which 68% of the events are contained, relative to the true direction. By default is calculated per each true energy bin, however the results shown in Figure 6.7 are plotted versus the reconstructed energy since the reference results are only available in units of estimated energy.

As expected the threshold layout in the energy range covered by the MSTs has a worse angular resolution due to the lower telescope multiplicity. In both cases the parallel configuration performs better than the divergent one at high energies, probably due to the low statistics of highly energetic events.

A similar information comes from the point spread function, that represents the spatial probability distribution of reconstructed event positions for a point source. It gives the angular separation between true and reconstructed directions. In Figure 6.10 a 2D polar representation of the radially symmetric PSF is shown.

Effective area

The sensitivity performance of a Cherenkov telescope is proportional to its effective area. The effective area is given by the acceptance probability of the telescope multiplied by the simulated area, where the acceptance probability is defined as the number of events remaining after the analysis divided by the overall statistics of the simulated events:

$$A_{eff} = \frac{N_{selected}}{N_{sim}} A_{sim} \qquad (6.3)$$

The number of selected events is much lower than the amount of triggered events, due to the noise removal and background suppression. Moreover quality cuts (angular and direction) could be applied in the computation, lowering even more the considered events. In this analysis the effective area is calculated per true energy bin. As expected, the effective area increases with the energy due to increasing Cherenkov light yield of the showers (Figure 6.8). The trend seems in line with the parallel configuration. This is however not true for the threshold layout, where again the effect of less MSTs can be seen. All the quality cuts are applied in the computation and this implicates a decrease in the effective area, especially for low and high energies. At low energies, this could be due to the cut on image Size, while for high energies the number of events passing the cuts is limited mostly by the leakage cut as the shower images are often not fully contained within the camera FoV.

An improvement in the recovery of these images could come by the analysis of truncated images: applying specific quality cuts several images, that normally would be discarded, could be recovered, increasing the statistic at the highest energy. This work is still ongoing and is developed by Gaia Verna [133].

93

Energy resolution

The energy resolution provides an estimation of the goodness of the energy reconstruction. In `pyirf` it can be calculated in two different ways: as the 68% percentile of the relative distance between the true and estimated energy, or using the interquartile range. The latter is defined as half of the width of the central interval between the 75% and 25% percentile, thus is simply calculated as half the difference between the upper and lower quartiles. The second definition is the default option and it was used in the analysis, because at very-high and low energy a gaussian distribution is not expected due to the low-event statistic and worse event reconstruction respectively. The energy bias is always defined as the median of the relative distance distribution.

As can be seen in Figure 6.9, the resolution improves with increasing energy and remains relatively constant like in the reference parallel analysis. However in general the energy regression seems to perform worse than the reference. The energy resolution is determined after both direction and gamma-selection cuts to the data set are applied.

Background rate

The background rate is calculated as the number of background-like events per second, reconstructed energy and solid angle. It is calculated after gamma-selection cuts and it is scaled accordingly to the number of simulated events. The plot can be seen in Figure 6.11. The two curves are very similar, the divergent one has a higher rate at lower energies. At high energy the trend of the parallel curve is probably due to the selection of the cuts.

Sensitivity

The sensitivity is defined as the minimum flux detectable with n sigma significance in a certain time. The definition is related to the concept of detection significance of a point source. Usually a detection correspond to a significance level of at least 5 σ in 50 hours of observations. To calculate the significance of an observation formula 17 from [97] is used:

$$S = \sqrt{2N_{on}\ln(\frac{1+\alpha}{\alpha}\frac{N_{on}}{N_{on}+N_{off}})N_{off}\ln[(1+\alpha)(\frac{N_{off}}{N_{on}+N_{off}})]} \qquad (6.4)$$

where N_{on} and N_{off} are the number of signal-like events for the ON and OFF observations respectively. $\alpha = t_{on}/t_{off}$ represents the ratio between the effective time of the ON and OFF region, and it is the scaling factor between the two. This implies that the number of background events is $N_{bkg} = N_{off} \cdot \alpha$, and the number of signal events is $N_{signal} = N_{on} - \alpha \cdot N_{off}$. In `pyirf` when $N_{on} < \alpha \cdot N_{off}$, the significance is set to zero instead of the negative values that would result from evaluating the formula.

Three conditions are required for the sensitivity in the analysis:

- At least ten weighted signal events;

- The weighted signal must be larger than 5% of the weighted background;

- At least 5 sigma are required.

If the conditions are not met, the sensitivity will be set to undefined (nan). The reference time (50h) is also incorporated by appropriately weighting the events before calculating N_{on} and N_{off}. The sensitivity, calculated according to the Li&Ma likelihood ratio test, can be seen in Figure 6.6. For the baseline layout the sensitivity seems to match the parallel one, doing even better in the core range after 1 TeV. It gets worse at higher energy. The trend follows the one seen in the effective area.
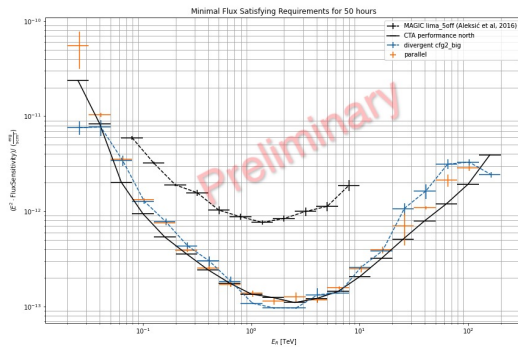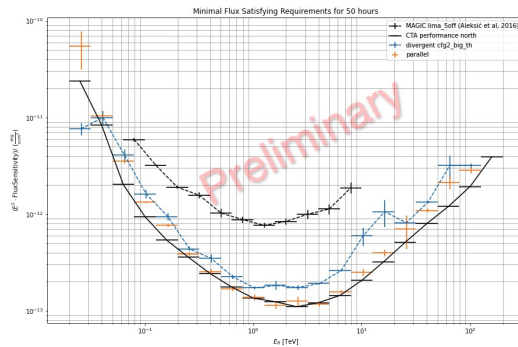
(a) Baseline layout.   (b) Threshold layout.

Figure 6.6: Sensitivity curve for the baseline (a) and threshold (b) layout for 50h of observation.
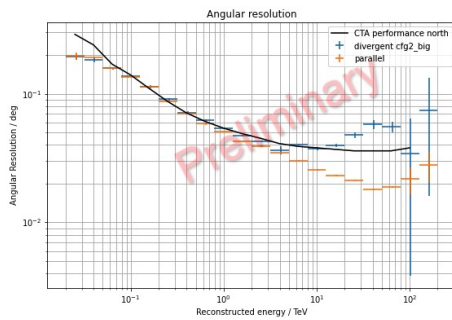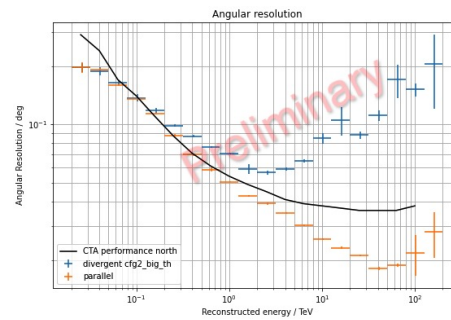
(a) Baseline layout.   (b) Threshold layout.

Figure 6.7: Angular resolution for the baseline (a) and threshold (b) layout.
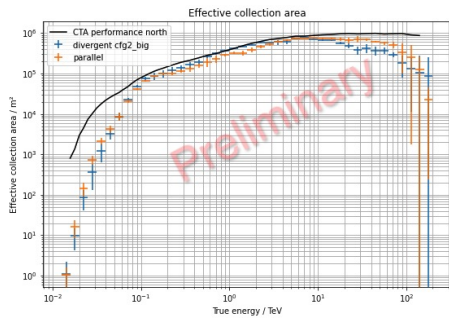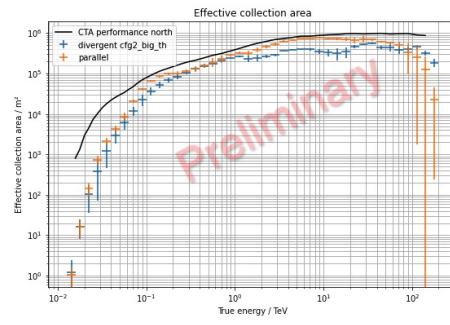
(a) Baseline layout.　　　　　　　　(b) Threshold layout.

Figure 6.8: Effective area after the optimized event selection has been applied for the baseline (a) and threshold (b) layout.
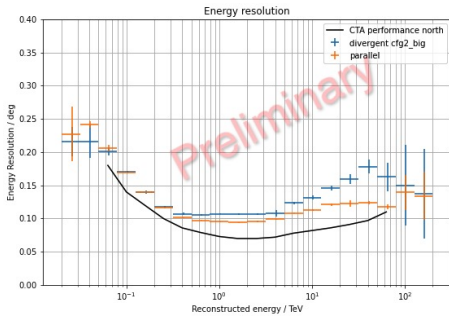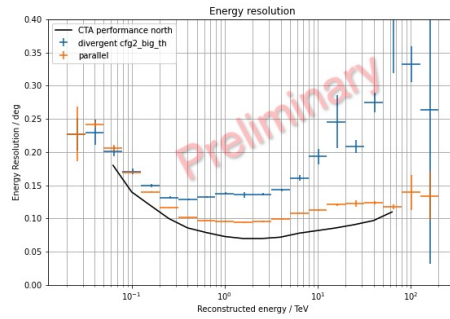
(a) Baseline layout.　　　　　　　　(b) Threshold layout.

Figure 6.9: Energy resolution as function of reconstructed energy for the baseline (a) and threshold (b) layout.
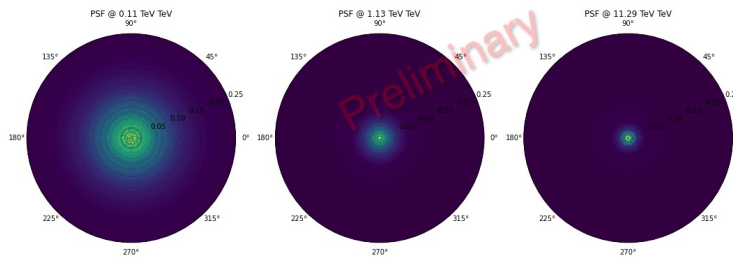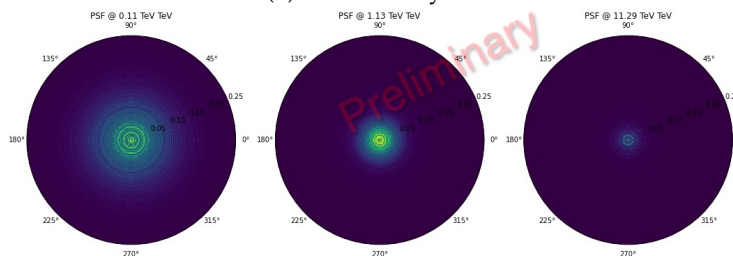
(a) Baseline layout.

(b) Threshold layout.

Figure 6.10: Point Spread Function for the baseline (a) and threshold (b) layout.
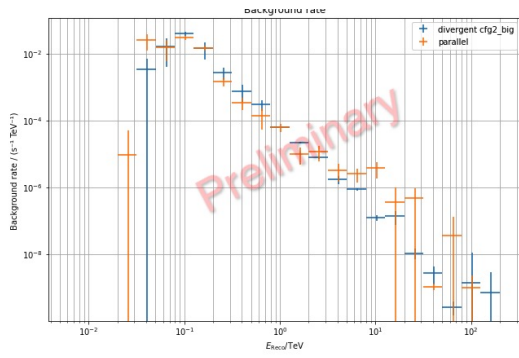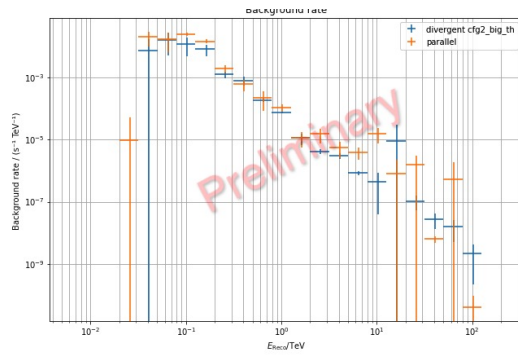
(a) Baseline layout.   (b) Threshold layout.

Figure 6.11: Background rate as function of reconstructed γ-ray energy for the baseline (a) and threshold (b) layout.

Conclusions

The study carried out for this thesis has been mainly centered in the context of the Cherenkov Telescope Array, the next-generation observatory for ground-based very-high-energy gamma-ray astronomy. The work, focused on the analysis pipeline, has spanned from the generation of the dataset to the low-level analysis of the raw data, finishing with the high-level simulations using the Instrument Response Functions to determine the capabilities of CTA for a specific observation mode, called "divergent pointing". CTA will be the first IACT array able to use the divergent mode due to the large number of telescopes that will be built in both sites with respect to the existing experiments. This new type of observing mode has several advantages: the prospect to survey the sky in a more efficient way, to increase the detection probability of VHE transients not driven by alerts, such as serendipitous detection of gamma-ray bursts even in the prompt phase, and to map very-large and non-circular sky regions, like the probability sky maps given by the gravitational wave interferometers.

The divergent pointing mode is considered an important task by several groups of the CTA Consortium due to its wide application to different science cases. Thus, it is important to know the performances of the array in divergent pointing in order to make it a feasible observing mode for future scientific proposals carried on in the Observatory. As pointed out in [63], with ~ 25 MSTs a HFoV of 20° x 20° can be covered with an average of 2-3 telescopes observing an event and with uniform exposure. With an exposure of ~ 4 hours, a sensitivity of 20mCrab at E > 100 GeV can be reached and 1/4 of the sky can be covered in about 100 hours. This is 4 times less than the total time needed in parallel mode at the same sensitivity. The study showed also that the time to complete the survey is smaller in divergent mode as long as the HFoV is more than 10° x 10°. However at the cost of worsening the energy and angular resolution. Similar results were obtained from more recent works, showing that for a survey there could be a gain in both sensitivity and time up to a factor 2, always at the expense of the angular and energy resolution.

All these studies highlighted the promising results of the divergent pointing, but also the missing of a dedicated pipeline to continue them. Therefore the first aim

of my work, conducted within the CTA Analysis and Simulation Working Group, was the adaptation of the data processing pipeline to this new observing mode. Some major changes were implemented into the low-level processing framework (`ctapipe`) to achieve this, and the various tests performed confirmed the validity of the modifications done.

Keeping in mind that the used pipeline is still in development, especially the high-level analysis, the preliminary results obtained seem to agree with the previous studies, showing a worsening of the angular and energy resolution that increases with the divergence of the configuration. The maximum geometrical HFoV reached is given by the configuration 5 with $\sim 230\,\mathrm{deg}^2$ (average telescope multiplicity 3), which is a factor of two lower than the HFoV given by studies considering the southern array (25 MSTs vs 15 MSTs). The minimal threshold of $10°$ x $10°$ mentioned in these studies could be fulfilled by the configuration 2 with $\sim 94\,\mathrm{deg}^2$ or 3 with $\sim 139\,\mathrm{deg}^2$, but the achievement of the required sensitivity has to be more thoroughly studied. A deeper study to optimize the machine-learning models for the energy reconstruction and the γ/h separation is also needed, together with a better comprehension of how the statistic affects the outcomes. In the next version of the pipeline, the models will automatically separate the data in train and test subsets. They will be trained on diffuse gammas instead of point-like ones, improving the realistic description of photo data taking. Moreover in this work protons and electrons were simulated as diffuse using the standard settings, but in the case of divergent pointing, the effective field of view is expected to increase. Thus, in the future analyses it should be checked if the simulated diffuse radius in the MC of protons and electrons should have been increased accordingly, to make sure there are no edge effects in the background estimation. Regarding the background rates observed in the last chapter, an ulterior step would be to check how many of these events are protons and which are electrons. Electrons will most likely be an irreducible background, while proton suppression could probably improve via analysis. The results achieved in this work are the most up-to-date concerning this type of pointing and the work carried out will set a starting point for further and deeper analysis of the simulated data for the divergent pointing. Yet, this preliminary study suggests that the CTA north site can not reach the requirements in divergent mode. A further step would be to perform a similar analysis for the southern array, more suitable for this mode due to the high number of telescopes that would assure a higher minimal multiplicity and also an increase in the maximum HFoV reachable if compared to the northern site. In addition, with the first LST at the ending of its commissioning phase, joint observations with the MAGIC telescopes could be performed, offering a great opportunity to take "divergent data". Of course to use these data for scientific purposes, other issues, like for example the time tagging of the events, should be first solved. However it would be useful for testing the goodness of the implemented divergent reconstruction on real data. If LST would point slightly offset with respect to MAGIC, the data could be used to study LST

off-axis performance too.

A second goal of the work was the testing and validation of the `protopipe` pipeline. I worked together with the group developing the pipeline to help in the debugging of the analysis and making sure that it can be used to produce Instrument Response Functions, not only for the divergent pointing. I focused in particular on the high-level analysis, implementing the method needed for the calculation of the IRFs and the array sensitivity. Comparisons with the EventDisplay and CTA-MARS pipeplines are being done and will help in the fine-tuning of the final pipeline. With the next telescopes being built in the near future, `protopipe`, together with `pyirf` and `ctapipe`, will be the software used to analyze the coming data and its development is of crucial importance.

Pointing tool plots

In the following plots relative to the pointing pattern (Chapter 6) are displayed for each configuration.

The first plot (a) of each figure is the skymap in sky coordinates of the configuration. The red circles represent the MSTs FoV, while the darker ones are the LSTs FoV. The center of each FoV is labeled with the associated telescope ID.

The second plots (b) are the scatter plots of the telescope FoV multiplicity. The first two plots represent the single LSTs and MSTs sub-arrays with maximum multiplicity 4 and 15 respectively, while the third one is the scatter plot of the whole array with 19 telescopes.

The last plots (c) are a chart where the HFoV is plotted against the multiplicity. Again the plots relative to the LSTs and MSTs sub-array are shown together with the one for the whole array.

At the end in Figure A.6, similar plots for the parallel configuration are shown for comparison.
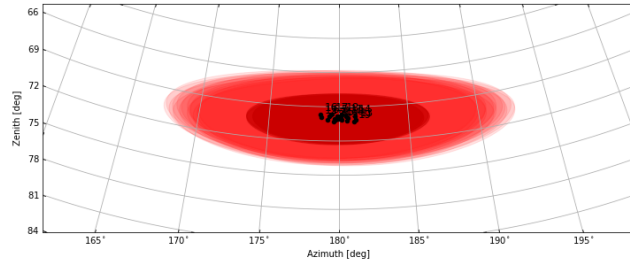
(a) Skymap.
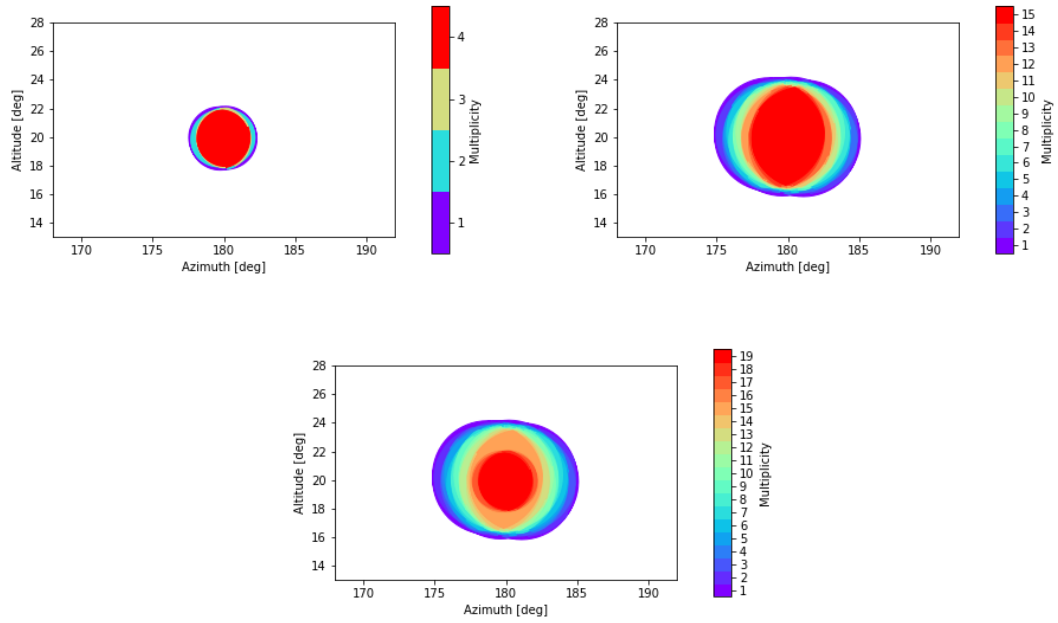
(b) Multiplicity plot for the LSTs and MSTs sub-arrays (above) and for the whole array (below).
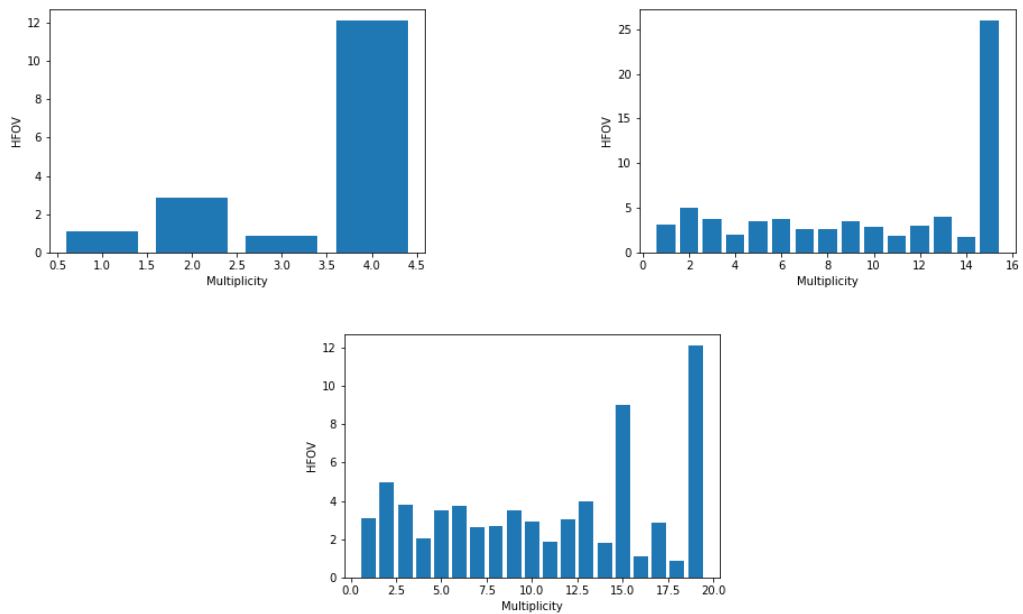
(c) HFoV vs telescope multiplicity. The LSTs and MSTs sub-arrays only (above) and the full array (below).
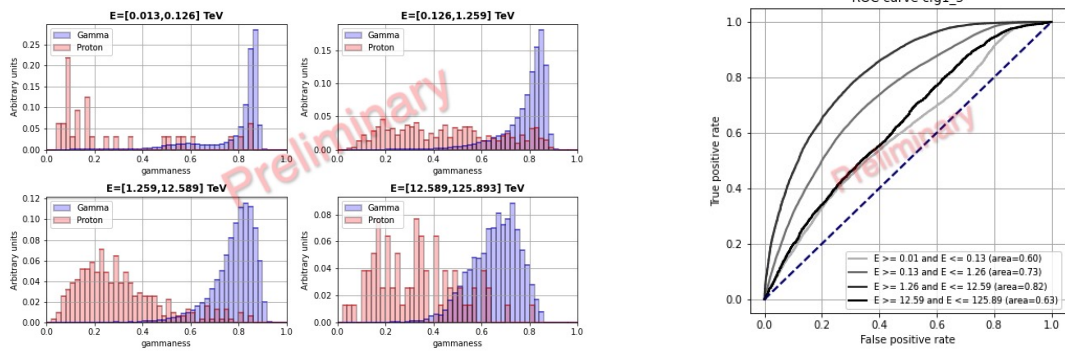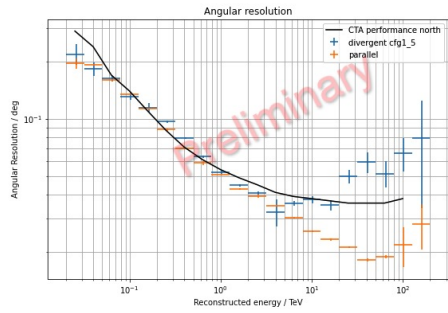
Figure A.1: Configuration x1.5.
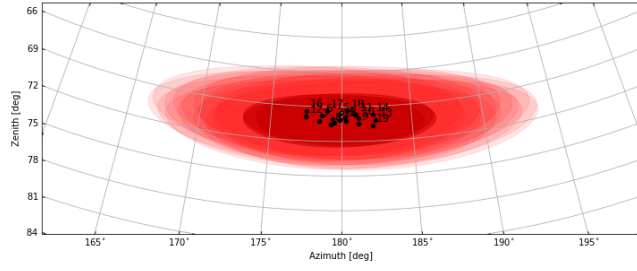
(a) Skymap.
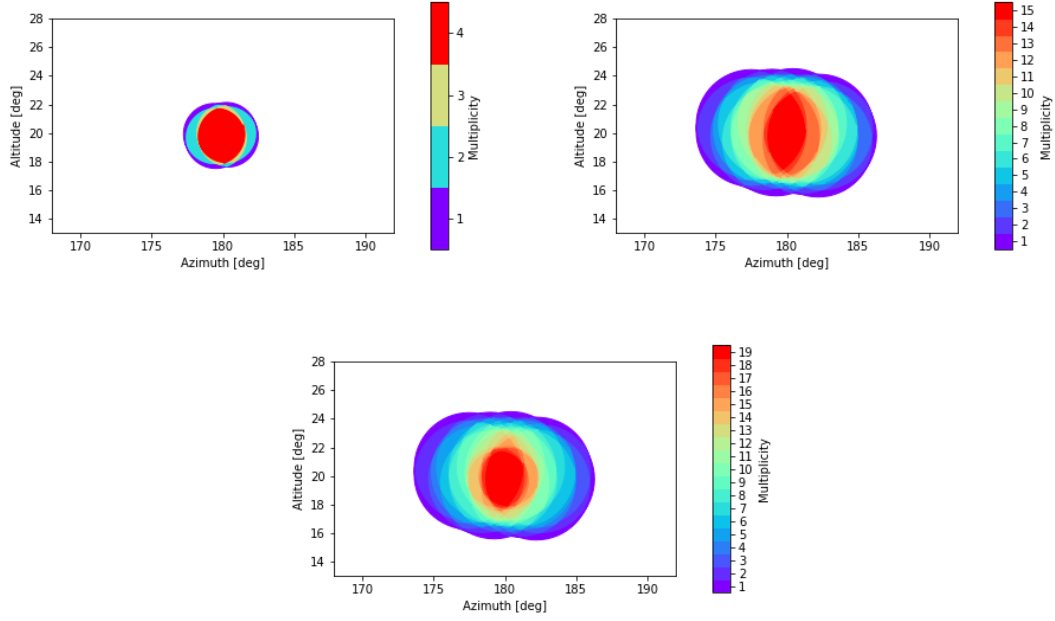
(b) Multiplicity plot for the LSTs and MSTs sub-arrays (above) and for the whole array (below).
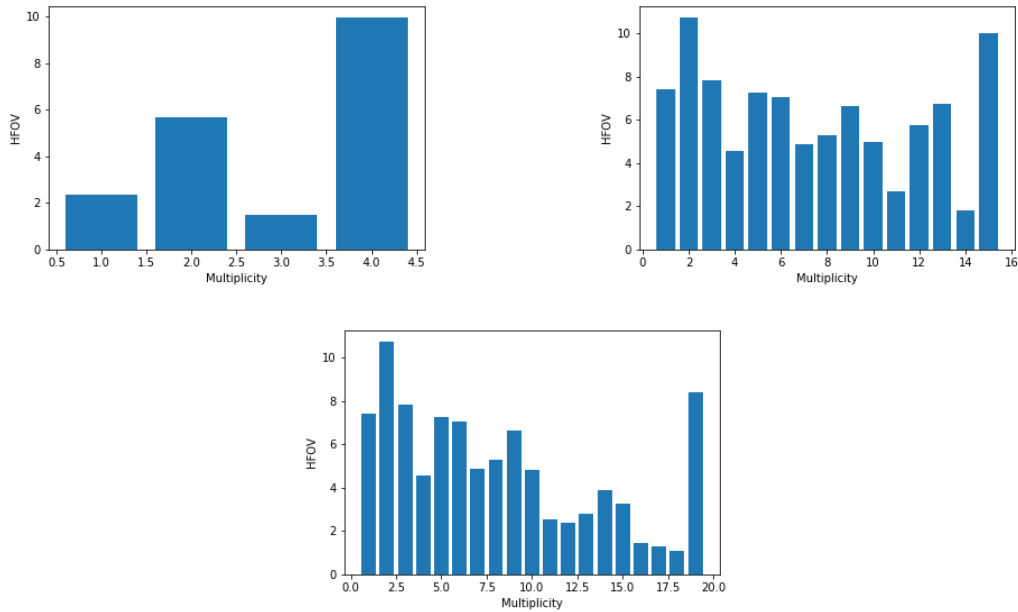
(c) HFoV vs telescope multiplicity. The LSTs and MSTs sub-arrays only (above) and the full array (below).

Figure A.2: Configuration x2.
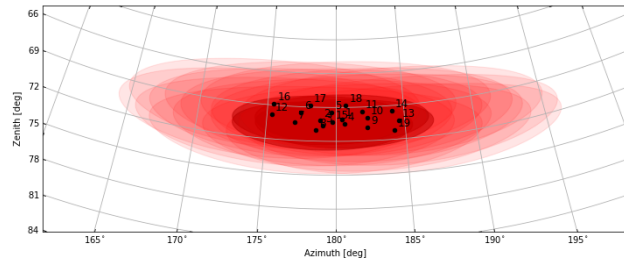
(a) Skymap.
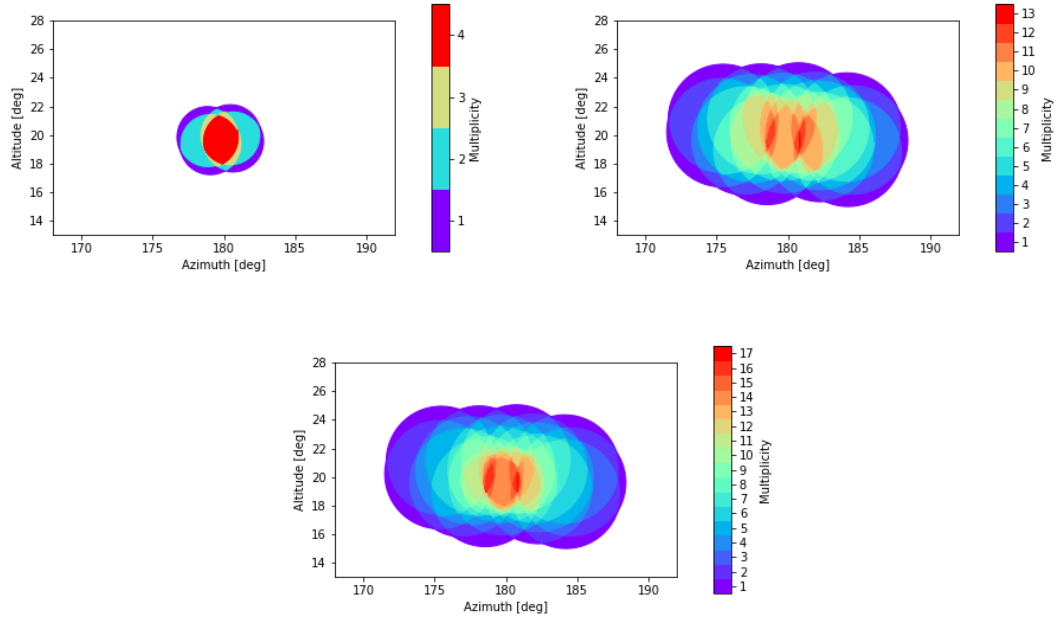
(b) Multiplicity plot for the LSTs and MSTs sub-arrays (above) and for the whole array (below).
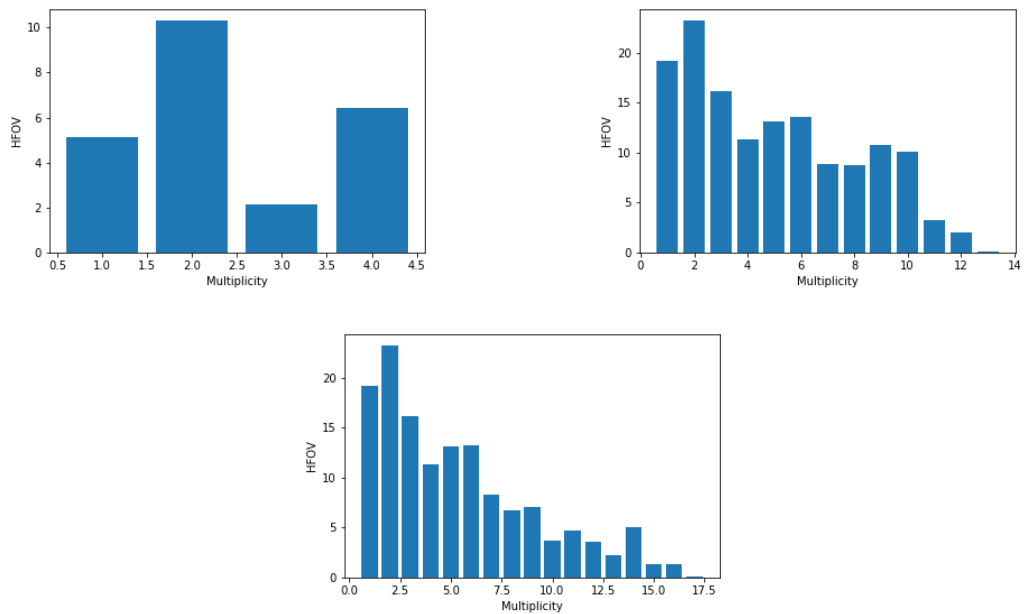
(c) HFoV vs telescope multiplicity. The LSTs and MSTs sub-arrays only (above) and the full array (below).

Figure A.3: Configuration x3.
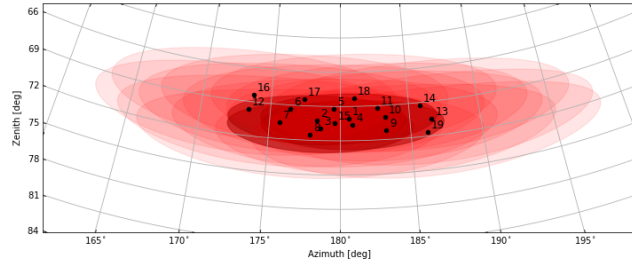
(a) Skymap.
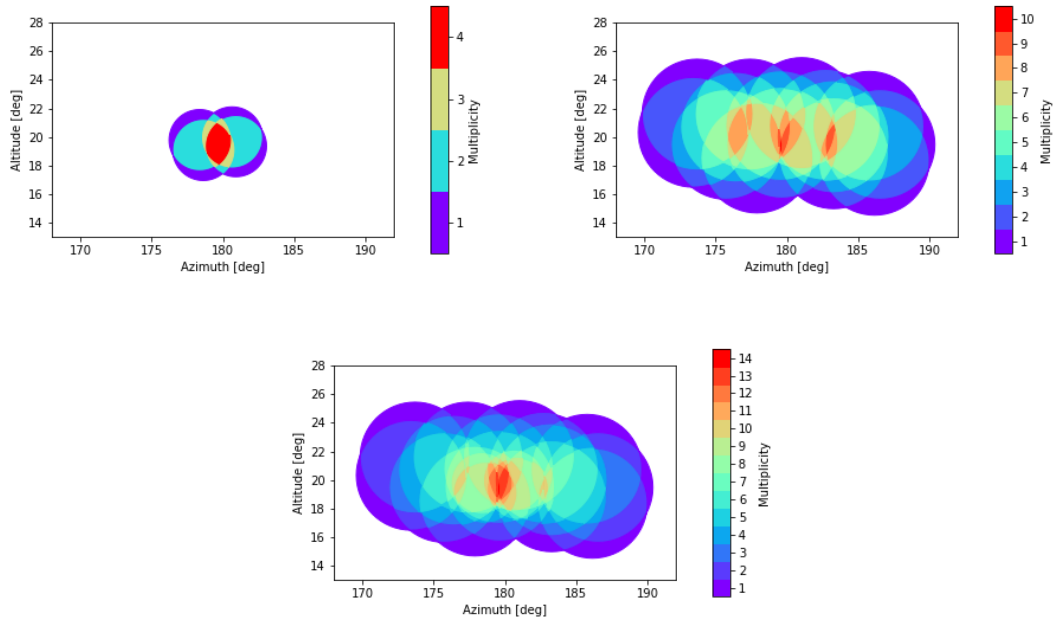
(b) Multiplicity plot for the LSTs and MSTs sub-arrays (above) and for the whole array (below).
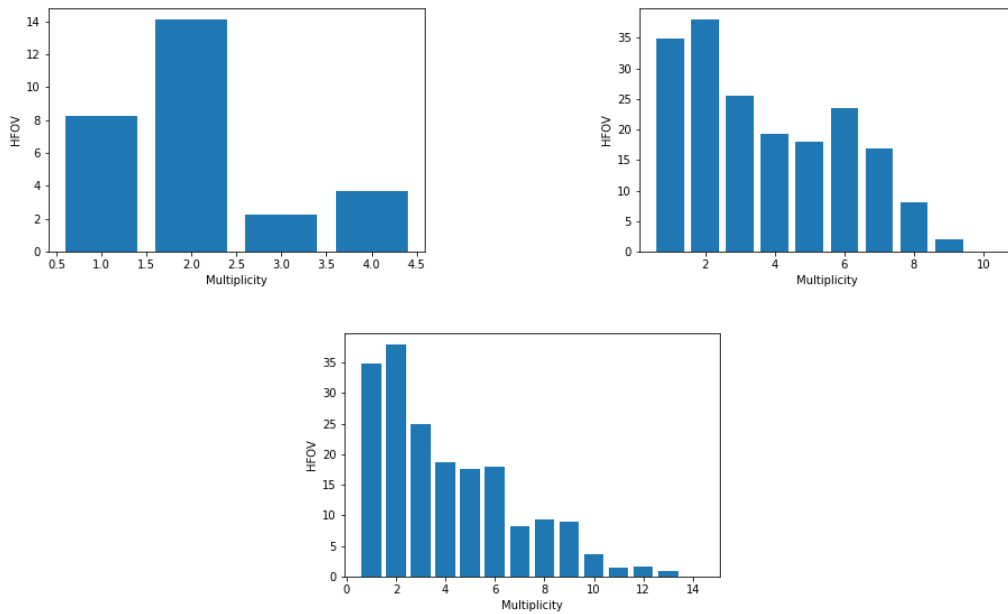
(c) HFoV vs telescope multiplicity. The LSTs and MSTs sub-arrays only (above) and the full array (below).

Figure A.4: Configuration x4.
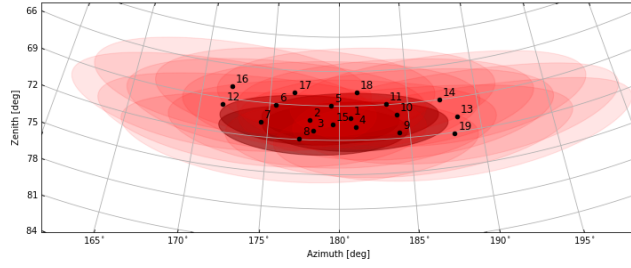
(a) Skymap.
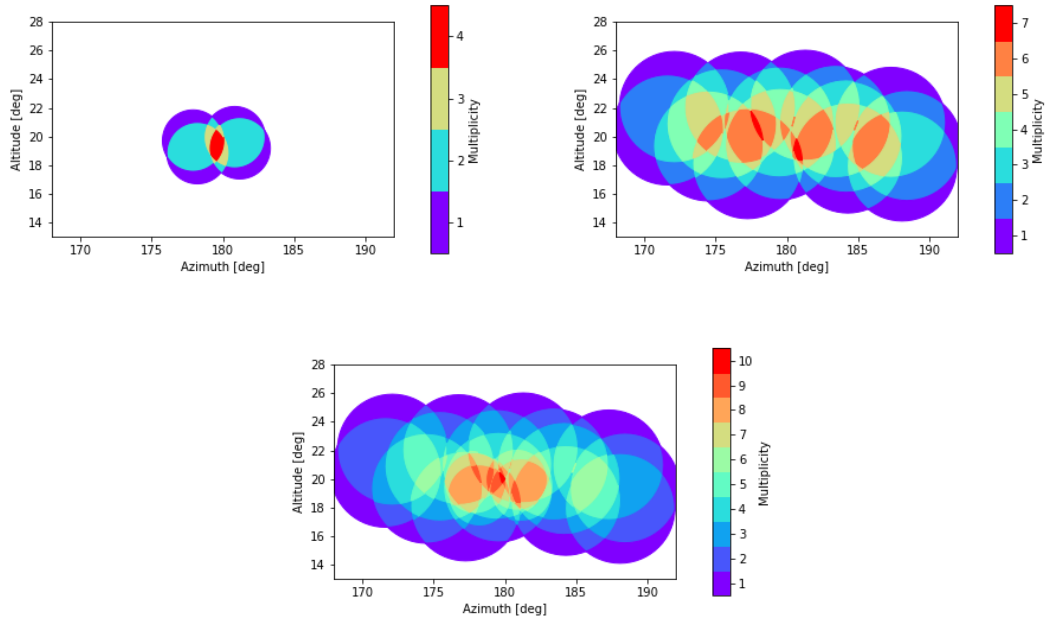
(b) Multiplicity plot for the LSTs and MSTs sub-arrays (above) and for the whole array (below).
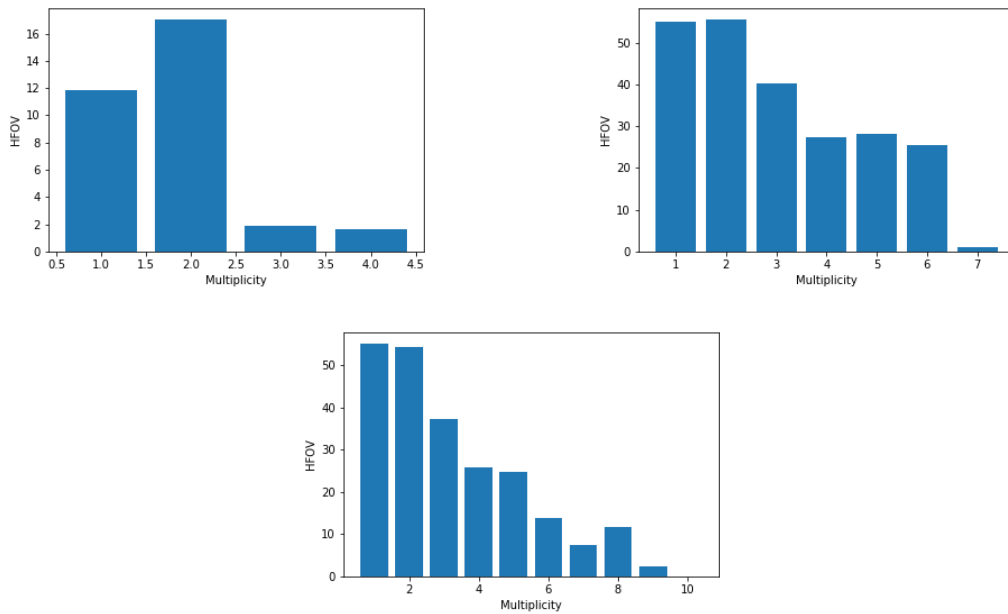
(c) HFoV vs telescope multiplicity. The LSTs and MSTs sub-arrays only (above) and the full array (below).

Figure A.5: Configuration x5.
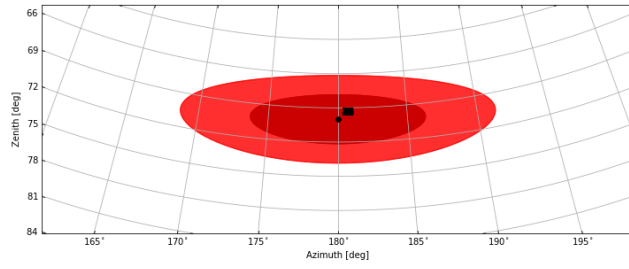
(a) Skymap.
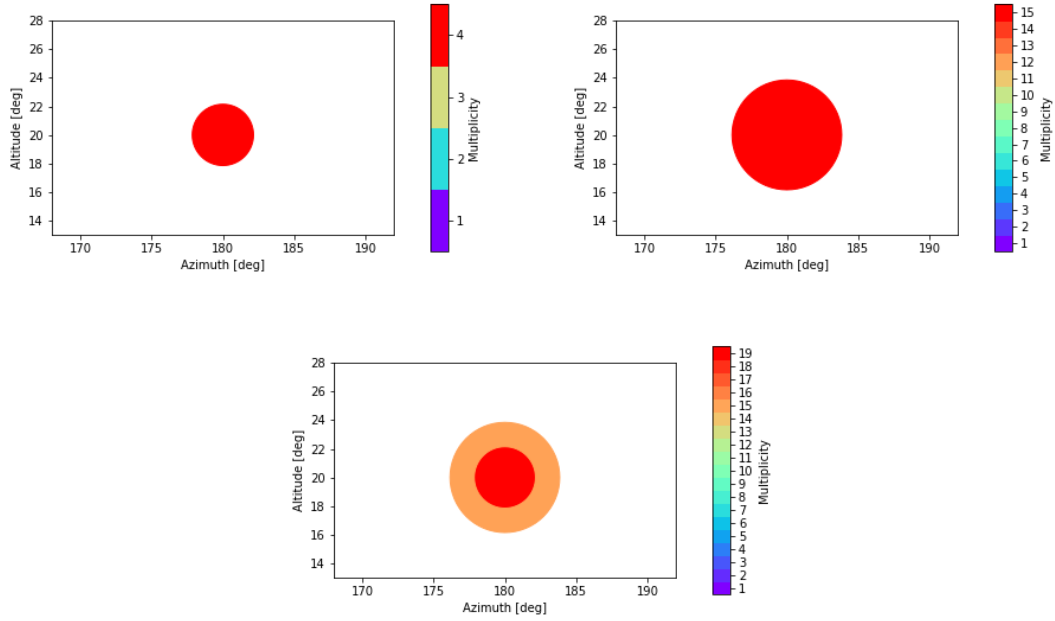
(b) Multiplicity plot for the LSTs and MSTs sub-arrays (above) and for the whole array (below).
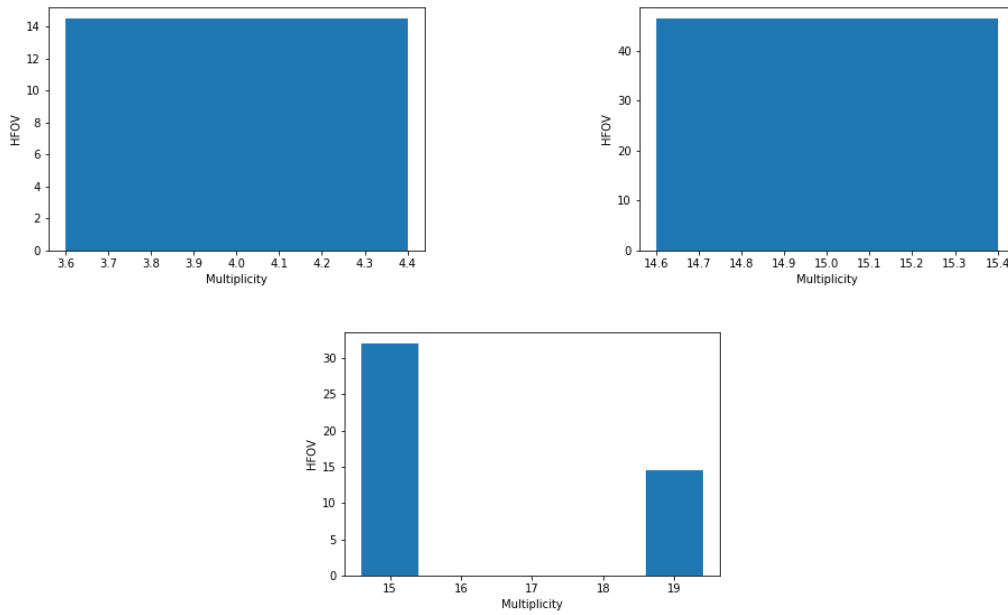
(c) HFoV vs telescope multiplicity. The LSTs and MSTs sub-arrays only (above) and the full array (below).

Figure A.6: Parallel configuration.

Performance studies plots

In each of the following figures, the outcomes of the diagnostic performed on the classifier model of each configuration are shown. Following these plots, the results obtained using those gamma/hadron cuts for the angular resolution, the collection area, the energy resolution, the background rate, the PSF and the sensitivity are reported.

For the diagnostic the Receiver Operating Characteristic (ROC) curve and the score distribution are shown. The ROC curve is used to evaluate the classifier output quality. The true positive rate (TPR) represents the gammas correctly recognized and classified as gammas, while hadrons classified as gammas are represented by the false positive rate (FPR). So the best classifier is the one which provides the maximum TPR for the minimum FPR. Typically the ROC curve shows the probability of false alarm on the x-axis and the probability of detection on the y-axis. This means that the top left corner of the plot represents the perfect point (even if not very realistic) with a false positive rate of zero and a true positive rate of one. So a larger area under the curve (AUC) represents usually a better result. The "steepness" of the ROC curve is also important, since it is ideal to maximize the true positive rate while minimizing the false positive rate. From the score distribution of the classification process, instead, can be seen how the events have been tagged in different energy range. The two populations (gammas and protons) are not well separated in most of the cases and often protons have a high gammaness value (probability to be a gamma).

At the end in Figure B.6, the results of the classification of the configuration 2 bigger production are also shown. The corresponding performances are presented in Chapter 6.

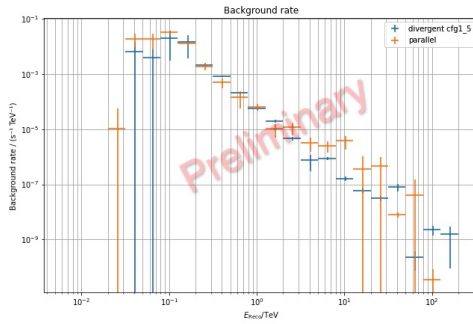(a) Score distribution (left) and ROC curve (right).
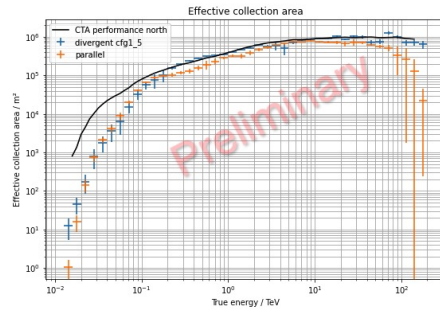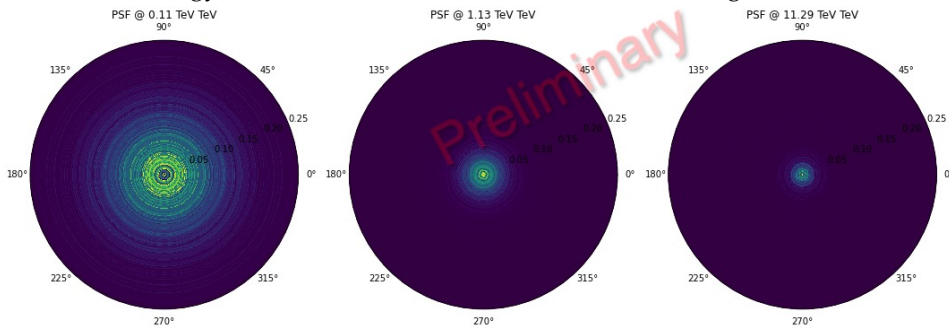

(b) Angular resolution.
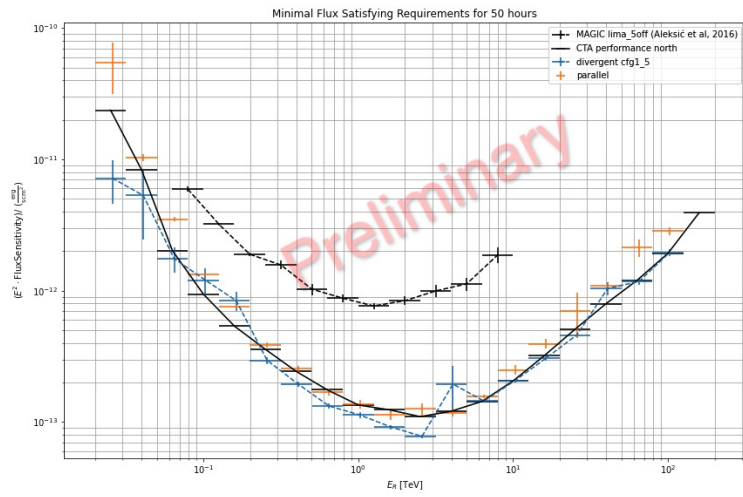

(c) Effective collection area.
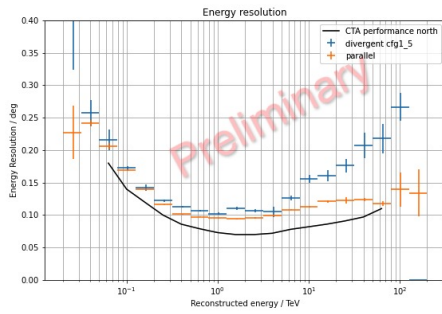
(d) Energy resolution.
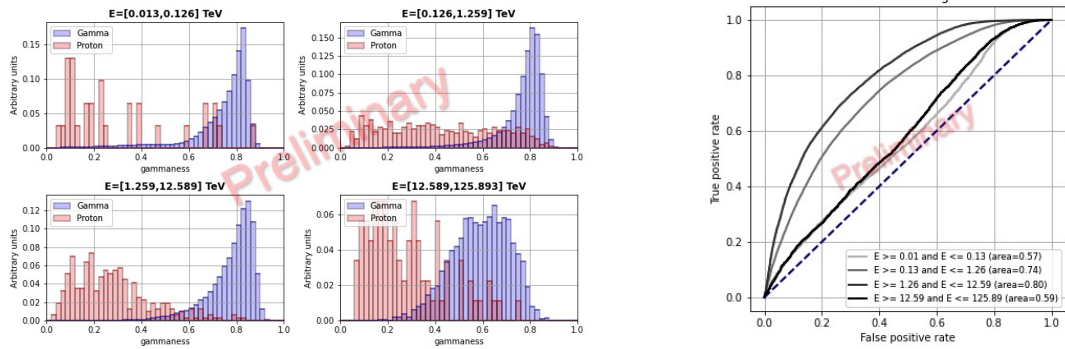

(e) Background rate.
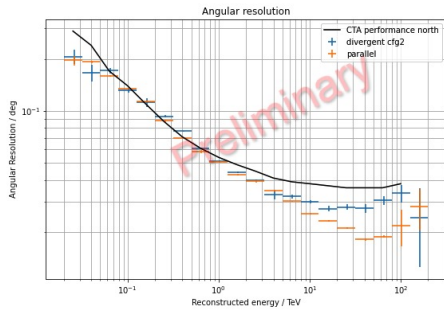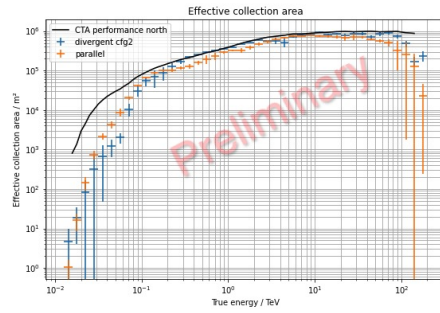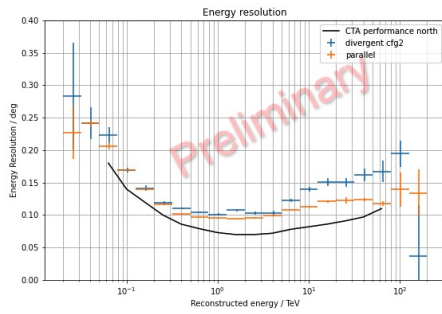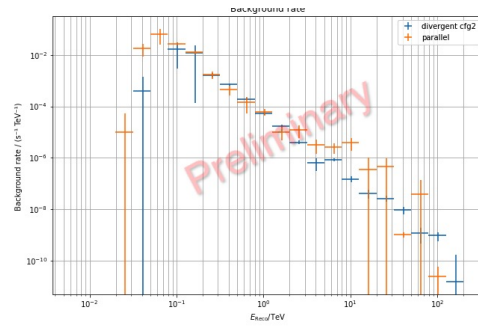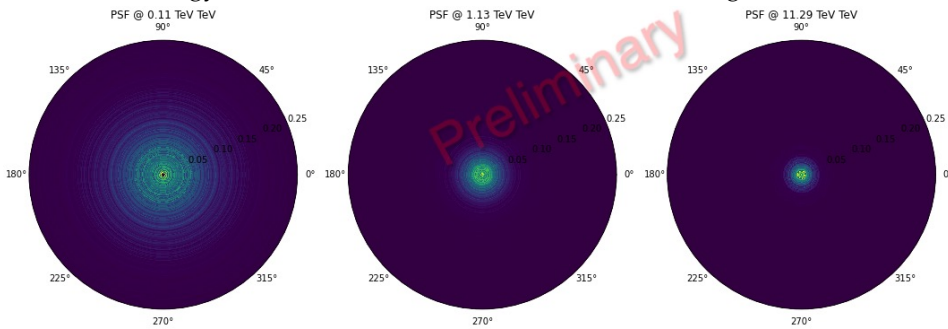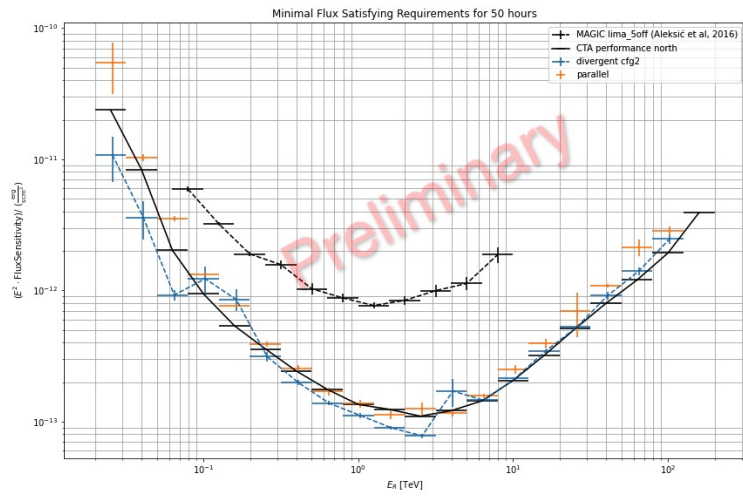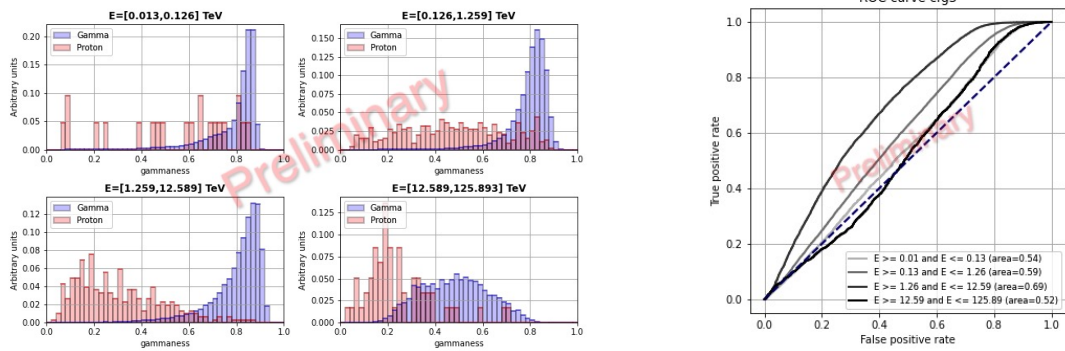

(f) Point Spread Function.

(g) Sensitivity.

Figure B.1: Performances for the configuration x1.5.

(a) Score distribution (left) and ROC curve (right).

(b) Angular resolution.

(c) Effective collection area.

(d) Energy resolution.

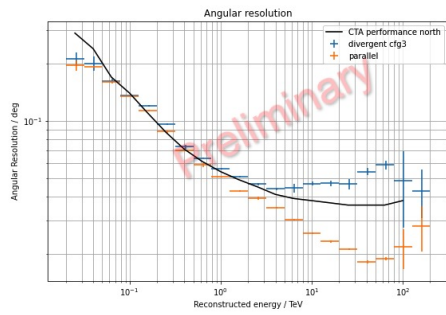

(e) Background rate.

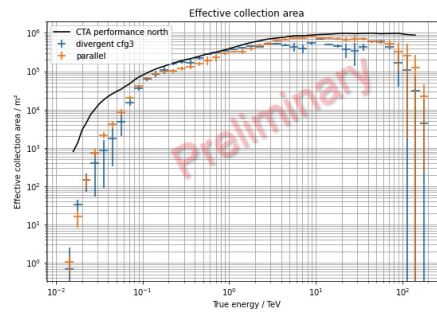(f) Point Spread Function.

(g) Sensitivity.

Figure B.2: Performances for the configuration x2.

(a) Score distribution (left) and ROC curve (right).

(b) Angular resolution.

(c) Effective collection area.

(d) Energy resolution.

(e) Background rate.

(f) Point Spread Function.

116

(g) Sensitivity.

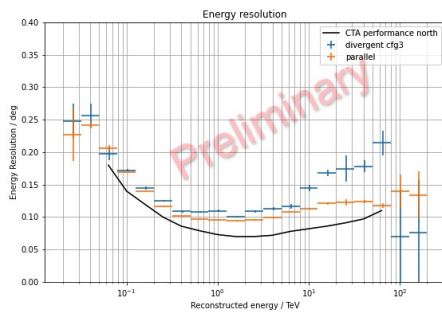Figure B.3: Performances for the configuration x3.

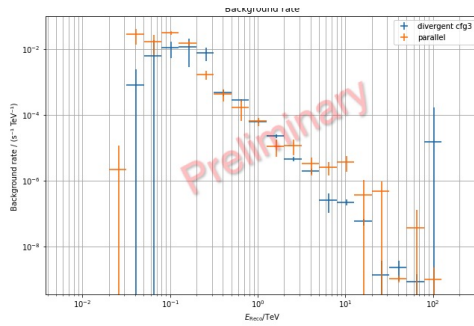(a) Score distribution (left) and ROC curve (right).
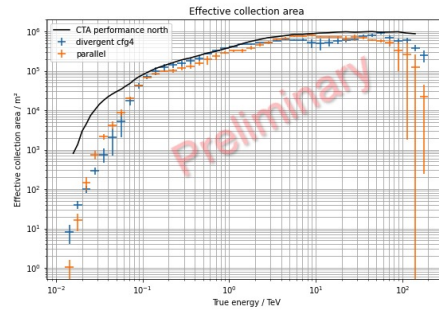
(b) Angular resolution.

(c) Effective collection area.

(d) Energy resolution.

(e) Background rate.

(f) Point Spread Function.

(g) Sensitivity.

Figure B.4: Performances for the configuration x4.

(a) Score distribution (left) and ROC curve (right).
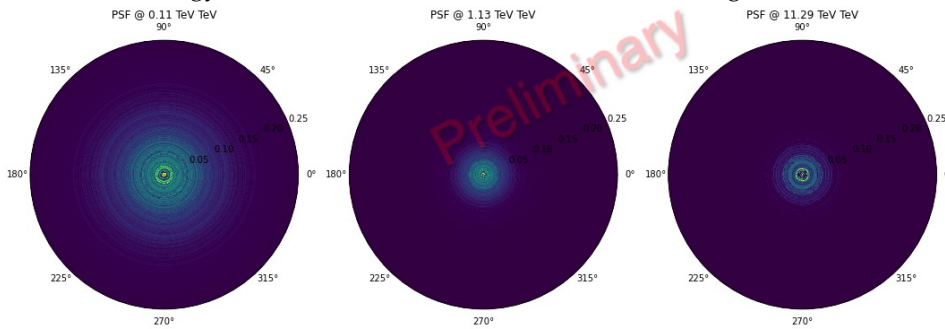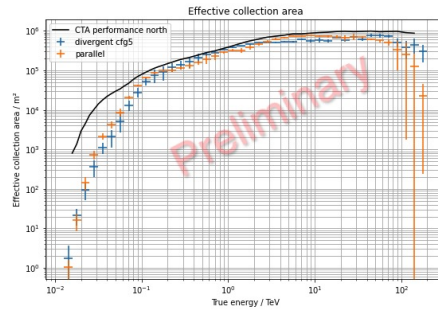

(b) Angular resolution.

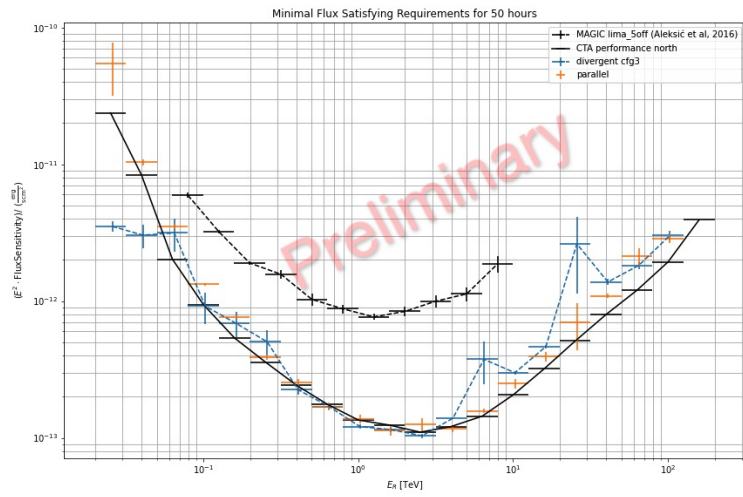

(c) Effective collection area.

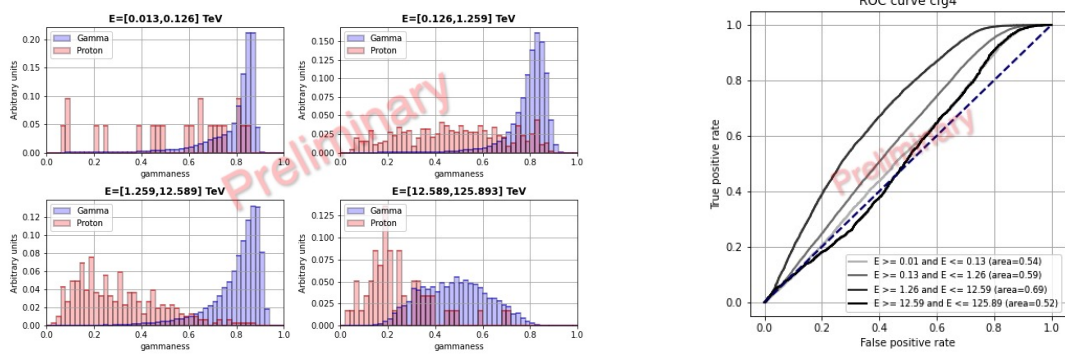(d) Energy resolution.

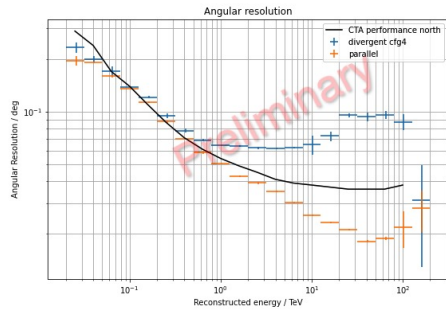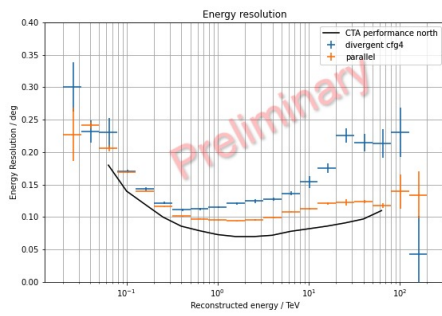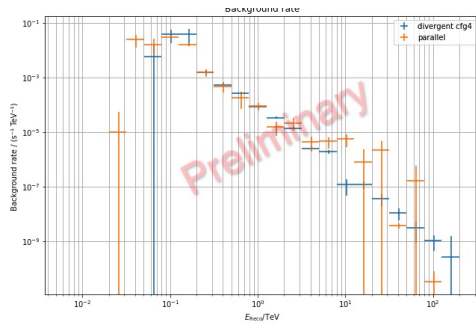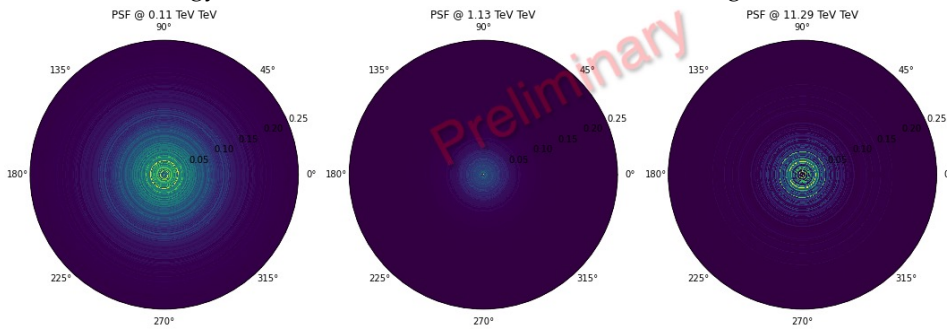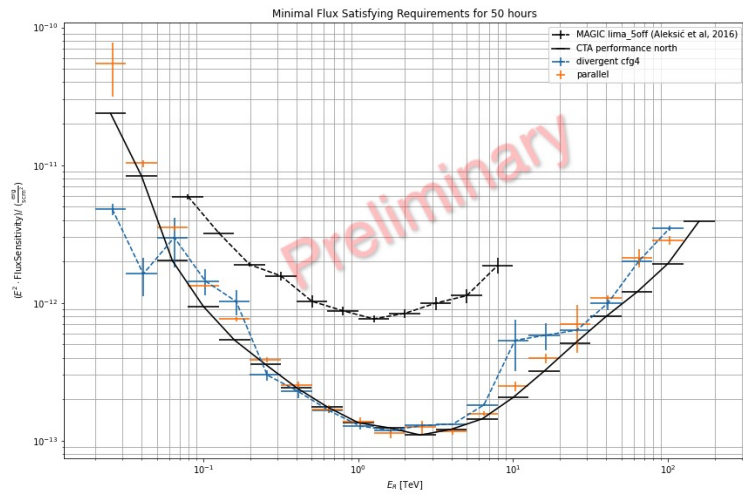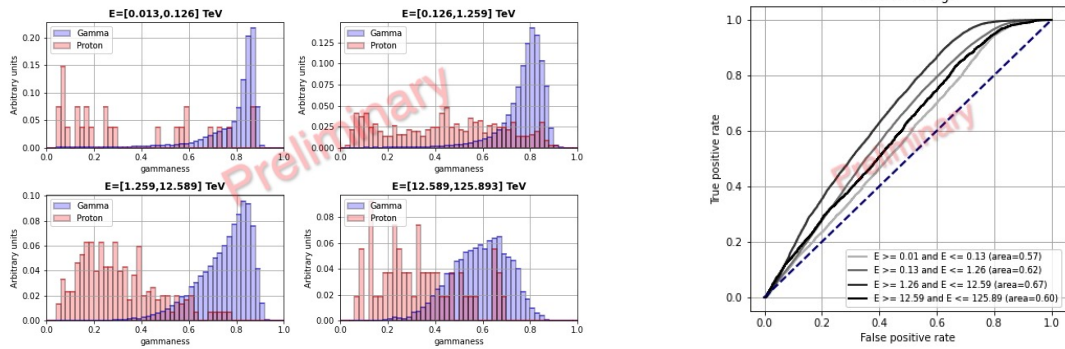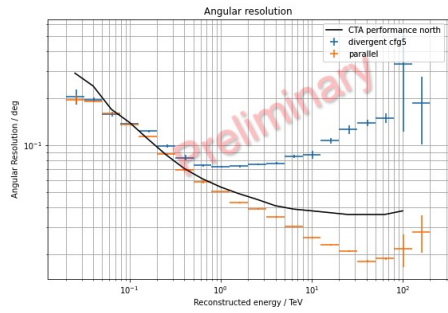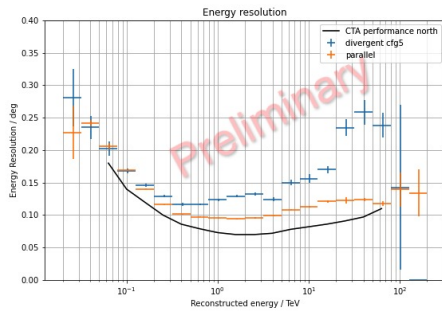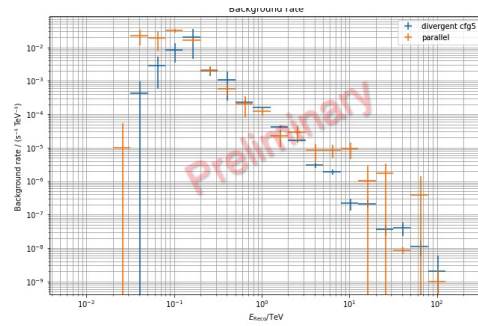(e) Background rate.
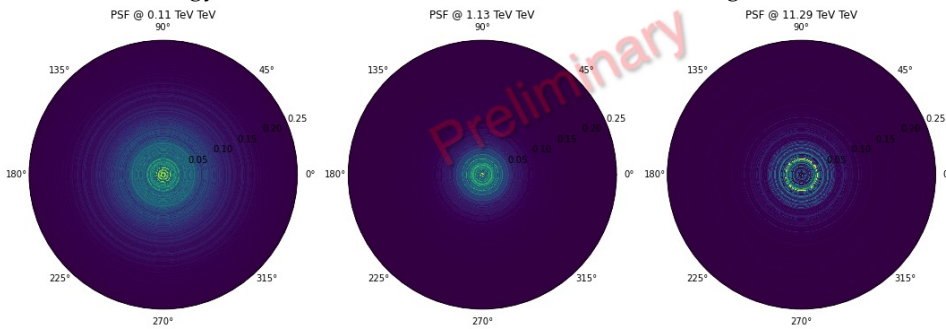
(f) Point Spread Function.
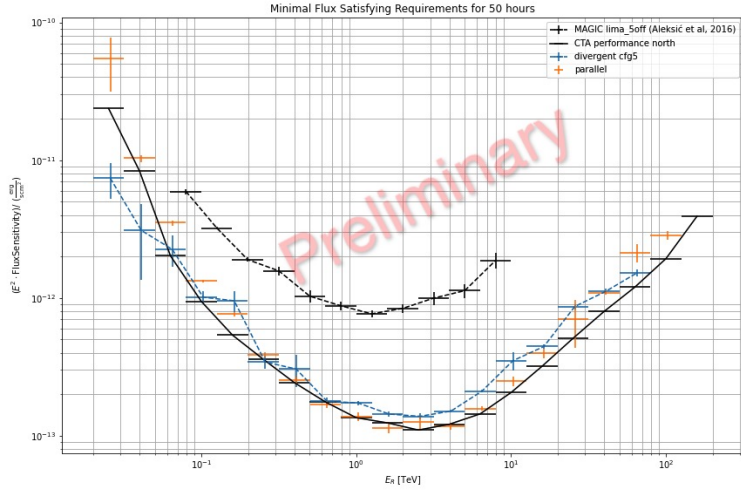
(g) Sensitivity.

Figure B.5: Performances for the configuration x5.
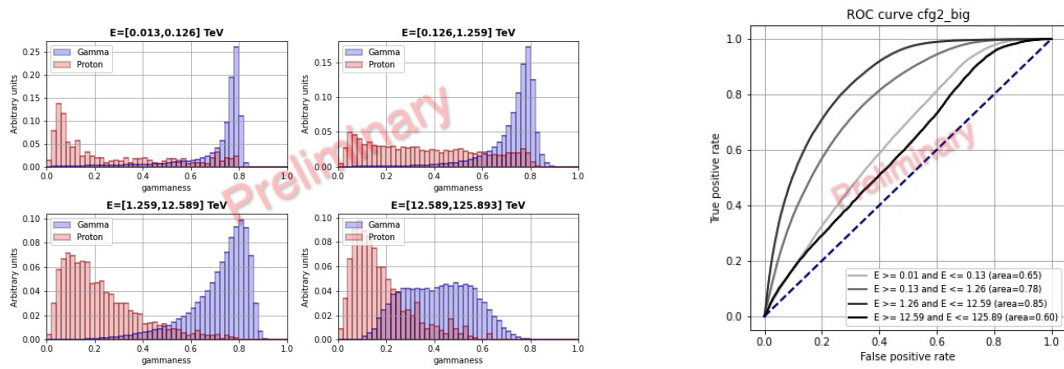
Figure B.6: Score distribution (left) and ROC curve (right) for
the configuration x2 with higher statistics. The performance
plots are shown in Chapter 6.

Bibliography

[1]   A. De Angelis and M. Pimenta. *Introduction to Particle and Astroparticle Physics.* 2018. DOI: 10.1007/978-3-319-78181-5.

[2]   C. Evoli. *The Cosmic-Ray Energy Spectrum.* Oct. 2018. DOI: 10.5281/zenodo. 2360277. URL: https://doi.org/10.5281/zenodo.2360277.

[3]   K. Greisen. "Cosmic Ray Showers". In: *Annual Review of Nuclear and Particle Science* 10 (Jan. 1960), pp. 63–108. DOI: 10.1146/annurev.ns.10.120160. 000431.

[4]   G. T. Zatsepin and V. A. Kuz'min. "Upper Limit of the Spectrum of Cosmic Rays". In: *Soviet Journal of Experimental and Theoretical Physics Letters* 4 (Aug. 1966), p. 78.

[5]   M. S. Longair. *High energy astrophysics.* Cambridge: Cambridge Univ. Press, 2011.

[6]   J. R. Primack et al. "Extragalactic Background Light and Gamma-Ray Attenuation". In: *American Institute of Physics Conference Series.* Ed. by F. A. Aharonian, W. Hofmann, and F. M. Rieger. Vol. 1381. American Institute of Physics Conference Series. Sept. 2011, pp. 72–83. DOI: 10.1063/1.3635825. arXiv: 1107.2566.

[7]   A. Heger et al. "How Massive Single Stars End Their Life". In: *The Astrophysical Journal* 591 (July 2003), pp. 288–300. DOI: 10.1086/375341. eprint: astro-ph/0212469.

[8]   M. Ackermann et al. "Detection of the Characteristic Pion-Decay Signature in Supernova Remnants". In: *Science* 339 (Feb. 2013), pp. 807–811. DOI: 10. 1126/science.1231160. arXiv: 1302.3307 [astro-ph.HE].

[9]   F. Acero et al. "Localizing the VHE γ-ray source at the Galactic Centre". In: *Monthly Notices of the Royal Astronomical Society* 402 (Mar. 2010), pp. 1877–1882. DOI: 10.1111/j.1365-2966.2009.16014.x. arXiv: 0911.1912.

[10] Y. Maeda et al. "A Chandra Study of Sagittarius A East: A Supernova Remnant Regulating the Activity of Our Galactic Center?" In: *The Astrophysical Journal* 570 (May 2002), pp. 671–687. DOI: 10.1086/339773. eprint: astro-ph/0102183.

[11] T. Piran. "The physics of gamma-ray bursts". In: *Reviews of Modern Physics* 76 (Oct. 2004), pp. 1143–1210. DOI: `10.1103/RevModPhys.76.1143`. eprint: `astro-ph/0405503`.

[12] M. Pitkin et al. "Gravitational Wave Detection by Interferometry (Ground and Space)". In: *Living Reviews in Relativity* 14.1, 5 (July 2011), p. 5. DOI: `10.12942/lrr-2011-5`. arXiv: `1102.3355 [astro-ph.IM]`.

[13] B.P. Abbott et al. "GWTC-1: A Gravitational-Wave Transient Catalog of Compact Binary Mergers Observed by LIGO and Virgo during the First and Second Observing Runs". In: *Physical Review X* 9.3 (2019). ISSN: 2160-3308. DOI: `10.1103/physrevx.9.031040`. URL: `http://dx.doi.org/10.1103/PhysRevX.9.031040`.

[14] R. Abbott et al. "GWTC-2: Compact Binary Coalescences Observed by LIGO and Virgo During the First Half of the Third Observing Run". In: (Oct. 2020). arXiv: `2010.14527 [gr-qc]`.

[15] B. P. Abbott et al. "GW170817: Observation of Gravitational Waves from a Binary Neutron Star Inspiral". In: 119.16, 161101 (Oct. 2017), p. 161101. DOI: `10.1103/PhysRevLett.119.161101`. arXiv: `1710.05832 [gr-qc]`.

[16] B. P. Abbott et al. "Gravitational Waves and Gamma-Rays from a Binary Neutron Star Merger: GW170817 and GRB 170817A". In: 848.2, L13 (Oct. 2017), p. L13. DOI: `10.3847/2041-8213/aa920c`. arXiv: `1710.05834 [astro-ph.HE]`.

[17] R. Narayan, B. Paczynski, and T. Piran. "Gamma-Ray Bursts as the Death Throes of Massive Binary Stars". In: 395 (Aug. 1992), p. L83. DOI: `10.1086/186493`. arXiv: `astro-ph/9204001 [astro-ph]`.

[18] *CORSIKA – an Air Shower Simulation Program*. URL: `https://www.ikp.kit.edu/corsika/`.

[19] I. Oya. "Observations of Active Galactic Nuclei with the MAGIC Telescope". PhD thesis. Universidad Complutense de Madrid, 2010.

[20] M. De Naurois. "Very High Energy astronomy from H.E.S.S. to CTA. Opening of a new astronomical window on the non-thermal Universe". Habilitation à diriger des recherches. Université Pierre et Marie Curie - Paris VI, Mar. 2012. URL: `https://tel.archives-ouvertes.fr/tel-00687872`.

[21] J. Matthews. "A Heitler model of extensive air showers". In: *Astroparticle Physics* 22.5-6 (Jan. 2005), pp. 387–397. DOI: `10.1016/j.astropartphys.2004.09.003`.

[22] R. M. Wagner. "Measurement of very high energy gamma-ray emission from four blazars using the MAGIC telescope and a comparative blazar study". PhD thesis. 2006.

[23]   F. Aharonian et al. "High energy astrophysics with ground-based gamma ray detectors". In: *Reports on Progress in Physics* 71.9, 096901 (Sept. 2008), p. 096901. DOI: 10.1088/0034-4885/71/9/096901.

[24]   M. Lopez. "Astronomia Gamma con el Telescopio MAGIC: Observaciones de la Nebulosa y Pulsar del Cangrejo". PhD thesis. Universidad Complutense de Madrid, 2006.

[25]   A. M. Hillas. "Cerenkov light images of EAS produced by primary gamma". In: *International Cosmic Ray Conference* 3 (Aug. 1985).

[26]   D. C. Fidalgo. *Revealing the Most Energetic Light from Pulsars and Their Nebulae.* Springer Theses. Springer, 2019. ISBN: 978-3-030-24193-3, 978-3-030-24194-0. DOI: 10.1007/978-3-030-24194-0.

[27]   R. Lopez-Coto. "Very-high-energy gamma-ray observations of pulsar wind nebulae and cataclysmic variable stars with MAGIC and development of trigger systems for IACTs". PhD thesis. Universitat Autonoma de Barcelona, July 2015.

[28]   M. Peresano. "MAGIC telescopes observations at Very Large Zenith angles and the first neutrino-gamma association". PhD thesis. Udine U., 2018.

[29]   MAGIC Collaboration et al. "MAGIC very large zenith angle observations of the Crab Nebula up to 100 TeV". In: 635, A158 (Mar. 2020), A158. DOI: 10.1051/0004-6361/201936899. arXiv: 2001.09566 [astro-ph.HE].

[30]   HEGRA Collaboration: A. Daum. "First Results on the Performance of the HEGRA IACT Array". In: *arXiv e-prints*, astro-ph/9704098 (Apr. 1997), astro–ph/9704098. arXiv: astro-ph/9704098 [astro-ph].

[31]   T. C. Weekes et al. "VERITAS: the Very Energetic Radiation Imaging Telescope Array System". In: *Astroparticle Physics* 17.2 (May 2002), pp. 221–243. DOI: 10.1016/S0927-6505(01)00152-9. arXiv: astro-ph/0108478 [astro-ph].

[32]   M. K. Daniel and <author pre="for the"VERITAS Collaboration. "Recent results from VERITAS". In: *Journal of Physics Conference Series*. Vol. 1342. Journal of Physics Conference Series. Jan. 2020, p. 012011. DOI: 10.1088/1742-6596/1342/1/012011.

[33]   M. De Naurois. "The H.E.S.S. experiment : current status and future prospects". In: *PoS* ICRC2019 (2020), p. 656. DOI: 10.22323/1.358.0656.

[34]   J. Aleksić et al. "The major upgrade of the MAGIC telescopes, Part I: The hardware improvements and the commissioning of the system". In: *Astroparticle Physics* 72 (Jan. 2016), pp. 61–75. DOI: 10.1016/j.astropartphys.2015.04.004. arXiv: 1409.6073 [astro-ph.IM].

[35] J. Aleksić et al. "The major upgrade of the MAGIC telescopes, Part II: A performance study using observations of the Crab Nebula". In: *Astroparticle Physics* 72 (Jan. 2016), pp. 76–94. DOI: 10.1016/j.astropartphys.2015.02.005. arXiv: 1409.5594 [astro-ph.IM].

[36] *Official CTA website*. URL: https://www.cta-observatory.org.

[37] M. Actis et al. "Design concepts for the Cherenkov Telescope Array CTA: an advanced facility for ground-based high-energy gamma-ray astronomy". In: *Experimental Astronomy* 32.3 (Dec. 2011), pp. 193–316. DOI: 10.1007/s10686-011-9247-0. arXiv: 1008.3703 [astro-ph.IM].

[38] B. S. Acharya et al. "Introducing the CTA concept". In: *Astroparticle Physics* 43 (Mar. 2013), pp. 3–18. DOI: 10.1016/j.astropartphys.2013.01.007.

[39] A. Acharyya et al. "Monte Carlo studies for the optimisation of the Cherenkov Telescope Array layout". In: *Astroparticle Physics* 111 (Sept. 2019), pp. 35–53. DOI: 10.1016/j.astropartphys.2019.04.001. arXiv: 1904.01426 [astro-ph.IM].

[40] G. Maier. "Performance of the Cherenkov Telescope Array". In: *36th International Cosmic Ray Conference (ICRC2019)*. Vol. 36. International Cosmic Ray Conference. July 2019, p. 733. arXiv: 1907.08171 [astro-ph.IM].

[41] K. Bernlöhr et al. "Monte Carlo design studies for the Cherenkov Telescope Array". In: *Astroparticle Physics* 43 (Mar. 2013), pp. 171–188. DOI: 10.1016/j.astropartphys.2012.10.002. arXiv: 1210.3503 [astro-ph.IM].

[42] T. Hassan et al. "Monte Carlo performance studies for the site selection of the Cherenkov Telescope Array". In: *Astroparticle Physics* 93 (2017), 76–85. ISSN: 0927-6505. DOI: 10.1016/j.astropartphys.2017.05.001. URL: http://dx.doi.org/10.1016/j.astropartphys.2017.05.001.

[43] J. Cortina and C. l. Project. "Status of the Large Size Telescopes of the Cherenkov Telescope Array". In: *36th International Cosmic Ray Conference (ICRC2019)*. Vol. 36. International Cosmic Ray Conference. July 2019, p. 653. arXiv: 1907.10146 [astro-ph.IM].

[44] V. V. Vassiliev and S. J. Fegan. "Schwarzschild-Couder two-mirror telescope for ground-based γ-ray astronomy". In: *International Cosmic Ray Conference* 3 (2008), pp. 1445–1448. arXiv: 0708.2741.

[45] R. A. Cameron. "Development of a mid-sized Schwarzschild-Couder Telescope for the Cherenkov Telescope Array". In: *Ground-based and Airborne Telescopes IV*. Vol. 8444. Sept. 2012, p. 844418. DOI: 10.1117/12.926614.

[46] J. A. Barrio and CTA Consortium. "Status of the large size telescopes and medium size telescopes for the Cherenkov Telescope Array observatory". In: *Nuclear Instruments and Methods in Physics Research A* 952, 161588 (Feb. 2020), p. 161588. DOI: 10.1016/j.nima.2018.11.047.

[47]   G. Puehlhofer et al. "FlashCam: a fully-digital camera for the medium-sized telescopes of the Cherenkov Telescope Array". In: *34th International Cosmic Ray Conference (ICRC2015)*. Vol. 34. International Cosmic Ray Conference. July 2015, p. 1039. arXiv: `1509.02434 [astro-ph.IM]`.

[48]   J. F. Glicenstein et al. "NectarCAM : a camera for the medium size telescopes of the Cherenkov Telescope Array". In: *34th International Cosmic Ray Conference (ICRC2015)*. Vol. 34. International Cosmic Ray Conference. July 2015, p. 937. arXiv: `1508.06555 [astro-ph.IM]`.

[49]   S. Scuderi. "The ASTRI Program". In: *European Physical Journal Web of Conferences*. Vol. 209. European Physical Journal Web of Conferences. Sept. 2019, p. 01001. DOI: `10.1051/epjconf/201920901001`.

[50]   O. Le Blanc et al. "Final characterisation and design of the Gamma-ray Cherenkov Telescope (GCT) for the Cherenkov Telescope Array". In: *Ground-based and Airborne Telescopes VII*. Ed. by Heather K. Marshall and Jason Spyromilio. Vol. 10700. Society of Photo-Optical Instrumentation Engineers (SPIE) Conference Series. July 2018, p. 1070010. DOI: `10.1117/12.2313158`.

[51]   M. Heller et al. "The SST-1M project for the Cherenkov Telescope Array". In: *36th International Cosmic Ray Conference (ICRC2019)*. Vol. 36. International Cosmic Ray Conference. July 2019, p. 694.

[52]   The CTA Consortium. *Cherenkov Telescope Array: The Next Generation Gamma-ray Observatory*. 2017. arXiv: `1709.05434 [astro-ph.HE]`.

[53]   Cherenkov Telescope Array Consortium et al. *Science with the Cherenkov Telescope Array*. 2019. DOI: `10.1142/10986`.

[54]   F. Acero et al. "Prospects for Cherenkov Telescope Array Observations of the Young Supernova Remnant RX J1713.7-3946". In: 840.2, 74 (May 2017), p. 74. DOI: `10.3847/1538-4357/aa6d67`. arXiv: `1704.04136 [astro-ph.HE]`.

[55]   M. Ackermann et al. "Detection of the Characteristic Pion-Decay Signature in Supernova Remnants". In: *Science* 339.6121 (Feb. 2013), pp. 807–811. DOI: `10.1126/science.1231160`. arXiv: `1302.3307 [astro-ph.HE]`.

[56]   E. O. Angüner et al. "Cherenkov Telescope Array potential in the search for Galactic PeVatrons". In: *36th International Cosmic Ray Conference (ICRC2019)*. Vol. 36. International Cosmic Ray Conference. July 2019, p. 618. arXiv: `1911.06134 [astro-ph.HE]`.

[57]   H. Sol et al. "Active Galactic Nuclei under the scrutiny of CTA". In: *Astroparticle Physics* 43 (Mar. 2013), pp. 215–240. DOI: `10.1016/j.astropartphys.2012.12.005`. arXiv: `1304.3024 [astro-ph.HE]`.

[58]   D. Mazin et al. "KSP: Extragalactic Survey". In: *Science with the Cherenkov Telescope Array*. Ed. by B. S. Acharya et al. 2019, pp. 143–162. DOI: `10.1142/9789813270091_0008`.

127

[59] M. Amenomori et al. "A Northern Sky Survey for Steady Tera-Electron Volt Gamma-Ray Point Sources Using the Tibet Air Shower Array". In: *The Astrophysical Journal* 633 (Nov. 2005), pp. 1005–1012. DOI: 10.1086/491612. eprint: `astro-ph/0502039`.

[60] A. Albert et al. "3HWC: The Third HAWC Catalog of Very-high-energy Gamma-Ray Sources". In: 905.1, 76 (Dec. 2020), p. 76. DOI: 10.3847/1538-4357/abc2d8. arXiv: 2007.08582 [astro-ph.HE].

[61] Zhen Cao et al. "Introduction to Large High Altitude Air Shower Observatory (LHAASO)". In: 43.4 (Oct. 2019), pp. 457–478. DOI: 10.1016/j.chinastron.2019.11.001.

[62] X. Bai et al. "The Large High Altitude Air Shower Observatory (LHAASO) Science White Paper". In: *arXiv e-prints* (May 2019). arXiv: 1905.02773 [astro-ph.HE].

[63] G. Dubus et al. "Surveys with the Cherenkov Telescope Array". In: *Astroparticle Physics* 43 (Mar. 2013), pp. 317–330. DOI: 10.1016/j.astropartphys.2012.05.020. arXiv: 1208.5686 [astro-ph.HE].

[64] L. Gerard for the CTA Consortium. "Divergent pointing with the Cherenkov Telescope Array for surveys and beyond". In: *ArXiv e-prints* (Aug. 2015). arXiv: 1508.06197 [astro-ph.IM].

[65] B. P. Abbott et al. "Prospects for observing and localizing gravitational-wave transients with Advanced LIGO, Advanced Virgo and KAGRA". In: *Living Reviews in Relativity* 23.1, 3 (Sept. 2020), p. 3. DOI: 10.1007/s41114-020-00026-9.

[66] B. P. Abbott et al. "GWTC-1: A Gravitational-Wave Transient Catalog of Compact Binary Mergers Observed by LIGO and Virgo during the First and Second Observing Runs". In: *Phys. Rev. X* 9 (3 2019), p. 031040. DOI: 10.1103/PhysRevX.9.031040. URL: `https://link.aps.org/doi/10.1103/PhysRevX.9.031040`.

[67] M. Seglar-Arroyo et al. "The gravitational wave follow-up program of the Cherenkov Telescope Array". In: *36th International Cosmic Ray Conference (ICRC2019)*. Vol. 36. International Cosmic Ray Conference. July 2019, p. 790. arXiv: 1908.08393 [astro-ph.HE].

[68] A. Mitchell et al. *Instrument Response Functions - Requirements.* Internal Document (Draft V0.1). CTA Observatory. 2020.

[69] K. Kosack et al. *CTA High-Level Data Model Definitions.* Internal Document (Draft V0.4). CTA Observatory. 2017.

[70] K. Kosack, M. Peresano, and CTA Consortium. "ctapipe: A Low-level Data Processing Framework for the Cherenkov Telescope Array". In: *PoS* ICRC2019 (2020), p. 717. DOI: 10.22323/1.358.0717.

[71] M. Peresano. *protopipe*. Version v0.3.0. Nov. 2020. DOI: 10.5281/zenodo. 4303996. URL: https://doi.org/10.5281/zenodo.4303996.

[72] C. Deil et al. "Gammapy - A prototype for the CTA science tools". In: *35th International Cosmic Ray Conference (ICRC2017)*. Vol. 301. International Cosmic Ray Conference. Jan. 2017, p. 766. arXiv: 1709.01751 [astro-ph.IM].

[73] Jürgen Knödlseder et al. *ctools 1.7.3*. Version 1.7.3. Dec. 2020. DOI: 10.5281/ zenodo.4303960. URL: https://doi.org/10.5281/zenodo.4303960.

[74] K. Kosack et al. *CTA Architecture*. Internal Document (Draft V1.0). CTA Observatory. 2018.

[75] D. Heck et al. *CORSIKA: a Monte Carlo code to simulate extensive air showers*. 1998.

[76] K. Bernlöhr. "Simulation of imaging atmospheric Cherenkov telescopes with CORSIKA and sim_ telarray". In: *Astroparticle Physics* 30 (Oct. 2008), pp. 149–158. DOI: 10.1016/j.astropartphys.2008.07.009. arXiv: 0808.2253.

[77] R. Zanin et al. "MARS, The MAGIC Analysis and Reconstruction Software". In: *International Cosmic Ray Conference*. Vol. 33. International Cosmic Ray Conference. Jan. 2013, p. 2937.

[78] G. Maier and J. Holder. "Eventdisplay: An Analysis and Reconstruction Package for Ground-based Gamma-ray Astronomy". In: *35th International Cosmic Ray Conference (ICRC2017)*. Vol. 301. International Cosmic Ray Conference. Jan. 2017, p. 747. arXiv: 1708.04048 [astro-ph.IM].

[79] Maximilian Nöthe et al. *pyirf*. Version v0.4.0. Nov. 2020. DOI: 10.5281/ zenodo.4304466. URL: https://doi.org/10.5281/zenodo.4304466.

[80] Charles R. H. et al. "Array programming with NumPy". In: *Nature* 585.7825 (Sept. 2020), pp. 357–362. DOI: 10.1038/s41586-020-2649-2. URL: https: //doi.org/10.1038/s41586-020-2649-2.

[81] P. Virtanen et al. "SciPy 1.0: Fundamental Algorithms for Scientific Computing in Python". In: *Nature Methods* 17 (2020), pp. 261–272. DOI: 10.1038/ s41592-019-0686-2.

[82] Astropy Collaboration et al. "The Astropy Project: Building an Open-science Project and Status of the v2.0 Core Package". In: 156.3, 123 (Sept. 2018), p. 123. DOI: 10.3847/1538-3881/aabc4f. arXiv: 1801.02634 [astro-ph.IM].

[83] J. Reback et al. *pandas-dev/pandas: Pandas 1.0.3*. Version v1.0.3. Mar. 2020. DOI: 10.5281/zenodo.3715232. URL: https://doi.org/10.5281/zenodo. 3715232.

[84] J. D. Hunter. "Matplotlib: A 2D graphics environment". In: *Computing in Science & Engineering* 9.3 (2007), pp. 90–95. DOI: 10.1109/MCSE.2007.55.

[85] K. Kosack et al. *cta-observatory/ctapipe: v0.7.0*. Version v0.7.0. Aug. 2019. DOI: 10.5281/zenodo.3372211. URL: https://doi.org/10.5281/zenodo.3372211.

[86] The HDF Group. *Hierarchical Data Format, version 5*. 1997-2020. URL: https://www.hdfgroup.org/HDF5/.

[87] K. Kosack et al. *cta-observatory/ctapipe: v0.10.0*. Version v0.10.0. Nov. 2020. DOI: 10.5281/zenodo.4279334. URL: https://doi.org/10.5281/zenodo.4279334.

[88] T. Hastie, R. Tibshirani, and J. Friedman. *The elements of statistical learning: data mining, inference and prediction*. 2nd ed. Springer, 2009. URL: http://www-stat.stanford.edu/~tibs/ElemStatLearn/.

[89] J. Albert et al. "Implementation of the Random Forest method for the Imaging Atmospheric Cherenkov Telescope MAGIC". In: *Nuclear Instruments and Methods in Physics Research A* 588.3 (Apr. 2008), pp. 424–432. DOI: 10.1016/j.nima.2007.11.068. arXiv: 0709.3719 [astro-ph].

[90] M. Krause, E. Pueschel, and G. Maier. "Improved γ/hadron separation for the detection of faint γ-ray sources using boosted decision trees". In: *Astroparticle Physics* 89 (Mar. 2017), pp. 1–9. DOI: 10.1016/j.astropartphys.2017.01.004. arXiv: 1701.06928 [astro-ph.IM].

[91] Y. Becherini et al. "A new analysis strategy for detection of faint γ-ray sources with Imaging Atmospheric Cherenkov Telescopes". In: *Astroparticle Physics* 34.12 (July 2011), pp. 858–870. DOI: 10.1016/j.astropartphys.2011.03.005. arXiv: 1104.5359 [astro-ph.HE].

[92] D. Nieto Castaño et al. "Exploring deep learning as an event classification method for the Cherenkov Telescope Array". In: *35th International Cosmic Ray Conference (ICRC2017)*. Vol. 301. International Cosmic Ray Conference. Jan. 2017, p. 809. arXiv: 1709.05889 [astro-ph.IM].

[93] F. Pedregosa et al. "Scikit-learn: Machine Learning in Python". In: *Journal of Machine Learning Research* 12 (2011), pp. 2825–2830.

[94] H. Drucker. "Improving Regressors using Boosting Techniques". In: *ICML*. 1997, pp. 107–115.

[95] W. Hofmann et al. "Improved energy resolution for VHE gamma-ray astronomy with systems of Cherenkov telescopes". In: *Astropart. Phys.* 12 (2000), pp. 207–216. DOI: 10.1016/S0927-6505(99)00109-7. arXiv: astro-ph/9908092.

[96] C. Nigro et al. "Towards open and reproducible multi-instrument analysis in gamma-ray astronomy". In: 625, A10 (May 2019), A10. DOI: 10.1051/0004-6361/201834938. arXiv: 1903.06621 [astro-ph.HE].

[97] T. P. Li and Y. Q. Ma. "Analysis methods for results in gamma-ray astronomy." In: 272 (Sept. 1983), pp. 317–324. DOI: 10.1086/161295.

[98] A. Berti. "Study of astrophysical transients with the MAGIC telescopes". PhD thesis. Universita' Di Trieste, 2018.

[99] C. Fruck et al. "A novel LIDAR-based Atmospheric Calibration Method for Improving the Data Analysis of MAGIC". In: *arXiv e-prints*, arXiv:1403.3591 (Mar. 2014), arXiv:1403.3591. arXiv: 1403.3591 [astro-ph.IM].

[100] R. Paoletti et al. "The Trigger System of the MAGIC Telescope". In: *IEEE Transactions on Nuclear Science* 54.2 (Apr. 2007), pp. 404–409. DOI: 10.1109/TNS.2007.892649.

[101] D. Tescaro et al. "The readout system of the MAGIC-II Cherenkov Telescope". In: *arXiv e-prints*, arXiv:0907.0466 (July 2009), arXiv:0907.0466. arXiv: 0907.0466 [astro-ph.IM].

[102] J. R. García et al. "Status of the new Sum-Trigger system for the MAGIC telescopes". In: *arXiv e-prints*, arXiv:1404.4219 (Apr. 2014), arXiv:1404.4219. arXiv: 1404.4219 [astro-ph.IM].

[103] D. Tescaro et al. "The MAGIC Telescopes DAQ Software and the On-the-Fly Online Analysis Client". In: *International Cosmic Ray Conference*. Vol. 33. International Cosmic Ray Conference. Jan. 2013, p. 2803. arXiv: 1310.1565 [astro-ph.IM].

[104] V. P. Fomin et al. "New methods of atmospheric Cherenkov imaging for gamma-ray astronomy. I. The false source method". In: *Astroparticle Physics* 2.2 (May 1994), pp. 137–150. DOI: 10.1016/0927-6505(94)90036-1.

[105] R. W. Klebesadel, I. B. Strong, and R. A. Olson. "Observations of Gamma-Ray Bursts of Cosmic Origin". In: 182 (June 1973), p. L85. DOI: 10.1086/181225.

[106] C. Meegan et al. "The spatial distribution of gamma-ray bursts observed by BATSE." In: *Compton Gamma-ray Observatory*. Ed. by M. Friedlander, N. Gehrels, and D. J. Macomb. Vol. 280. American Institute of Physics Conference Series. Jan. 1993, pp. 681–685. DOI: 10.1063/1.44251.

[107] C. Kouveliotou et al. "Identification of Two Classes of Gamma-Ray Bursts". In: 413 (Aug. 1993), p. L101. DOI: 10.1086/186969.

[108] C. A. Meegan et al. "The Third BATSE Gamma-Ray Burst Catalog". In: 106 (Sept. 1996), p. 65. DOI: 10.1086/192329.

[109] E. Costa et al. "Discovery of an X-ray afterglow associated with the γ-ray burst of 28 February 1997". In: 387.6635 (June 1997), pp. 783–785. DOI: 10.1038/42885. arXiv: astro-ph/9706065 [astro-ph].

[110] J. van Paradijs et al. "Transient optical emission from the error box of the γ-ray burst of 28 February 1997". In: 386.6626 (Apr. 1997), pp. 686–689. DOI: 10.1038/386686a0.

[111] M. Ruderman. "Theories of gamma -ray bursts." In: *Seventh Texas Symposium on Relativistic Astrophysics*. Ed. by P. G. Bergman, E. J. Fenyves, and L. Motz. Vol. 262. Oct. 1975, pp. 164–180. DOI: 10.1111/j.1749-6632.1975.tb31430.x.

[112] D. Band et al. "BATSE Observations of Gamma-Ray Burst Spectra. I. Spectral Diversity". In: 413 (Aug. 1993), p. 281. DOI: 10.1086/172995.

[113] B. Zhang et al. "A Comprehensive Analysis of Fermi Gamma-ray Burst Data. I. Spectral Components and the Possible Physical Origins of LAT/GBM GRBs". In: 730.2, 141 (Apr. 2011), p. 141. DOI: 10.1088/0004-637X/730/2/141. arXiv: 1009.3338 [astro-ph.HE].

[114] B. Paczynski. "Gamma-ray bursters at cosmological distances". In: 308 (Sept. 1986), pp. L43–L46. DOI: 10.1086/184740.

[115] Y. Lithwick and R. Sari. "Lower Limits on Lorentz Factors in Gamma-Ray Bursts". In: 555.1 (July 2001), pp. 540–545. DOI: 10.1086/321455. arXiv: astro-ph/0011508 [astro-ph].

[116] P. Kumar and B. Zhang. "The physics of gamma-ray bursts & relativistic jets". In: 561 (Feb. 2015), pp. 1–109. DOI: 10.1016/j.physrep.2014.09.008. arXiv: 1410.0679 [astro-ph.HE].

[117] M. J. Rees and P. Meszaros. "Relativistic fireballs - Energy conversion and time-scales." In: 258 (Sept. 1992), p. 41. DOI: 10.1093/mnras/258.1.41P.

[118] S. Campana et al. "The association of GRB 060218 with a supernova and the evolution of the shock wave". In: 442.7106 (Aug. 2006), pp. 1008–1010. DOI: 10.1038/nature04892. arXiv: astro-ph/0603279 [astro-ph].

[119] S. E. Woosley and A. Heger. "The Progenitor Stars of Gamma-Ray Bursts". In: 637.2 (Feb. 2006), pp. 914–921. DOI: 10.1086/498500. arXiv: astro-ph/0508175 [astro-ph].

[120] W. Fong, E. Berger, and D. B. Fox. "Hubble Space Telescope Observations of Short Gamma-Ray Burst Host Galaxies: Morphologies, Offsets, and Local Environments". In: 708.1 (Jan. 2010), pp. 9–25. DOI: 10.1088/0004-637X/708/1/9. arXiv: 0909.1804 [astro-ph.HE].

[121] M. M. González et al. "A γ-ray burst with a high-energy spectral component inconsistent with the synchrotron shock model". In: 424.6950 (Aug. 2003), pp. 749–751. DOI: 10.1038/nature01869.

[122] K. Hurley et al. "Detection of a γ-ray burst of very long duration and very high energy". In: 372.6507 (Dec. 1994), pp. 652–654. DOI: 10.1038/372652a0.

[123] M. Ackermann et al. "The First Fermi-LAT Gamma-Ray Burst Catalog". In: 209.1, 11 (Nov. 2013), p. 11. DOI: 10.1088/0067-0049/209/1/11. arXiv: 1303.2908 [astro-ph.HE].

[124] M. Ajello et al. "A Decade of Gamma-Ray Bursts Observed by Fermi-LAT: The Second GRB Catalog". In: 878.1, 52 (June 2019), p. 52. DOI: 10.3847/1538-4357/ab1d4e. arXiv: 1906.11403 [astro-ph.HE].

[125] G. Ghisellini et al. "GeV emission from gamma-ray bursts: a radiative fireball?" In: 403.2 (Apr. 2010), pp. 926–937. DOI: 10.1111/j.1365-2966.2009.16171.x. arXiv: 0910.2459 [astro-ph.HE].

[126] F. Piron. "Gamma-ray bursts at high and very high energies". In: *Comptes Rendus Physique* 17.6 (June 2016), pp. 617–631. DOI: 10.1016/j.crhy.2016.04.005. arXiv: 1512.04241 [astro-ph.HE].

[127] R. Mirzoyan. "First time detection of a GRB at sub-TeV energies; MAGIC detects the GRB 190114C". In: *The Astronomer's Telegram* 12390 (Jan. 2019), p. 1.

[128] H. Abdalla et al. "A very-high-energy component deep in the γ-ray burst afterglow". In: 575.7783 (Nov. 2019), pp. 464–467. DOI: 10.1038/s41586-019-1743-9. arXiv: 1911.08961 [astro-ph.HE].

[129] M. de Naurois and H. E. S. S. Collaboration. "GRB190829A: Detection of VHE gamma-ray emission with H.E.S.S." In: *GRB Coordinates Network* 25566 (Aug. 2019), p. 1.

[130] A. Donini et al. "The Cherenkov Telescope Array Performance in Divergent Mode". In: *36th International Cosmic Ray Conference (ICRC2019)*. Vol. 36. International Cosmic Ray Conference. July 2019, p. 664. arXiv: 1907.07978 [astro-ph.IM].

[131] M. Szanecki et al. "Monte Carlo simulations of alternative sky observation modes with the Cherenkov Telescope Array". In: *Astroparticle Physics* 67 (July 2015), pp. 33–46. DOI: 10.1016/j.astropartphys.2015.01.008. arXiv: 1501.02586 [astro-ph.IM].

[132] T. Gasparetto. "Development of a computing farm for Cloud computing on GPU - Development and optimisation of data-analysis methodologies for the Cherenkov Telescope Array". PhD thesis. Universita' Di Trieste, 2020. URL: https://arts.units.it/handle/11368/2963769.

[133] G. Verna. *Internal talk CTA ASWG*. Private communication. 2020.